THE UNIVERSITY OF CHICAGO

MEASUREMENT OF COLLINEAR W BOSON EMISSION FROM HIGH TRANSVERSE MOMENTA JETS USING THE ATLAS DETECTOR

A DISSERTATION SUBMITTED TO
THE FACULTY OF THE DIVISION OF THE PHYSICAL SCIENCES
IN CANDIDACY FOR THE DEGREE OF
DOCTOR OF PHILOSOPHY

DEPARTMENT OF PHYSICS

BY
MILES ANTHONY KING-TING WU

CHICAGO, ILLINOIS
MARCH 2017

Table of Contents

List of Figures

List of Tables

ACKNOWLEDGMENTS

I feel very lucky to have had David Miller as my advisor, as he has been a truly incredible mentor as I navigated my way through my Ph.D. program. Even though there are not enough hours in the day to do the things he does as a professor, a convenor and now a father, David has always made time to chat with me and discuss my research. During these discussions, he invariably provided really useful feedback and plenty of new and inspiring ideas. Much of this thesis would not have been possible without David, and so I am extremely grateful to him for everything he has done for me.

I would like to thank Mark Oreglia, Paolo Privitera and LianTao Wang for being on my thesis committee and for being so accommodating during the process. My thanks also go out to fellow graduate students, the post-docs and all the professors of the entire University of Chicago ATLAS group for countless intellectually-stimulating conservations and helpful suggestions. In particular, I want to thank Frank Merritt for being my advisor and guiding me for the first couple years of graduate school. Of course, none of this would be possible without the excellent collaborators around the world on ATLAS. I am also thankful to all my physics teachers, especially Valerie Halyo and John Cullerne, for giving me the skills, inspiration and encouragement to pursue my passion.

Lastly, I am indebted to Emily and my parents for being so supportive and patient. Without them, the struggles and toils of research would have been much harder to overcome.

ABSTRACT

The high centre-of-mass energy and luminosity of the Large Hadron Collider offers a unique opportunity to probe the Standard Model in extreme and often unexplored regions of phase space. Processes involving gauge bosons and other massive particles are of particular interest given their potential connection to physics beyond the Standard Model. This thesis presents a measurement of the cross-section of $W \to \mu\nu$ in association with high transverse momenta jets using data collected by the ATLAS experiment from proton–proton collisions at a centre-of-mass energy of 8 TeV at the LHC, corresponding to an integrated luminosity of 20.3 fb^{-1}. The cross-section is expressed as a function of the angular separation between the muon and the closest jet. The focus is on the contributions to W + jets processes from a high transverse momentum jet emitting a real W boson, which are expected to be large at small angular separation. Collinear W emission is an irreducible background to searches for new physics that involves Lorentz-boosted top quarks and is an important probe of both quantum chromodynamics corrections and electroweak corrections to W + jets production. Theoretical predictions of this process, including several novel predictions, are compared to the data in terms of both the absolute and differential cross-sections.

CHAPTER 1

INTRODUCTION

Precision measurements of Standard Model processes at the Large Hadron Collider (LHC) are crucial for probing the fundamental structure of the strong and electroweak interactions. The large data sample collected by the ATLAS experiment from proton–proton collisions at a high centre-of-mass energy provides a great opportunity to perform these measurements in unique topologies that have previously never been studied.

The studies in this thesis [1] peform a measurement of W boson production in association with very high transverse momenta jets. In particular, they focus on the process where a real W boson is emitted from an energetic jet. This emission process is enhanced in the collinear limit, and thus collinear topologies are specifically isolated to study the rate and kinematics of W boson emission. At these high energies, the contribution of collinear W production to W + jets processes is expected to be large, and large quantum chromodynamics (QCD) corrections and electroweak (EW) corrections also arise. This measurement therefore allows for detailed study of these phenomena.

Searches for beyond the Standard Model physics are an important goal of the LHC experiments, and collinear W production can be a significant irreducible background in these searches. If the W decay products are collinear with one of the jets, the structure of that jet can resemble the three-pronged structure of a Lorentz-boosted top quark [2], which is one of the signatures of new physics that is often searched for. Hadronic decays of collinear W bosons may also be a background for searches that focus on the high jet p_{T}, high jet mass regime, as the hadronic W decay causes a large increase in the measured jet mass. Given the relevance of collinear W production to these new physics searches, it is critical to measure its rate and to be able to provide accurate predictions of this process.

Generating accurate predictions of collinear W production is, however, very challenging due to the large higher-order corrections that appear in this new kinematic regime. Multi-

ple theoretical predictions that use different approaches for estimating these corrections are evaluated in this thesis. Some of these calculations are especially interesting due to their novelty, and the studies in this thesis are some of the first to utilise them. Since the predictions are not consistent with each other, comparing them to the results of this measurement is of crucial importance.

This thesis represents the first explicit measurement of collinear W production, which has only recently become accessible with the energies of the LHC. Previous studies of W + jets by both the ATLAS and CMS experiments [3, 4] did not focus on collinear W production, and they also removed the region of phase space where this process is most likely to occur.

This thesis is structured as follows. Chapter 2 provides an overview of the Standard Model and goes into some of the theoretical details behind calculations of W + jets production, including the features of the theoretical predictions evaluated in these studies. Chapter 3 briefly describes the LHC and the ATLAS detector. Chapter 4 summarises how data is collected, how simulated Monte Carlo samples are produced and how physics objects are reconstructed. Chapter 5 describes the analysis in detail and some of the motivation behind the design of the analysis is given. Chapter 6 describes the systematic uncertainties that affect the measurement and how these are evaluated. Chapter 7 examines the results of the measurement and compares them to theoretical predictions. Chapter 8 briefly concludes the measurement.

CHAPTER 2

SUMMARY OF THE STANDARD MODEL

2.1 Overview of the Theory

The Standard Model of particle physics is a quantum field theory that governs all the currently-known fundamental particles and their interactions with each other through three of the four fundamental forces. These fundamental particles, depicted in Figure 2.1, are grouped into two categories: fermions and bosons.

Fermions have half-integer spin and together they make up all the ordinary and exotic matter in the universe. Six leptons and six quarks make up these so-called matter particles and they are divided into three generations of two particles each, where each generation is progressively heavier than the previous generation. As the second generation and third generation of particles are unstable and have a short lifetime, all ordinary stable matter is made from particles from the first generation. The electron, muon and tau leptons have an electric charge of -1, while their corresponding neutrinos have no electric charge, are (nearly) massless and are very weakly interacting with ordinary matter. The quarks have an electric charge of either $+2/3$ or $-1/3$, but they also carry colour, which can be either red, green or blue. For every fermion, there also exists a corresponding anti-particle that has the same mass but opposite charge.

Bosons, on the other hand, have integer spin and when these so-called force carriers are exchanged between pairs of fermions they carry the fundamental forces of the universe. The massless gluon carries the strong force and interacts with the six quarks. The massless photon carries the electromagnetic force and interacts with all particles with non-zero electric charge. The massive W and Z bosons carry the weak force and interact with all the fundamental particles. Notably, the Standard Model does not contain a description of the gravitational force and its force-carrier particle, the graviton, has not yet been found. At the scales

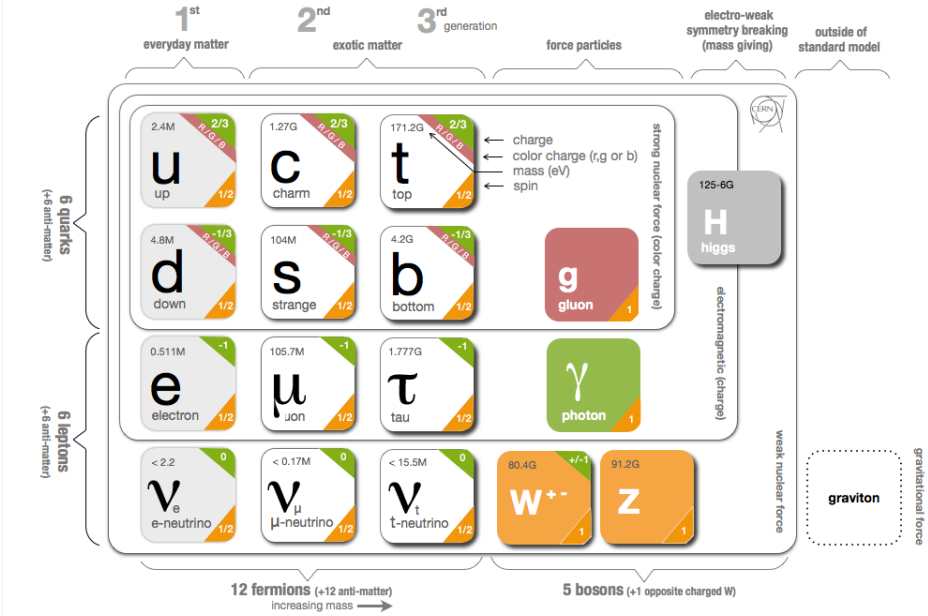

Figure 2.1: An infographic depicting the fundamental particles of the Standard Model of particle physics. Source: [5]

probed at the LHC, gravitational forces are many orders of magnitude smaller than the other three fundamental forces, so they can be safely ignored. Lastly, the Higgs boson, a massive scalar, gives all the other fundamental particles their mass through spontaneous electroweak symmetry breaking.

Mathematically the Standard Model can be represented by the gauge symmetry group $\mathrm{SU}(3) \times \mathrm{SU}(2) \times \mathrm{U}(1)$. The $\mathrm{SU}(3)$ group gives rise to the eight gluons that carry the strong force, and this portion of the Standard Model is known as quantum chromodynamics (QCD). The $\mathrm{SU}(2) \times \mathrm{U}(1)$ group gives rise to the photon, W boson and Z boson that together carry the electroweak (EW) force.

Ever since its introduction in the mid-1970s, the Standard Model has stood the test of time as the most accurate theory of the fundamental particles and their interactions. Some of its triumphs include predicting the top quark [6, 7] and its properties and the

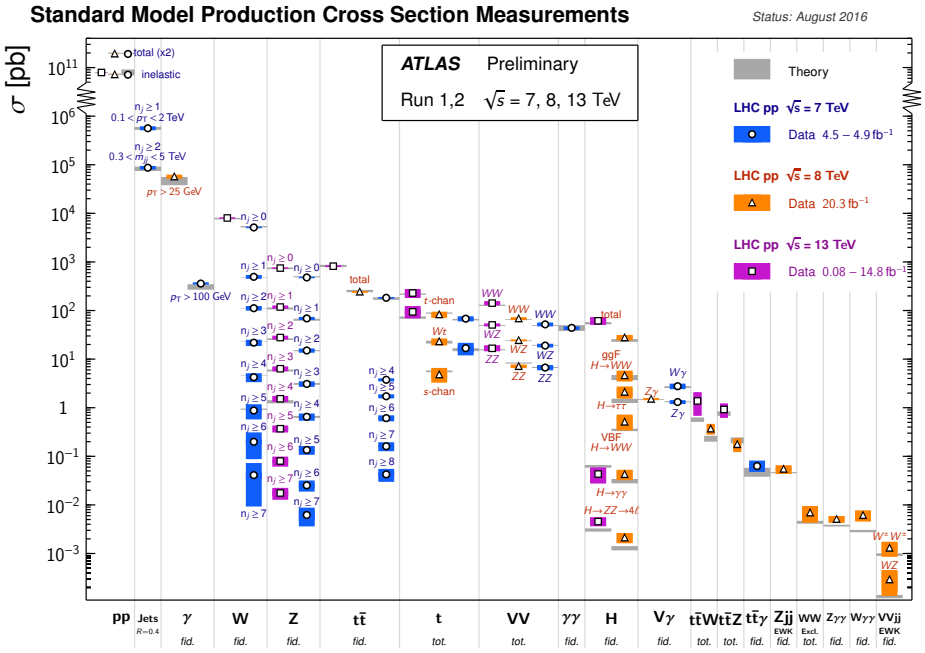

Figure 2.2: Many Standard Model cross-section measurements made by ATLAS, along with the corresponding Standard Model predictions. Source: [15]

Higgs boson [8–10], all of which were experimentally confirmed many decades later [11–14]. Precision measurements of a vast range of processes have been made, and thus far no statistically significant discrepencies with the Standard Model have been found. For example, ATLAS has made many cross-section measurements, shown in Figure 2.2, and the results agree well with the predictions from the Standard Model [15]. Perhaps the largest deviation discovered so far is in the muon anomalous magnetic moment, where currently the experimental measurement and the Standard Model disagree by 3.4σ [16], but this is below the community's typical 5σ certainty threshold.

Despite its resounding success, there are nonetheless a couple of deficiencies in the Standard Model. Numerous cosmological observations, such as measurements of galaxy rotation curves [17], the cosmic microwave background [18] and gravitation lensing [19], together have demonstrated beyond doubt the existence of dark matter, and it is estimated that it accounts for 85% of the mass of the universe. However, the Standard Model does not contain

any particles that could account for the dark matter. The universe today overwhelmingly consists of matter and there is very little antimatter, despite the common assumption that the Big Bang produced equal amounts of both. Although matter-antimatter asymmetry can arise from charge–parity (CP) violating processes in the Standard Model, these occur far too rarely to produce the massive asymmetry seen today [20].

Some theoretical aspects of the Standard Model are also unsatisfying. One example is the heirachy problem. When attempting to calculate the mass of the Higgs boson, corrections from loop diagrams involving virtual particles cause the mass to diverge up to the gravitational Planck scale, which is approximately 10^{18} GeV. To reconcile this prediction with the recent observation of the Higgs boson at a mass of 125 GeV, many orders of magnitude smaller than the Planck scale, the leading-order bare mass of the Higgs boson must nearly exactly cancel the loop corrections. This near-exact cancellation would be extremely sensitive to the bare mass and this is considered unnatural.

These deficiencies and shortcomings of the Standard Model have led theorists to suggest theories that go beyond the Standard Model to solve these problems. One of the main goals of ATLAS is to search for evidence of beyond the Standard Model physics, but, thus far, there has been no statistically significant evidence of new physics.

2.2 QCD, Electromagnetic and Weak Radiation

For each force in the Standard Model, there exists an associated radiation, where a real or virtual particle can be emitted. Through the electromagnetic force, a charged particle can radiate a photon and this is known as bremsstrahlung. Through the strong force, a quark can radiate a gluon. Finally, a similar process can occur through the weak force, where a massive W or Z boson can be radiated from a quark.

While the first two processes are very common and well-understood through the theories of QCD and QED (quantum electrodynamics), weak radiation, which is the focus of this

thesis, has not been studied experimentally in detail before. This is because the process has only recently become accessible with the energies of the LHC, as quarks must have a large amount of energy to create the W or Z boson due to their large mass.

2.3 Inclusive W boson Production

While there are an unlimited number of Feynman diagrams that can take a given initial state to a specified final state, and, by the principles of quantum mechanics, these all interefere either constructively or destructively, a pertubative approach is typically used for calculations. Each diagram in the unlimited set can be categorised by the number of QCD interaction vertices and the number of EW interaction vertices it contains. When calculating the cross-section, each additional QCD and EW vertex adds a factor of α_{S} and α_{EW} respectively, where α_{S} is the gauge coupling of the QCD theory and α_{EW} is the gauge coupling of the EW theory. Since at short-distances both $\alpha_{\mathrm{S}} \ll 1$ and $\alpha_{\mathrm{EW}} \ll 1$, the pertubative approach of expanding to orders in α_{S} and α_{EW} generally works well, and each order after leading-order (LO) is a successively smaller correction. However, as one shall see in the following section, there are often kinematic topologies where leading-order calculations are not sufficient and the higher-order corrections are large.

At leading-order, W bosons can be produced through the electroweak interaction of a quark and antiquark, illustrated in the Feynman diagram of Figure 2.3. Since electric charge is conserved, the charge of the quark and the anti-quark must add up to the charge of the W, $+1$ or -1. For example, for a W^+ boson, this restricts the quark–antiquark combinations to pairs of an up-type quark (u, c, t) and a down-type antiquark ($\bar{d}$, $\bar{s}$, $\bar{b}$). The entries of the Cabibbo–Kobayashi–Maskawa (CKM) matrix govern the relative strength of weak interactions between the quarks of different flavours. While the diagonal entries, $|V_{ud}|$, $|V_{cs}|$ and $|V_{tb}|$, are very nearly 1, the off-diagonal terms are much smaller. As a result, production of W bosons from mixed-generation quark–antiquark interactions is supressed.

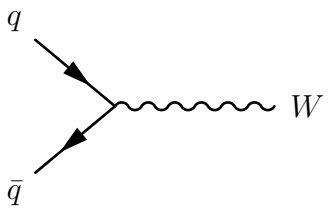

Figure 2.3: Feynman diagram for leading-order W boson production.

Furthermore, one needs to consider the flavour of quarks that make up the colliding protons. This is provided by parton distribution functions, which are described in more detail in Section 2.5. At the LHC, the most common colliding parton is the up quark, followed by the down quark [21]. This leads to a charge asymmetry in W boson production at the LHC, where more W^+ bosons are produced than W^- bosons. Taking all of this into account, the relative rates of W^+ and W^- boson production as a function of the interacting quark flavours are shown in Figure 2.4. Notably the rate for W^+ boson production is approximately 50% larger than that for W^- boson production.

2.4 W + jets Production

While the previous section introduced inclusive W boson production, the studies contained in this thesis focus on events where the W boson is produced in association with at least one jet—a process termed $W + \geq 1$-jet. These hadronic jets are narrow sprays of particles formed from the final state radiation (FSR) and subsequent hadronization of bare quarks and gluons.

Using the same concepts of inclusive W boson production from the previous section, one can derive the two sub-processes that make up W + 1-jet production to leading-order, $q\bar{q} \to Wg$ and $qg \to Wq$, whose Feynman diagrams are shown in Figure 2.5. Since transverse momentum is conserved and must vectorially sum to zero at a particle collider, the W boson is balanced by the recoil hadronic jet and they must travel with equal and opposite momentum in the transverse plane. This configuration is often referred to as *back-to-back* production.

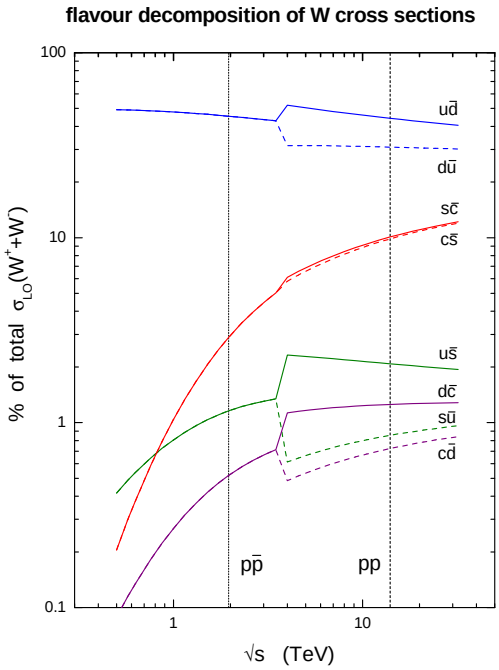

Figure 2.4: The cross-section of W boson production as a function of centre-of-mass energy and quark and antiquark flavours. For $\sqrt{s} < 4$ TeV the lines correspond to W boson production at a $p\bar{p}$ collider. For $\sqrt{s} > 4$ TeV the solid lines correspond to W^+ boson production and the dashed lines correspond to W^- boson production at a pp collider. These results were calculated with the MSTW 2008 parton distribution function set [21]. Source: [22]

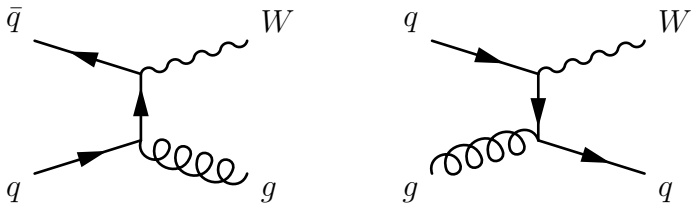

Figure 2.5: Feynman diagram for leading-order W + 1-jet production

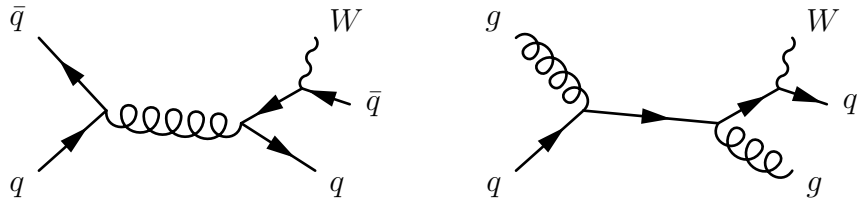

Figure 2.6: Example Feynman diagrams for real W emission from a final-state quark. These are only provided as an illustrative example, and there are numerous other diagrams for this process that are not shown here.

When calculating $W + \geq 1$-jet production at next-to-leading order (NLO), both QCD and EW corrections arise from including contributions that involve an additional real emission—i.e. another external leg in the Feynman diagram—and contributions that involve a virtual loop. In particular, several of these contributions involve the emission of a real W boson from an initial- or final-state quark. A couple of example Feynman diagrams for real W boson emission are shown in Figure 2.6.

In the collinear limit where the angular separation between the W boson and the quark is very small, the terms in the calculation for such an emission involve a logarithm of a fraction that has the mass of the emitted particle in the denominator. In the limit of vanishing W mass, there is therefore a divergence and the emission would be perfectly collinear, analogous to massless gluon emission. However, since the W boson is massive, the collinear divergence is regulated and there is only a collinear enhancement in the distribution of angular separation between the W boson and the quark.

Typically in QCD, corrections from real emissions tend to cancel the corrections from virtual loops [23]. However, the large mass of the W boson does not allow for such a cancellation of the EW corrections. The size of these NLO EW corrections can be approximated with a Sudakov–type leading logarithm term $\mathcal{O}\left(\alpha_{\mathrm{EW}} \ln^2 p_{\mathrm{T},j}/m_W\right)$, where α_{EW} is the gauge coupling of the EW theory, $p_{\mathrm{T},j}$ is the transverse momentum of the jet and m_W is the mass of the W boson. As such, these become increasingly large in the presence of highly energetic jets. For example at 2 TeV, they are approximately 40% [24].

In the case of collinear emission of massless particles, such as gluon radiation, the logarithmic divergences render the use of pertubation theory in calculations ineffective. To accurately study these emissions with a pertubative approach, one would need to calculate upto very high orders which is challenging. Instead, the parton shower approach is often used where each initial- and final-state parton is given probabilities to radiate or split and the logarithms are resummed to all orders. The Sudakov form factors and Dokshitzer–Gribov–Lipatov–Altarelli–Parisi (DGLAP) equations govern the evolution of the parton shower, and in the collinear limit they are universally applicable to any process [25].

While the massive W boson does not suffer from these logarithmic divergences, nonetheless the corrections can be large at small angles, and it might be necessary to consider even higher-order corrections to obtain an accurate description of collinear W emission at high transverse momentum. Since it can be difficult to calculate these higher-order corrections, recently an analogous procedure to the approach used for massless gluon emission has become available [26, 27]. This is called the electroweak parton shower, and it includes the ability to emit W bosons in the parton shower.

In the previous paragraphs, collinear W emission has been discussed as a NLO contribution to the W + 1-jet process. However, this final state where a W is emitted close to a quark can also be considered as a leading-order W + 2-jet process or as a higher-order correction to a QCD dijet process. In general, there is an ambiguity of how to describe any given final state, as it can be designated as its own process or as several different corrections to several other processes. The most appropriate description depends on context and what the core process being studied is. For example, in the context of reconstructing hadronically-decaying Lorentz-boosted top quarks, one of the main backgrounds is QCD dijets, so it would make the most sense to consider collinear W emission as a correction to QCD dijets. When combining multiple processes at orders higher than leading-order, one must also be very careful to avoid so-called double counting, as the same diagram may be included more than once,

leading to an incorrect result.

In Section 7.3, the measurement results of this thesis are compared to various theoretical calculations. In the following sub-sections, the setups of these theoretical calculations are described.

2.4.1 ALPGEN – Multi-leg LO

Events containing $W \to \mu\nu + Np$, where N is the number of partons p in the final state in addition to the W boson, are generated with ALPGEN v2.14 [28] at leading-order using the CTEQ6L1 LO PDF set [29]. Since ALPGEN does not perform any parton showering, it is interfaced with PYTHIA v6.427 [30] for the parton showering and fragmentation. To avoid double-counting final states involving a jet that could be generated in either the ALPGEN matrix elements or the PYTHIA parton shower, the MLM procedure to match jets with partons [31] is applied. This procedure requires every parton to be close in angular separation to a unique jet and there to be no additional jets in the event, otherwise the event is rejected. Monte Carlo samples are produced for each value of N for $1 \leq N \leq 5$ and then combined to provide a reasonable calculation of the overall $W+ \geq$ 1-jet process. Figure 2.7 shows the expected distribution of the angular separation between the W boson and the closest jet as calculated by ALPGEN, split by each process that has a different value of N. This is known as a multi-leg leading-order approach and has been very successful at calculating several important kinematic distributions, such as the number of jets in W + jets events [3].

Events containing $W \to \mu\nu + c + Np$, $W \to \mu\nu + c\bar{c} + Np$ and $W \to \mu\nu + b\bar{b} + Np$ are also generated for $0 \geq N \geq 4$, $0 \geq N \geq 3$ and $0 \geq N \geq 3$ respectively. These samples explicitly contain massive b- or c-quarks in the matrix elements, in contrast to the non-heavy flavour samples that do not and that only contain events with heavy-flavour through heavy-flavour production in the parton showering. Again, to avoid double-counting these heavy-flavour final states, a veto procedure is applied. This procedure uses the matrix element approach

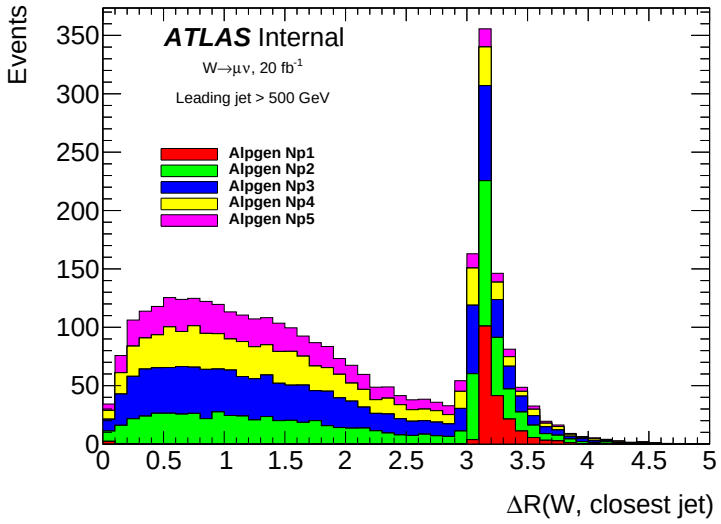

Figure 2.7: Expected distribution of the angular separation between the W boson and the closest jet for $W \to \mu\nu + Np$ production, as calculated by ALPGEN. Each process that has a different value of N is shown in a stacked histogram. Events are required to have a jet with $p_{\mathrm{T}} > 500$ GeV.

for when the opening angle between the quarks is large and uses the parton shower approach when the opening angle is small. This is because the matrix element approach, where each jet in the event corresponds one-to-one with each parton in the matrix elements calculation, is more accurate for widely-separated partons than the parton shower approach, but much poorer at small angles where the pertubative approach breaks down due to the large collinear logarithms. The relative strengths of these two approaches is in fact the motivation for using the parton shower approach to model collinear W emission in the PYTHIA8 calculation, and this is discussed in more detail in Section 2.4.2.

In the ALPGEN calculation, many potentially large NLO QCD and EW corrections are not included, and this could impact the accuracy of this calculation in the topology of this measurement. While a k-factor is applied, this only corrects the overall inclusive cross-section and therefore the normalisation of distributions, not their shapes. This k-factor is calculated by comparing a calculation performed to next-to-next-to-leading-order (NNLO) in QCD by FEWZ [32] using the MSTW 2008 NNLO PDF set with the nominal cross-section

from ALPGEN.

2.4.2 PYTHIA – Weak Shower

Events containing W + 1-jet production and QCD dijet production are generated with PYTHIA v8.210 [33] at leading-order using the CT10 NLO PDF set [34]. While this normally would not contain any events with collinear W boson emission, since this is not part of leading-order W + 1-jet production or leading-order QCD dijet production, PYTHIA is configured to enable its implementation of an electroweak parton shower [26] where a W boson can be emitted during the shower. This is a relatively new feature of PYTHIA and was introduced in v8.176. By extending the parton shower to include EW emissions, QCD, electromagnetic and weak radiation are unified and treated equally within the same machinery. This allows for competition between the emissions of gluons, photons and W and Z bosons within a jet. As alluded to earlier, this description of W bosons being emitted in the shower can be more convenient than the W + jets matrix elements description for certain contexts, for example, when studying the substructure of jets, where W emission can have a significant effect. This approach also naturally allows for the possibility of multiple W or Z boson emissions, which becomes more likely at extremely high jet p_{T}, where as the matrix element approach would need to handle each final state explicitly.

Therefore, in this calculation W bosons can be either produced in the matrix elements of a W + 1-jet event or emitted as electroweak final-state radiation in the parton shower of QCD dijet events. Figure 2.8, which shows the differential cross-sections for the angular separation between the W boson and the closest jet for these two processes as calculated by PYTHIA, demonstrates that in this calculation the weak parton shower process dominates at small angles and the leading-order W + 1-jet process dominates at large angles.

At small angular separation between the W and the closest jet, the parton shower approach of PYTHIA could yield a more accurate calculation of collinear W boson emission

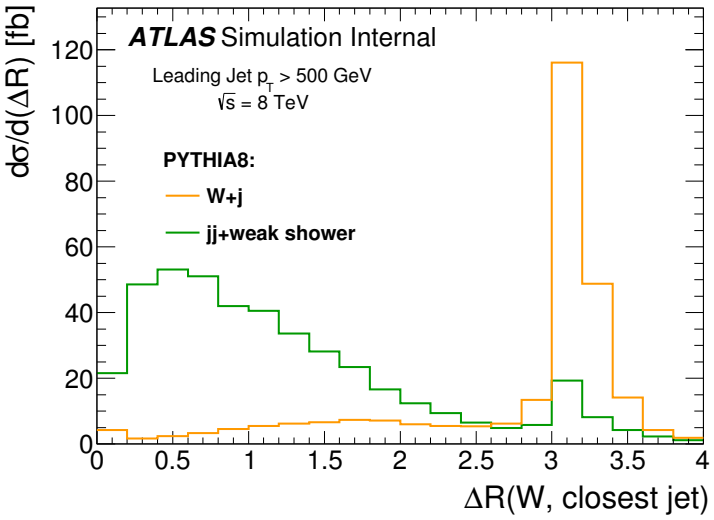

Figure 2.8: Differential cross-section for the angular separation between the W boson and the closest jet for W + 1-jet production (orange) and QCD dijet production with electroweak parton showering (green), as calculated by PYTHIA. Events are required to have a jet with $p_{\mathrm{T}} > 500$ GeV.

than the matrix element approach. This is because, in this collinear limit, the pertubative series does not converge rapidly due to large logarithmically enchanced terms, and so a fixed-order matrix element calculation may not be that accurate. With the parton shower approach, the leading-logarithmic terms can be summed to all orders using resummation techniques. However, compared to ALPGEN, PYTHIA lacks many diagrams related to other aspects of $W + \geq 2$-jet production, and so this calculation could provide a poor description of regions of the measurement other than the region of small angular separation.

2.4.3 SHERPA+OpenLoops – NLO QCD+EW

A calculation of the differential cross-section for the angular separation between the muon and the closest jet of W + 1-jet and W + 2-jet production at NLO in both QCD and EW was performed by the authors of Ref. [35] specifically for the studies in this thesis. In the case of W + 2-jet production, Ref. [35] was the first NLO QCD+EW prediction of this process. This was done by combining the OpenLoops matrix-element generator [36, 37],

which recently gained the ability to calculate NLO EW and NLO QCD corrections in a fully automated fashion [35], with the SHERPA Monte Carlo generator [38–40]. At first, the calculation was only performed for on-shell W boson production since this simplification significantly reduces the computational complexity, as adding off-shell production at NLO in EW increases the number of particles to consider in EW loops. This was later extended to include off-shell W boson production as well [41]. It also contains the sub-leading Born-level contributions. These are $\mathcal{O}\left(\alpha_{\mathrm{EW}}^3\right)$ in W + 1-jet production and $\mathcal{O}\left(\alpha_{\mathrm{S}}\alpha_{\mathrm{EW}}^3\right)$ in W + 2-jet production.

The NNPDF2.3QED NLO PDF set [42] is used. Both the renormalisation and factorisation scales are set to $\mu_0 = 1/2\left(\sqrt{m_{\mu v}^2 + (p_{\mathrm{T}}^{\mu v})^2} + \Sigma_i p_{\mathrm{T}}^{J_i} + \Sigma_i p_{\mathrm{T}}^{\gamma_i}\right)$, where $m_{\mu v}$ and $p_{\mathrm{T}}^{\mu v}$ are the mass and transverse momentum of the total four-momentum of the muon and neutrino, $p_{\mathrm{T}}^{J_i}$ is the transverse momentum of each jet, and $p_{\mathrm{T}}^{\gamma_i}$ is the transverse momentum of each photon.

To combine the calculations for W + 1-jet and W + 2-jet production, some care must be taken to avoid double-counting final states that can be generated in both processes. The exclusive sums approach is used, so events in the W + 1-jet calculation that contain a second jet are vetoed, resulting in a calculation for W + 1-jet exclusive production. Figure 2.9 shows the differential cross-section and the magnitude of the NLO corrections for the angular separation between the muon and the closest jet as calculated by SHERPA+OpenLoops for W + 1-jet inclusive, W + 1-jet exclusive, W + 2-jet inclusive and the exclusive sums combination. Notably, the NLO EW corrections and sub-leading Born-level corrections together can have significant effects—up to 20%—across the angular distribution.

2.4.4 N_{jetti} NNLO QCD

A calculation to next-to-next-to-leading-order (NNLO) in QCD of the angular separation between the muon and the closest jet for $W + \geq$ 1-jet events recently became available [44].

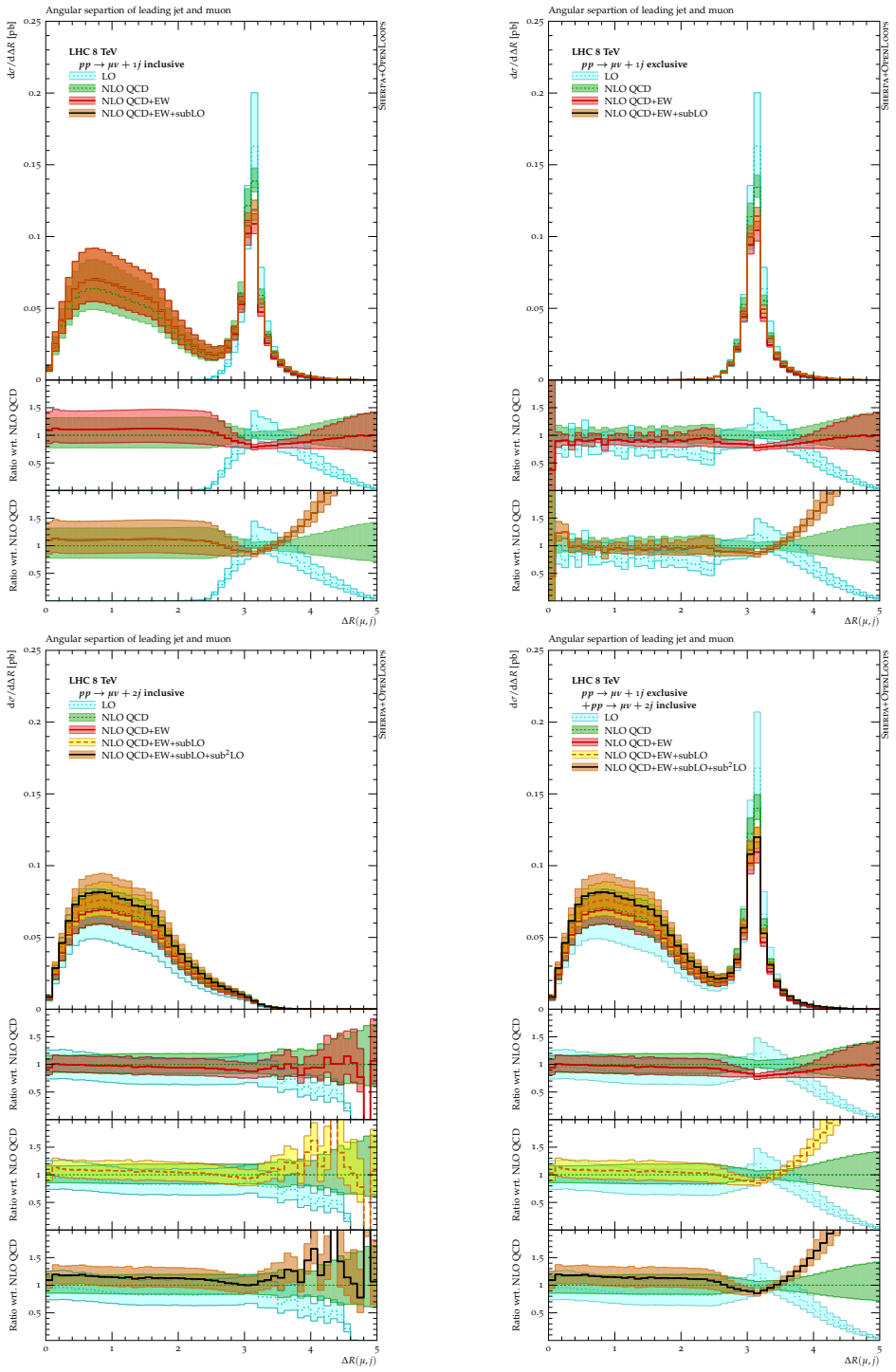

Figure 2.9: Differential cross-section for the angular separation between the muon and the closest jet for W + 1-jet inclusive (upper left), W + 1-jet exclusive (upper right), W + 2-jet inclusive (lower left) and the exclusive sums combination of W + 1-jet and W + 2-jet (lower right), as calculated by SHERPA+OpenLoops. The NLO QCD and NLO EW corrections are shown in the lower panels. Events are required to have a jet with $p_{\mathrm{T}} > 500$ GeV. The shaded bands represent the scale uncertainties. Source: [43]

This is the first exact NNLO QCD calculation of this observable. It includes terms up to $\mathcal{O}\left(\alpha_{\mathrm{S}}^{3}\right)$ and was specifically performed by the authors of Ref. [44] to enable comparisons with the measurement results contained in this thesis. It uses a new technique based on N-jettiness [45, 46] to split the phase space for the real emission corrections, and it also relies on the theoretical formalism provided in soft-collinear effective theory.

The CT14 NNLO PDF [47] is used. Both the renormalisation and factorisation scales are set to $\mu_0 = \sqrt{m_{\ell\nu}^2 + \Sigma_i (p_{\mathrm{T}}^{J_i})^2}$, where $m_{\ell\nu}$ is the invariant mass of the lepton and neutrino and $p_{\mathrm{T}}^{J_i}$ is the transverse momentum of each jet. As the calculation was peformed at parton-level, the jets are built by clustering the partonic final state using the anti-k_t jet algorithm with a radius parameter $R = 0.4$. No non-perturbative corrections are applied.

Figure 2.10 shows the differential cross-section for the angular separation between the muon and the closest jet for $W + \geq 1$-jet production, calculated at LO, NLO and NNLO in QCD. The NNLO QCD corrections also have a significant effect—up to 30%—across the angular distribution. Another notable effect of the NNLO QCD corrections is the reduction in the scale uncertainty. It decreases from $\sim \pm 20\%$ at NLO to $+3\%/-7\%$ at NNLO.

2.5 Parton Distribution Functions

While the Standard Model enables the calculation of cross-sections as a function of the energies of the colliding partons, the LHC is a proton–proton (pp) collider and so one is interested in cross-sections for a given proton energy. Parton distribution functions (PDFs), determined experimentally, describe the distribution of the fraction of the proton's energy that is carried by each constituent parton. By integrating a calculated cross-section that is a function of parton energies with the probability of these energies from the parton distribution function, the pp cross-section can be evaluated. There is some uncertainty in these parton distribution functions, and this causes some uncertainty in predicted cross-sections.

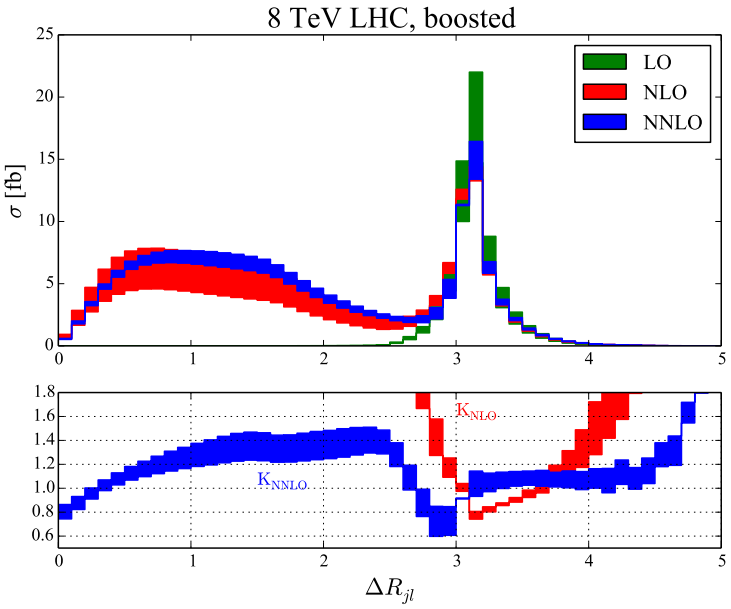

Figure 2.10: Differential cross-section for the angular separation between the muon and the closest jet for $W + \geq$ 1-jet production, calculated at LO, NLO and NNLO in QCD. The NLO and NNLO QCD corrections are shown in the lower panel. The final state is required to have a jet with $p_{\mathrm{T}} > 500$ GeV. The shaded bands represent the scale uncertainties. Source: [44]

CHAPTER 3

THE LHC AND THE ATLAS DETECTOR

3.1 The Large Hadron Collider

The Large Hadron Collider (LHC) [48] is a 27 km circumference circular particle collider, located at the European Organization for Nuclear Research (CERN) in Geneva, Switzerland. It was designed to accelerate two beams of protons in opposite directions to an energy of 7 TeV per beam and collide them with a centre-of-mass energy $\sqrt{s} = 14$ TeV at four interaction points (IP) that are located around the circular ring, illustrated in Figure 3.1. A particle detector around each interaction point observes the results of these collisions. These detectors corresponds to the four major LHC experiments: ALICE, ATLAS, CMS and LHCb. There are also a few smaller experiments, TOTEM, LHCf and MoEDAL, that are located close to the ATLAS and CMS interaction points. The LHC also has the capability of colliding heavy ions, such as lead ions, but the studies in this thesis exclusively focus on proton–proton (pp) collisions.

The LHC accelerates the circulating protons in two beampipes, evacuated to a high vacuum, through the use of superconducting radio-frequency (RF) cavities. Within these cavities, a resonating electromagnetic field that oscillates at 400 MHz is built up. Using these, the LHC is able to accelerate the proton beams to the design energy of 7 TeV per beam in approximately twenty minutes.

The initial proton beams that enter the LHC have already been accelerated by a series of smaller accelerators to an energy of 450 GeV per beam. First, the Linac 2 linear accelerator accelerates the protons to an energy of 50 MeV. These then enter the Proton Synchrotron Booster, a circular accelerator, where they are accelerated to 1.4 GeV and passed to the Proton Synchroton, another circular accelerator. Here they are accelerated to 26 GeV. This is finally followed by the Super Proton Synchroton, again a circular accelerator, that brings

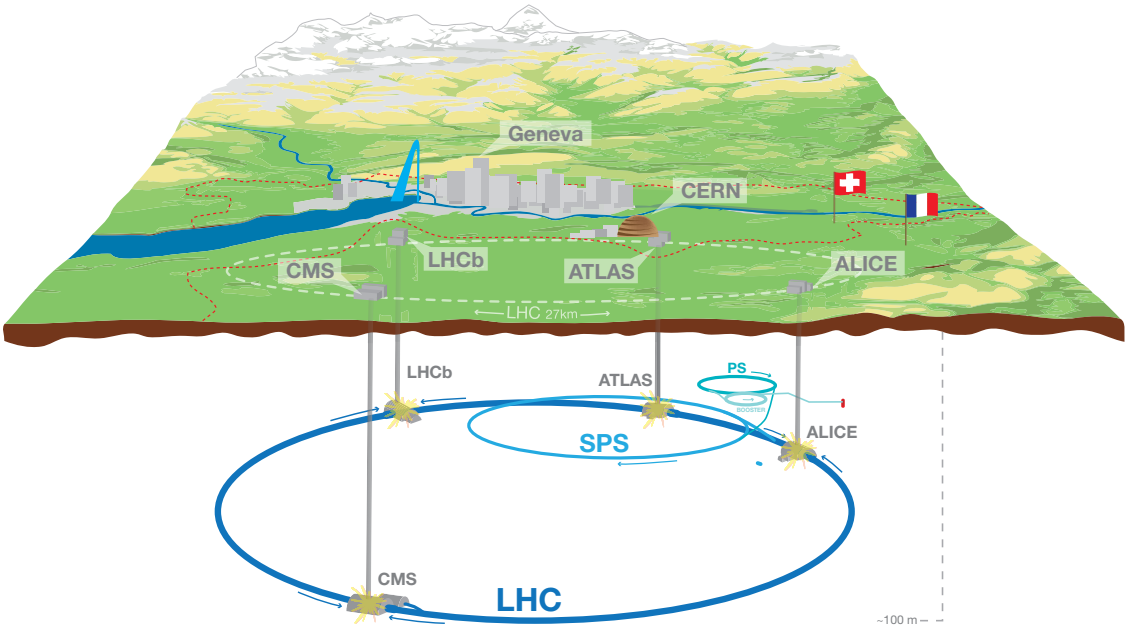

Figure 3.1: Overall view of the Large Hadron Collider (LHC) and its preceeding accelerators. The four main experiments—ALICE, ATLAS, CMS and LHCb—are also marked. Source: [49]

the proton beams to the input energy of the LHC—450 GeV per beam.

Superconducting dipole magnets provide a magnetic field of up to 8.3 T and these steer the proton beams around the circular ring. Quadrupole magnets, along with higher order multipole magnets, are used to keep the beam focused to an approximate width of 0.2 mm. Near the four interaction points, the LHC has additional quadrupole magnets known as inner triplets. These further focus the beams even tighter—to an approximate width of 16 μm [50]—so that when they cross at the interaction points, the luminosity, which is proportional to the rate of proton–proton collisions, is maximised. The protons are not distributed uniformly around the LHC ring, but instead are grouped into bunches. When the bunches cross, multiple proton–proton interactions can occur. The additional interactions to the hard scatter, defined as the collision with the largest momentum transfer, are known as pile-up and can confound analysis of the recorded event. The LHC was designed to produce a luminosity of up to $\mathcal{L} = 10^{34}$ cm^{-2}s^{-1}, using 2808 bunches colliding every 25 ns.

The luminosity of the LHC can be calculated using the number of protons in each bunch n_p, the number of bunches n_b, the frequency of revolution f_r and the convolved beam widths in the horizontal and vertical direction Σ_x and Σ_y [51]:

$$\mathcal{L} = \frac{n_b f_r n_p^2}{2\pi \Sigma_x \Sigma_y}.$$

The number of protons in each bunch n_p is measured using beam current monitors. The beam widths Σ_x and Σ_y are determined by sweeping the beams across each other in a scan known as a van der Meer scan. By observing the relative interaction rate as a function of the beam offset during these scans, the beam profile and its widths can be measured.

The studies in this thesis utilise data from pp collisions during 2012. During this time, the LHC was operated at a lower centre-of-mass energy of $\sqrt{s} = 8$ TeV and produced collisions at a slightly reduced peak luminosity of $\mathcal{L} = 8 \times 10^{33}$ cm^{-2}s^{-1} (see Figure 3.2 for the peak luminosity during each run), using 1380 bunches containing around 1.7×10^{11} pro-

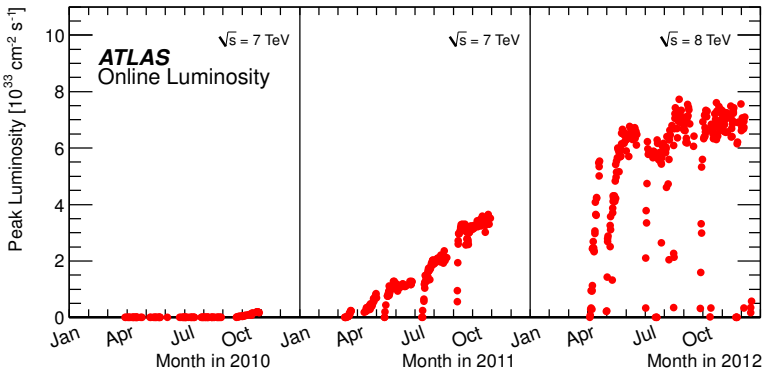

Figure 3.2: The peak luminosity delivered to ATLAS by the LHC for each *pp* run in 2010, 2011 and 2012. Source: [52]

tons colliding every 50 ns. The number of interactions per bunch crossing at the ATLAS interaction point is calculated by dividing the per-bunch-crossing luminosity, which is the instantaneous luminosity measured by the ATLAS detector divided by the bunch crossing rate, by the total inelastic cross-section. The distribution of this is shown in Figure 3.3. On average, each bunch crossing had 20.7 *pp* interactions.

3.2 The ATLAS Detector

The ATLAS detector [53] is a general-purpose particle detector located at one of the interaction points of the LHC. It provides nearly full solid angle coverage, maximising its ability to detect and measure all the products of a proton–proton collision, excluding neutrinos which are so weakly interacting that they pass through the detector undetected. The detector is comprised of four main subdetectors that are arranged concentrically around the beam pipe of the LHC, shown in Figure 3.4. The innermost subdetector is the Inner Detector (ID), followed by the Electromagnetic (EM) Calorimeter, the Hadronic Calorimeter and finally the Muon Spectrometer (MS).

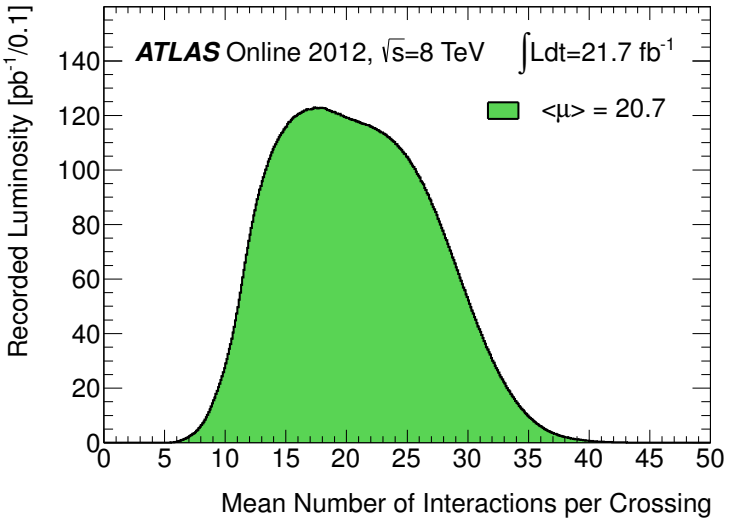

Figure 3.3: The distribution of the number of pp interactions per bunch crossing at ATLAS during 2012. Source: [52]

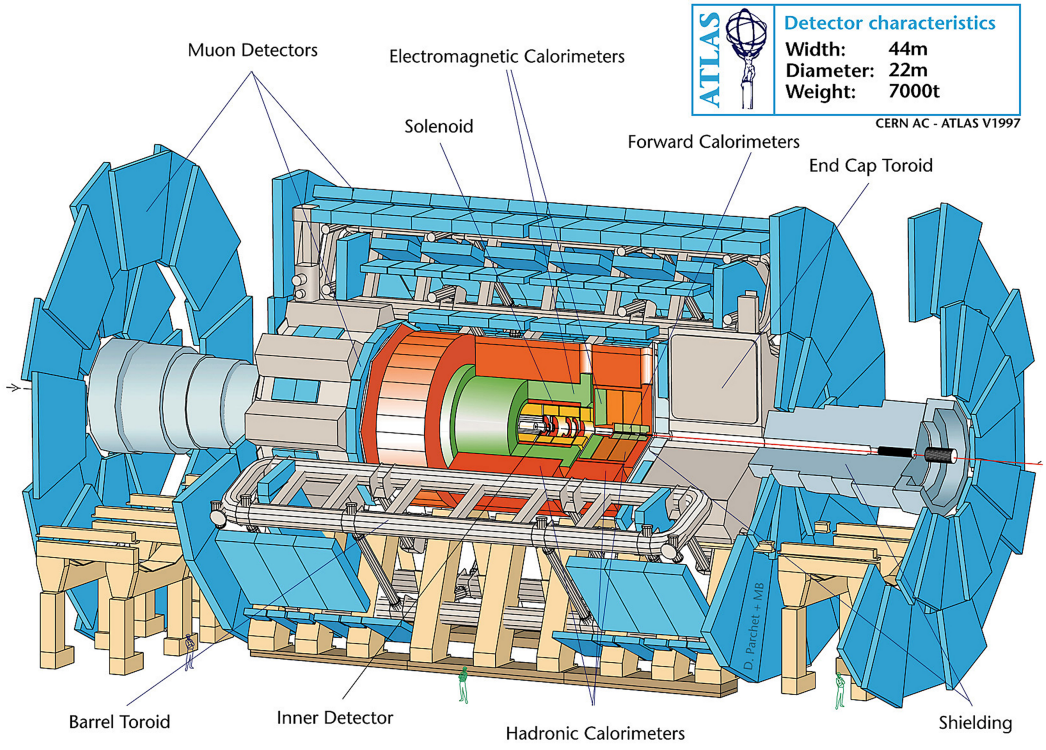

Figure 3.4: An overview of the main components of the ATLAS detector. Source: [54]

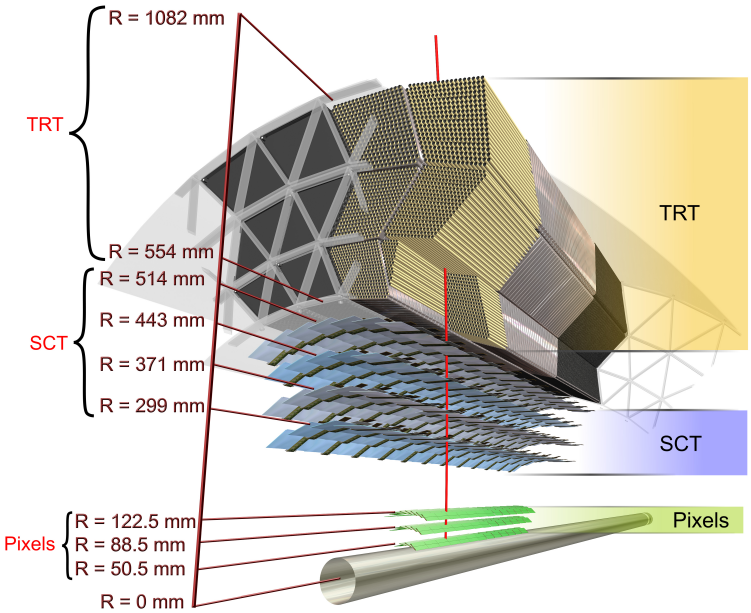

Figure 3.5: An overview of the Inner Detector. Source: [55]

3.2.1 Inner Detector

The Inner Detector, located closest to the beam pipe, detects charged particles and enables reconstruction of their momenta. It provides coverage within $|\eta| < 2.5$[1] and is made up of three components shown in Figure 3.5—the Pixel Detector, the Semiconductor Tracker (SCT) and the Transition Radiation Tracker (TRT)—that register the position of a charged particle whenever one passes through their sensors. These recorded positions are known as hits. From these hits, the path of charged particles can be reconstructed, and these are known as tracks.

The Pixel Detector surrounds the beampipe with 80 million silicon pixel sensors, organised into 3 layers covering $|\eta| < 2.5$. Most of the pixels measure 50 μm by 400 μm in size

1. ATLAS uses a right-handed coordinate system with its origin at the nominal interaction point (IP) in the centre of the detector and the z-axis along the beam pipe. The x-axis points from the IP to the centre of the LHC ring, and the y-axis points upward. Cylindrical coordinates (r, ϕ) are used in the transverse plane, ϕ being the azimuthal angle around the z-axis. The pseudorapidity is defined in terms of the polar angle θ as $\eta = -\ln\tan(\theta/2)$.

(10% of the pixels are located in gaps between read-out chips and these are slightly larger at 50 μm by 600 μm) and can measure a charged particle's two-dimensional position. When a charged particle traverses one of the silicon pixels, it ionizes the silicon and produces electrons. A high voltage is applied across the silicon using electrodes, and therefore the ionization electrons drift towards the anodes. This drift current can then be measured. If the centre of the pixel were used as the position for the charged particle, this would result in a measurement uncertainty of $50/\sqrt{12}$ μm by $400/\sqrt{12}$ μm, as the variance of a uniform distribution between 0 and l is $l^2/12$. However, the position within the pixel can be determined through interpolation using the amount of charge collected on each edge of the pixel. This improves the spatial resolution of the pixels to 10 μm by 115 μm.

The Semiconductor Tracker surrounds the Pixel Detector with more silicon sensors, but here they are in the form of 6 million strips of width 80 μm. These are organised into eight layers in the barrel and eighteen layers in the endcaps, covering $|\eta| < 2.5$. Unlike pixels, strips only provide a spatial measurement in one direction. To achieve a two-dimensional position measurement, within each pair of layers the layers are set at a 40 milli-radian angle with respect to each other. The intersection of the two lines formed from one-dimensional measurements in two layers yields the two-dimensional position. In practice, for track reconstruction, which is described in Section 4.3.1, the 1-D hits from each layer are input to a fit which combines all the 1-D and 2-D hits in the Inner Detector to provide a best estimate of the track's parameters.

The Transition Radiation Tracker is the outermost component of the Inner Detector and is made up of three hundred thousand proportional drift tubes. These are arranged into 73 planes in the barrel and 160 planes in the endcaps, covering $|\eta| < 2.0$. These cylindrical straw tubes are 4 mm in diameter, are filled with a gas mixture consisting of 70% xenon, 27% carbon-dioxide and 3% oxygen and contain a 0.03 mm gold-plated tungsten wire at the centre that applies a high voltage. Xenon gas was chosen as it is particularly effective at

absorbing transition radiation photons. Just like with the silicon detectors, a charged particle causes ionization electrons in the gas, which then causes a drift current in a large electric field that can be measured by the wire. The position along the width of the straw is obtained by looking at the drift time. When the charged particle track passes close to the wire, the drift time is quicker. This is illustrated in Figure 3.6. The Transition Radiation Tracker also provides identification of electrons by interleaving polypropylene fibers between the straws and looking for transition radiation photons. Signals are compared against two energy thresholds, a low-threshold of around 300 eV and a high-threshold of around 6 keV, and hits for each threshold are stored separately. Transition radiation photons cause more energetic ionization than other charged particles, so they produce more high-threshold hits. Since electrons have a much smaller mass than pions, they produce larger amounts of transition radiation, and so the number of high-threshold hits can be used to discriminate between the two. One of the identification schemes used within ATLAS typically achieves an efficiency between 89% and 95% for electrons and a rejection efficiency of 76% to 99% for pions [56]. The exact performance depends on $|\eta|$ and is better for high-p_{T} electrons and low-p_{T} pions.

A superconducting solenoid surrounds the Inner Detector, providing a 2 T magnetic field. This causes the charged particles inside the Inner Detector to follow helical trajectories. The curvature of the helix is inversely proportional to the transverse momentum of the particle, and hence the reconstructed tracks provide measurements of charged particle momenta. The sign of the charge is determined by the direction of the helix. For a particle with $p_{\mathrm{T}} = 30$ GeV and $|\eta| = 0.3$, the p_{T} resolution of the Inner Detector is around 2% [57]. However, the resolution worsens for particles with higher p_{T} or large $|\eta|$, as the track becomes straighter and the uncertainty in the curvature gets amplified when propogating it to the p_{T}. Tracks with large $|\eta|$ are straighter because the magnetic field is significantly weaker in the end-regions of the Inner Detector. For example, the p_{T} resolution degrades to 13% for a particle with $p_{\mathrm{T}} = 400$ GeV and $|\eta| = 0.3$ and to 6% for a particle with $p_{\mathrm{T}} = 30$ GeV and $|\eta| = 2.2$.

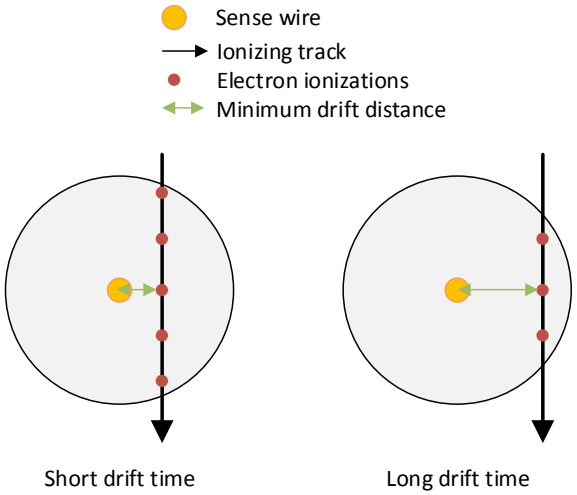

Figure 3.6: Illustration of how a straw tube can measure the position of a charged particle track along the width of the straw by examining the timing of the drift current. When the track passes close to the wire, the drift current arrives earlier and lasts longer than when the track is far from the wire.

A typical charged particle track leaves 3 hits in the Pixel Detector, 8 in the Semiconductor Tracker and 36 in the Transition Radiation Tracker. The high spatial resolution of the Pixel Detector and Semiconductor Tracker allow for high-precision measurement of the origin (also known as the vertex) and initial direction of the charged particle. The vertex is reconstructed with a resolution below 20 μm in the transverse direction [58], but the z-direction resolution depends on the number of tracks produced at that vertex. For a vertex with 10 tracks, the z-direction resolution is around 100 μm, but for a vertex with 70 tracks, it is around 30 μm. Although the Transition Radiation Tracker has a much lower spatial resolution than the other two systems, it can measure the curvature of the track much better, leading to a high-precision transverse momentum measurement. This is because it records many more hits across a relatively large range of distances from the interaction point.

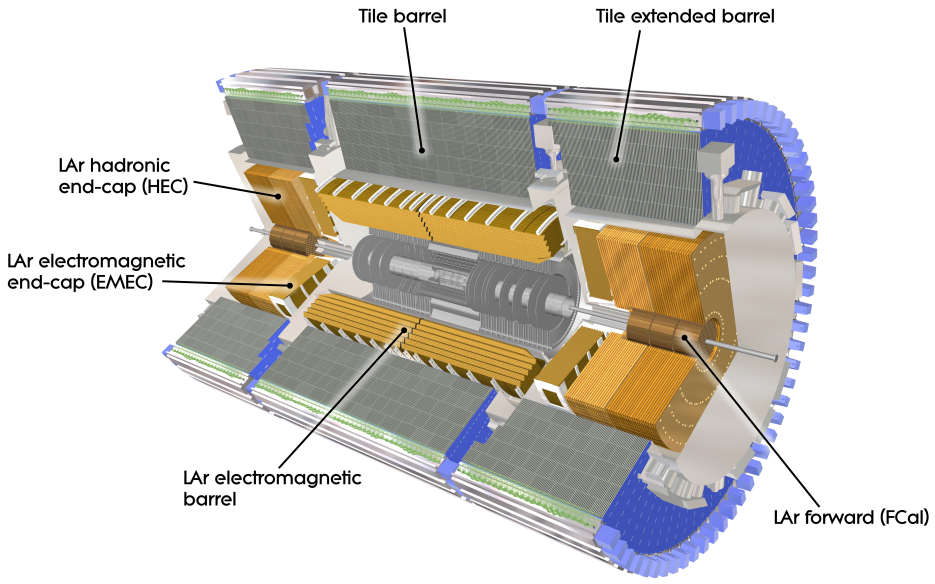

Figure 3.7: An overview of the Electromagnetic and Hadronic Calorimeter. Source: [59]

3.2.2 Electromagnetic Calorimeter

The Electromagnetic Calorimeter, shown in Figure 3.7, lies between the solenoid of the Inner Detector and the Hadronic Calorimeter, and absorbs and measures the energy of electrons and photons within $|\eta| < 3.2$. Within $|\eta| < 2.5$ it has three layers and for $2.5 < |\eta| < 3.2$ it has two layers. Although the exact granularity depends on the $|\eta|$ region, for the first layer it typically is 0.003125×0.1, for the second layer 0.025×0.025 and for the third layer 0.05×0.025 in $\Delta\eta \times \Delta\phi$. This results in approximately 160,000 readout channels. Each layer uses liquid argon (LAr) as an ionization material and lead plates as an absorber material. The lead plates and electrodes are interleaved in an accordion-like structure within the liquid argon.

Incident photons are absorbed by the lead plates and emit electron–positron pairs. As these electrons and positrons continue to pass through the lead plates, they slow down and radiate photons through bremsstrahlung. These photons can then go onto produce more positions and electrons and so on, until all the produced particles' energies are sufficiently

low such that pair production and bremsstrahlung can no longer occur. A similar story occurs with incident electrons and positrons producing a large number of low energy particles. This is known as an electromagnetic shower.

The electromagnetic shower must also be mostly contained within the Electromagnetic Calorimeter, so that as little as possible of the shower energy is lost and that other detector systems are minimally contaminated with the products of the shower. This suggests making the Electromagnetic Calorimeter extremely thick. However, there is a trade-off, as neutral and charged hadrons must pass through this before reaching the Hadronic Calorimeter. The thicker the Electromagnetic Calorimeter is, the larger the fraction of hadronic energy that is absorbed, which degrades the hadronic energy resolution. Electromagnetic showers can be characterized by their radiation lengths and hadronic showers by their interaction lengths. Both are defined as the distance over which the incident particle energy drops to $1/e$ of its original energy. The thickness of the Electromagnetic Calorimeter is greater than 22 radiation lengths and around two interaction lengths. This ensures that the electromagnetic showers are almost entirely captured and not too much hadronic energy is absorbed when hadrons pass through. For example, for an incident pion of 100 GeV, 35% of its measured energy is in the Electromagnetic Calorimeter [60] and the remainder is measured in the Hadronic Calorimeter.

When the particles produced in the electromagnetic shower pass through the liquid argon, they cause ionization. The ionization electrons then drift in an electric field and can be measured at the electrodes. As the energies of the shower particles are relatively low, the dominant interaction process is ionization and so most of the energy goes towards this. The energy deposited in the liquid argon can be measured by multiplying the number of electrons collected by the ionization energy of liquid argon. Much of the incident energy is, however, lost to ionization in the lead and other interaction processes, such as thermal excitation. For example, for an electron with $E = 100$ GeV, only 18% of its energy is collected by the

active material [61]. Calorimeters that produce and measure a particle shower to measure the energy of incident particles are known as sampling calorimeters.

Some incident electrons and photons begin showering before reaching the Electromagnetic Calorimeter through interactions with various detector material. To avoid losing this energy, an additional layer with just liquid argon and no lead absorber, known as the presampler layer, is placed before the first layer. This covers $|\eta| < 1.8$ and has granularity of 0.025×0.1. For an electron with $p_{\mathrm{T}} = 20$ GeV, 2–8% of its energy is deposited in the presampler layer, and this fraction decreases for more energetic electrons [62].

3.2.3 Hadronic Calorimeter

The Hadronic Calorimeter, shown in Figure 3.7, surrounds the Electromagnetic Calorimeter, and absorbs and measures the energy of hadrons within $|\eta| < 4.9$. It is composed of three systems that cover different $|\eta|$ ranges: the Tile Calorimeter covers $|\eta| < 1.7$, the LAr hadronic endcap covers $1.5 < |\eta| < 3.2$ and the LAr forward calorimeter covers $3.1 < |\eta| < 4.9$. All three systems are sampling calorimeters, and therefore work on a similar principle to the Electromagnetic Calorimeter. Hadronic showers, rather than only producing electrons, positrons and photons through pair production and bremsstrahlung like in electromagnetic showers, can produce a large variety of lower-energy particles through numerous processes, such as pions.

The thickness of the Hadronic Calorimeter is approximately 10 interaction lengths, again ensuring the showers are mostly captured. Highly energetic showers, however, can still punch through the Hadronic Calorimeter and deposit energy beyond it, which results in an energy measurement that is too low. If they deposit energy in the Muon Spectrometer, these signals can also be incorrectly detected as muons. Although real muons traverse the calorimeter, they only interact weakly with it and typically the energy loss is a few GeV [63].

The Tile Calorimeter is made up of three layers and has a granularity of 0.1×0.1 for the

first two layers and 0.2×0.1 for the last layer. This amounts to around 10,000 readout channels. Steel is used as the absorbing material and plastic scintillator tiles as the active material. When ionized, the plastic emits scintillation light that is captured by wavelength-shifting fibres and then detected and measured by a photomultiplier tube (PMT). The amount of electric charge collected is then proportional to the energy absorbed by the plastic. The energy scale is calibrated by passing a Caesium-137 radioactive source that produces photons with a well-known energy through the calorimeter. Again, much of the incident energy is lost to processes other than the ionization of the plastic. For example, for a pion with incident energy $E = 100$ GeV, only 3% of this is deposited in the plastic scintillator [64].

The LAr hadronic endcap is made up of four layers and has a granularity of 0.1×0.1 for $1.5 < |\eta| < 2.5$ and 0.2×0.2 for $2.5 < |\eta| < 3.2$. This amounts to around 5,000 readout channels. Unlike the Electromagnetic Calorimeter, copper is used instead of lead for the absorbing material, because the interaction length in copper is 25% shorter than in lead [65]. (The radiation length in lead is about half of that in copper, so lead is a good choice for the Electromagnetic Calorimeter.)

The LAr forward calorimeter is made up of three layers, has very coarse granularity and around 3,500 readout channels. The first layer uses copper plates as the absorber, but the other two layers use tungsten plates. Since there is no Electromagnetic Calorimeter coverage in this $|\eta|$ region, this calorimeter is designed to measure both electromagnetic and hadronic energies.

3.2.4 Muon Spectrometer

The Muon Spectrometer, the outermost subdetector of the ATLAS detector, detects muons and enables reconstruction of their momenta. It is composed of four systems covering $|\eta| < 2.7$, shown in Figure 3.8: Monitored Drift Tubes (MDTs), Cathode Strip Chambers (CSCs), Resistive Plate Chambers (RPCs) and Thin Gap Chambers (TGCs). Similar to the

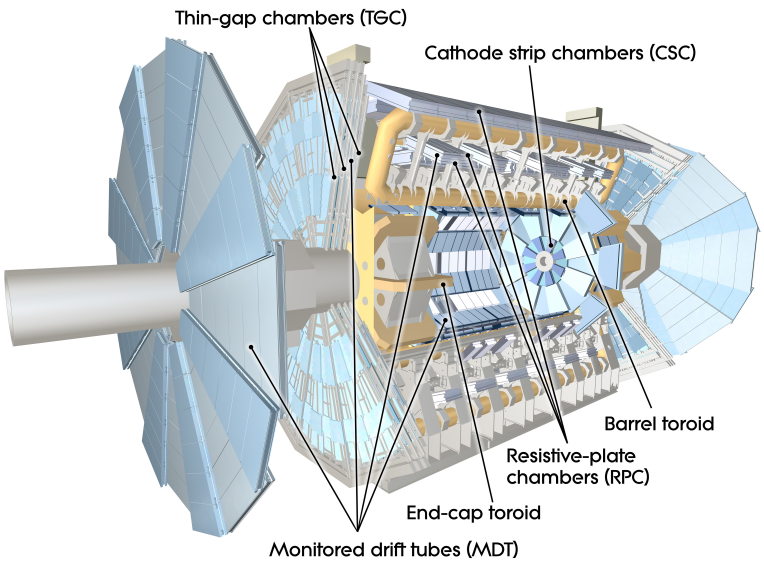

Figure 3.8: An overview of the Muon Spectrometer. Source: [66]

Transition Radiation Tracker in the Inner Detector, all four systems detect muons through the muons producing ionization electrons in a gas and then measuring a drift current with a large electric field applied. These position hits can then be reconstructed as tracks. Each system has three layers, with the exception of the Cathode Strip Chambers that only has one. A typical muon leaves 3 hits in the Monitored Drift Tubes (at large $|\eta|$, 2 hits in the MDTs and 1 hit in the CSCs) and 3 hits in either the Resistive Plate Chambers or the Thin Gap Chambers.

Monitored Drift Tubes provide coverage up to $|\eta| < 2.7$ (the first layer only provides coverage up to $|\eta| < 2.0$) and there are 350,000 of these proportional drift tubes. Each tube is 30 mm in diameter, is filled with a 93% argon and 3% carbon-dioxide gas mix and contains a high-voltage 0.05 mm tungsten-rehenium wire at its centre. Cathode Strip Chambers cover the missing $2.0 < |\eta| < 2.7$ gap in the first layer of the Monitored Drift Tubes with 31,000 readout channels. These chambers are multiwire proportional chambers and contain many cathode strips orthogonal to many anode wires in a single chamber filled with 80% argon and 20% carbon-dioxide. The position of the muon can be determined by interpolating

using the amount of charge collected on each strip and each orthogonal wire. Resistive Plate Chambers cover $|\eta| < 1.05$ and provide around 370,000 readout channels. These contain cathode strips orthogonal to anode strips in a chamber filled with 95% $C_2H_2F_4$. Thin Gap Chambers cover $1.05 < |\eta| < 2.7$ and provide around 320,000 readout channels. These are multiwire proportional chambers just like the Cathode Strip Chambers, with the main difference being they use a gas mixture of 55% carbon-dioxide and 45% n-pentane. Although the Monitored Drift Tubes can only measure one spatial dimension of a muon hit, the Cathode Strip Chambers, Resistive Plate Chambers and Thin Gap Chambers can measure both spatial dimensions.

One important distinction between these systems is how fast they react. The trigger system—the trigger determines which events are recorded for further analysis—must make a decision extremely quickly, within 25 ns, before the next bunch crossing. The Monitored Drift Tubes have a maximum drift time of around 700 ns, making them unsuitable to use as inputs to the trigger system. However, the Resistive Plate Chambers and Thin Gap Chambers have much smaller maximum drift times of around 5 ns, and so these are used for triggering on the presence of muons. These two systems achieve a fast response because the gap between the electrodes is much smaller, around 2 mm instead of 15 mm. Not only is the distance the ionization electrons must drift smaller, but the electric field is higher for the same applied voltage, increasing the drift velocity. Furthermore, the Resistive Plate Chambers run at a voltage more than three times higher than the Monitored Drift Tubes. Only the Thin Gap Chambers in $1.05 < |\eta| < 2.4$ are used, limiting the muon trigger acceptance to $|\eta| < 2.4$.

Three large superconducting air-core toroids provide up to a 4 T magnetic field in the muon spectrometer. Just like with the solenoid and the Inner Detector, the magnetic field bends the muons' tracks and enables measurement of their momenta.

CHAPTER 4

DATA, SIMULATED SAMPLES AND RECONSTRUCTION

4.1 Collection of Data

The studies in this thesis utilise data from pp collisions at a centre-of-mass energy of $\sqrt{s} =$ 8 TeV recorded by the ATLAS detector throughout the entire period of LHC operation during 2012. This data sample corresponds to an integrated luminosity of $\int \mathcal{L}\, dt = 20.3$ fb^{-1}. The uncertainty in the integrated luminosity, which is covered in more detail in Section 6.2, is $\pm 1.9\%$.

The amount of raw data produced by a single read-out of the entire ATLAS detector is around 1.3 megabytes [53]. If the data from every bunch crossing, also known as an event, were saved, this would require a storage system capable of recording over 40 terabytes per second at the nominal LHC bunch crossing rate of 40 MHz. Such a storage system would be extremely hard to build and be prohibitively expensive.

Instead, only data from the most interesting events is kept for further offline analysis. The system that decides in real-time which events are potentially interesting is called the trigger. The trigger is made up of three levels: the Level-1 (L1) trigger, the Level-2 (L2) trigger and the Event Filter (EF). These progressively reduce the event rate from the original 40 MHz down to a much more manageable 200 Hz through the use of various selection criteria. The Level-1 trigger is implemented in dedicated hardware, as it must make the acceptance decisions very quickly, in less than 2.5 μs. It only uses a very limited subset of detector information to reduce the rate to 75 kHz. The Level-2 trigger uses all the detector information within a geometrical region of interest identified by the Level-1 trigger to reduce the rate to 3.5 kHz, taking approximately 40 ms to decide for each event. The last level, the Event Filter, uses information from the entire detector to reduce the rate to the target 200 Hz, with an average processing time of approximately 4 s. The last two level are implemented in

software on commodity computers as this allows more complicated reconstruction algorithms and selection criteria to be used. Futhermore, it is also more flexible as this portion of the trigger can be updated and improved more easily.

The event selection of these studies require that events pass certain selection criteria in each level of the trigger, known as a trigger chain, that identifies the presence of a muon with a certain minimum p_{T} [67]. Within the Level-1 trigger, muons are identified through a spatial coincidence of three hits in either the Resistive Plate Chambers or the Thin Gap Chambers of the Muon Spectrometer and their p_{T} estimated from the amount of deviation of the three hits from a straight line. The trigger chains used require the Level-1 muon to have $p_{\mathrm{T}} > 15$ GeV. If the Level-1 trigger is passed, it sends a geometric region of interest of size 0.1×0.1 in $\Delta\eta \times \Delta\phi$ containing the muon to the Level-2 trigger. The Level-2 trigger constructs a muon track using a simple parametric function for speed from hits within the region of interest in the Monitored Drift Tubes of the Muon Spectrometer. It also finds the closest inner detector track and the muon p_{T} is estimated to be the average of the muon track and the inner detector track. The trigger chains used require the Level-2 muon to have $p_{\mathrm{T}} > 22$ GeV. Once the Level-2 trigger is passed, the Event Filter analyses the region of interest using offline reconstruction algorithms. First it forms a muon track from hits in the Muon Spectrometer and then it combines the muon track with an inner detector track to produce a so-called combined muon. Using this combined muon, the Event Filter evaluates the trigger chain's overall p_{T} requirement and track-based isolation can also be calculated. The muon trigger efficiency, shown in Figure 5.2, plateaus at around 70% for muons with $|\eta| < 1.05$ and around 85% for muons with $1.05 < |\eta| < 2.4$ for the trigger chains used in this analysis [67].

Once the trigger has accepted an event, the raw detector electronics read-out is recorded to persistent disk or tape storage at CERN. The raw data then undergoes reconstruction, which is described in Section 4.3.

4.2 Monte Carlo Simulation

When developing the measurement approach, the analysis is tested on simulated events corresponding to the W + jets signal process and the relevant background processes: QCD dijets, top-quark pairs, Z + jets and dibosons. Here an overview of how the simulated events are produced is given, and the details of the simulated samples used are given in the following sub-sections, Sections 4.2.1–4.2.5.

Events containing the final-state stable particles are created using a Monte Carlo (MC) generator. The generator first calculates the matrix elements of the specified physics process. It then randomly samples the phase space so that the hard scatter in each event is produced according to the probability distribution of kinematic configurations described by the calculated matrix elements. The products of the hard scatter then undergo parton showering and hadronisation within the generator.

The generator-level events are then processed by a full simulation of the ATLAS detector [68]. This uses the GEANT4 simulation toolkit [69] to simulate using Monte Carlo methods the interaction between the final-state stable particles and the material of the detector. The simulation considers all material throughout the detector, not just active material, so it includes items such as the physical support structure, the electronics, the cabling and the pipes.

In addition to the hard scatter, each simulated event is overlaid with additional simulated pp collisions. These are generated with PYTHIA v8.160 [33] using the ATLAS A2 set of tuned parameters (A2 tune) [70] and the MSTW 2008 LO PDF set [21]. The number of additional collisions is drawn from the predicted distribution of the average number of interactions per bunch crossing μ in 2012. However, since this was only a prediction, the MC events are reweighted so that the μ distribution in the MC sample matches the actual μ distribution in the 2012 data, shown in Figure 3.3. The simulated events can finally undergo the same reconstruction step that the data goes through, which is described in Section 4.3.

All samples are initially normalised to the cross-section calculated by the MC generator. For some samples, a scale factor is derived by dividing the inclusive cross-section calculated to a higher order by the inclusive cross-section from the generator. This scale factor is known as a k-factor and corrects the overall normalisation of the process.

The W + jets, dijets, $t\bar{t}$ and Z + jets samples also have an additional correction applied to the normalisation, derived from the comparison of data and MC simulations in the signal region and control regions. These data-driven corrections reduce the uncertainty in the theoretical modelling of the background caused by not including higher-order corrections. The process of deriving this correction is explained in more detail in Section 5.5.2.

Using the simulated MC samples, the expected performance of the measurement selection is evaluated and optimised in terms of quantities such as the signal efficiency and the background rejection. Ideally one would like to retain all the signal and throw out all the background, i.e. a signal efficiency of one and an infinite background rejection, but there is often a trade-off between the two. To find the best compromise, a sensitivity metric is introduced, defined as $S/\sqrt{B}$ where S is the number of accepted signal events and B is the number of accepted background events, and a selection that maximises this is chosen for the analysis. The basis of the metric is the statistical significance of the signal above a background-only hypothesis. Considering just statistical uncertainty and ignoring systematic uncertainties, the one standard deviation uncertainty in the background is $\sqrt{B}$, as it follows a Poisson distribution. Since $B \approx 500$ for the signal region of this analysis, the Possion distribution can be approximated as a normal distribution. As a result, $S/\sqrt{B}$ can be considered as a z-score.

Simulated events also contain additional information, such as the kinematics and decay tree of unstable particles and the kinematics of stable particles without detector effects. This additional information is known as *truth* information. By comparing truth with detector-level information, one can probe detector effects such as the efficiency and the spatial and

energy resolution of particle detection and reconstruction. Truth information is also used to study other things, such as the distribution of angular separation between the W boson and its decay muon shown in Figure 5.24.

For the measurement itself, simulated MC events are used to provide an estimate of background, which is subtracted from the data, and to correct for selection efficiency and detector effects in the measured distributions. This is covered in more detail in Section 5.5 and Section 5.8.

4.2.1 W + jets MC Samples

Events containing W + jets are generated with ALPGEN+PYTHIA6 [28, 30]. ALPGEN, a multi-leg leading-order MC generator, calculates the hard-scatter and PYTHIA6 with the P2011C tune [71] performs the parton showering and hadronisation. k-factors that correct the overall inclusive cross-section to a cross-section calculated to NNLO in QCD are applied. The setup is described in more detail in Section 2.4.1.

In addition to samples with events containing $W \to \mu\nu$ decays, samples with $W \to \tau\nu$ decays are used as well. This is because the τ-lepton can decay to a muon either directly or through a pion, allowing $W \to \tau\nu$ events to pass the analysis selection. $W \to e\nu$ samples are not used however, because only a negligble number of these events would pass the analysis selection since the $W \to e\nu$ decay does not produce a muon. Furthermore, the analysis selection requires no electrons be detected.

The samples have a generator filter that requires that each event contains a $R = 1.0$ anti-k_t truth jet with $p_{\mathrm{T}} > 250$ GeV. This saves storage space and computing time, as events that fail the filter would not pass the analysis selection requirement of the leading jet transverse momentum $p_{\mathrm{T}}^{j} > 500$ GeV and so are not needed to be saved, simulated or reconstructed. The p_{T} requirement of the generator filter must be significantly lower than that of the analysis selection to ensure that events are not missed. Due to detector effects,

such as the contamination from pile-up, the finite energy resolution and the uncertainty in energy scale calibrations, the reconstructed jet energy can be higher than the generator-level energy. As the p_{T} gap between the generator filter and the analysis selection is several times larger than these effects, only a negligble number of events fail the generator filter that would pass the analysis selection.

Another simulated sample of W + jets events is generated with PYTHIA8 [33] at leading-order using the setup described in Section 2.4.2. This contains events from all decay modes of the W boson. No k-factor is applied. Although this is not used for the measurement result, it is used for other studies and cross-checks. This sample has a generator filter that requires a $R = 0.6$ anti-k_t truth jet with $p_{\mathrm{T}} > 350$ GeV in each event.

More details of the W + jets samples, such as the number of events in each sample and their cross-sections, are listed in Table 4.1.

4.2.2 QCD Dijet MC Samples

QCD dijet events are generated at leading-order with PYTHIA v8.165 using the CT10 NLO PDF set [34]. No k-factors to correct the cross-section to include higher order corrections are applied. Although the leading-order cross-section may not be accurate, this is not a problem as the scaling procedure of Section 5.5.2 corrects the normalisation of the MC sample using data from a control region. Again to increase the efficiency of the generation as the analysis selection requires a muon with $p_{\mathrm{T}} > 25$ GeV, a generator filter is applied that requires each event to contain a muon with $p_{\mathrm{T}} > 3$ GeV. This muon can come from a variety of processes, such as in-flight pion decay and semi-leptonic b-hadron decay.

The events are generated such that the leading anti-k_t $R = 0.6$ truth jet p_{T} distribution is flat, and then they are sliced into different samples based on the leading jet p_{T}. This is done to ensure that there are sufficient statistics across a large range of jet p_{T}. A weight for each event is applied to recover the correct leading jet p_{T} distribution. The 200 GeV $<$

Generator	Process and Fiducial Region	No. of events	$\sigma \times \epsilon_{\text{filter}}$ [pb]	k-factor
ALPGEN + PYTHIA6	$W \to \mu\nu + 1p$, $p_{\text{T}}^{j} > 250$ GeV	160000	0.7064	1.133
	$W \to \mu\nu + 2p$, $p_{\text{T}}^{j} > 250$ GeV	425000	1.922	1.133
	$W \to \mu\nu + 3p$, $p_{\text{T}}^{j} > 250$ GeV	450000	2.125	1.133
	$W \to \mu\nu + 4p$, $p_{\text{T}}^{j} > 250$ GeV	304200	1.417	1.133
	$W \to \mu\nu + 5p$, $p_{\text{T}}^{j} > 250$ GeV	237750	1.061	1.133
	$W \to \tau\nu + 1p$, $p_{\text{T}}^{j} > 250$ GeV	159996	0.7047	1.133
	$W \to \tau\nu + 2p$, $p_{\text{T}}^{j} > 250$ GeV	425998	1.931	1.133
	$W \to \tau\nu + 3p$, $p_{\text{T}}^{j} > 250$ GeV	449996	2.142	1.133
	$W \to \tau\nu + 4p$, $p_{\text{T}}^{j} > 250$ GeV	302095	1.430	1.133
	$W \to \tau\nu + 5p$, $p_{\text{T}}^{j} > 250$ GeV	237599	1.070	1.133
	$W \to b\bar{b} + 0p + X$, $p_{\text{T}}^{j} > 250$ GeV	5000	0.01246	1.133
	$W \to b\bar{b} + 1p + X$, $p_{\text{T}}^{j} > 250$ GeV	30000	0.1198	1.133
	$W \to b\bar{b} + 2p + X$, $p_{\text{T}}^{j} > 250$ GeV	69898	0.2825	1.133
	$W \to b\bar{b} + 3p + X$, $p_{\text{T}}^{j} > 250$ GeV	181646	0.7321	1.133
	$W \to c\bar{c} + 0p + X$, $p_{\text{T}}^{j} > 250$ GeV	5000	0.01328	1.133
	$W \to c\bar{c} + 1p + X$, $p_{\text{T}}^{j} > 250$ GeV	48000	0.2244	1.133
	$W \to c\bar{c} + 2p + X$, $p_{\text{T}}^{j} > 250$ GeV	158798	0.6919	1.133
	$W \to c\bar{c} + 3p + X$, $p_{\text{T}}^{j} > 250$ GeV	421414	1.786	1.133
	$W \to c + 0p + X$, $p_{\text{T}}^{j} > 250$ GeV	30000	0.08747	1.52
	$W \to c + 1p + X$, $p_{\text{T}}^{j} > 250$ GeV	104896	0.4721	1.52
	$W \to c + 2p + X$, $p_{\text{T}}^{j} > 250$ GeV	121999	0.5700	1.52
	$W \to c + 3p + X$, $p_{\text{T}}^{j} > 250$ GeV	90000	0.3791	1.52
	$W \to c + 4p + X$, $p_{\text{T}}^{j} > 250$ GeV	79400	0.2991	1.52
PYTHIA8	$jj + W$ and $W + j$, $p_{\text{T}}^{j} > 350$ GeV	1999376	11.87	

Table 4.1: List of W + jets MC samples used. For the ALPGEN+PYTHIA6 samples, the filter on p_{T}^{j} is performed on $R = 1.0$ anti-k_t truth jets. For the PYTHIA8 sample, the filter on p_{T}^{j} is performed on $R = 0.6$ anti-k_t truth jets. No k-factor is applied to the PYTHIA8 sample.

Generator	Process and Fiducial Region	No. of events	$\sigma \times \epsilon_{\text{filter}}$ [pb]	k-factor
PYTHIA8	jj, $p_{\text{T}}^{j} = 200$ – 500 GeV, $p_{\text{T}}^{\mu} > 3$ GeV	3928796	40.55	
	jj, $p_{\text{T}}^{j} = 500$ – 1000 GeV, $p_{\text{T}}^{\mu} > 3$ GeV	1990150	0.2705	
	jj, $p_{\text{T}}^{j} = 1000$ – 1500 GeV, $p_{\text{T}}^{\mu} > 3$ GeV	1997238	0.0053401	

Table 4.2: List of QCD dijet MC samples used. The filter on p_{T}^{j} is performed on $R = 0.6$ anti-k_t truth jets. No k-factors are applied.

$p_{\text{T}}^{j} < 500$ GeV, 500 GeV $< p_{\text{T}}^{j} < 1000$ GeV and 1000 GeV $< p_{\text{T}}^{j} < 1500$ GeV samples are used. Events with $p_{\text{T}}^{j} < 200$ GeV at generator-level will not pass the analysis selection requirement of $p_{\text{T}}^{j} > 500$ GeV, so these samples can be omitted. The dijet cross-section for $p_{\text{T}}^{j} > 1500$ GeV is so small that a negligble number of dijet events from this kinematic region are expected in the signal region, so these samples can be omitted as well.

More details of the dijet samples, such as the number of events in each sample and their cross-sections, are listed in Table 4.2.

4.2.3 Top Quark Pair MC Samples

Events with top-quark pair production are generated at NLO in QCD with POWHEG r2129 [72–75] interfaced with PYTHIA v6.426 with the P2011C tune for parton showering and hadronisation. The CT10 NLO PDF set is used. A filter requires that each event contain at least one lepton, where a lepton here means an electron or a muon, with $p_{\text{T}} > 1$ GeV at generator-level. This effectively removes events from the all-hadronic decay mode of $t\bar{t}$, which without a muon would not pass the analysis selection anyway. A k-factor is applied to correct the cross-section of the sample to the cross-section calculated to NNLO in QCD. This NNLO calculation is performed by Top++ [76] and also includes resummation of next-to-next-to-leading logarithmic (NNLL) soft gluon terms. In this calculation, the top quark mass is set to $m_t = 172.5$ GeV and a combination according to the PDF4LHC prescription [77] of the MSWT 2008 NNLO, CT10 NNLO and NNPDF2.3 5f FFN NNLO [78] PDF sets is used.

Generator	Process and Fiducial Region	No. of events	$\sigma \times \epsilon_{\text{filter}}$ [pb]	k-factor
POWHEG+PYTHIA6	$t\bar{t} \to l + X$	14996424	114.5	1.1994

Table 4.3: List of $t\bar{t}$ MC samples used.

More details of the $t\bar{t}$ sample, such as the number of events it contains and its cross-section, is shown in Table 4.3.

Although a single top-quark produces a final-state that is considered by this analysis, the production cross-section for single top-quarks is so small that it is a negligble background for this analysis.

4.2.4 Z + jets MC Samples

Z + jets events are generated with ALPGEN+PYTHIA6 in exactly the same fashion as the ALPGEN+PYTHIA6 W + jets simulated samples of Section 4.2.1, with a couple of exceptions. The first difference is that no generator filter on the leading jet p_{T} is applied. The other difference is that Z + jets samples with explicit heavy-flavour production are not used to save on storage space. While using dedicated heavy-flavour samples like with W + jets would be more accurate, the background from Z + jets is small enough that the decreased accuracy has a negligble effect on the measurement. Since heavy-flavour samples are not used, the veto procedure to avoid double-counting heavy-flavour final states, described in Section 2.4.1, is not needed. More details of the Z + jets samples, such as the number of events in each sample and their cross-sections, are listed in Table 4.4.

4.2.5 Diboson MC Samples

Diboson events are generated at NLO in QCD with MC@NLO v4.07 [79], interfaced with HERWIG [80] and JIMMY [81] for parton showering and hadronisation. The CT10 NLO

Generator	Process and Fiducial Region	No. of events	$\sigma \times \epsilon_{\text{filter}}$ [pb]	k-factor
ALPGEN + PYTHIA6	$Z \to \mu\mu + 0p$	6298796	719.2	1.18
	$Z \to \mu\mu + 1p$	8193384	175.7	1.18
	$Z \to \mu\mu + 2p$	3175488	58.88	1.18
	$Z \to \mu\mu + 3p$	894799	15.67	1.18
	$Z \to \mu\mu + 4p$	393200	4.006	1.18
	$Z \to \mu\mu + 5p$	229200	1.254	1.18
	$Z \to \tau\tau + 0p$	19202764	718.9	1.18
	$Z \to \tau\tau + 1p$	10674582	175.8	1.18
	$Z \to \tau\tau + 2p$	3765893	58.86	1.18
	$Z \to \tau\tau + 3p$	1096994	15.67	1.18
	$Z \to \tau\tau + 4p$	398798	4.012	1.18
	$Z \to \tau\tau + 5p$	229799	1.256	1.18

Table 4.4: List of Z + jets MC samples used.

PDF set is used. Samples containing events with WW bosons and WZ bosons where at least one of the vector bosons decays leptonically are used. No k-factors are applied.

Events with ZZ bosons are not considered because the background from ZZ is negligble. This is because the cross-section for ZZ is significantly smaller than the cross-section for WW or WZ. Not only is the branching ratio of the Z boson to leptons approximately three times lower than that for the W boson, but the Z boson decay modes also have a lower probability of passing the analysis selection. This is because the analysis selection rejects events if two muons are selected and $Z \to \mu\mu$ produces two muons. $Z \to \tau\tau$ decays can produce exactly one muon, but the branching ratio of $\tau \to \mu\nu\bar{\nu}$ is less than twenty percent [82], so this does not occur too often.

An additional set of diboson samples are generated using SHERPA v1.4.1, a multi-leg leading-order MC generator, using the CT10 NLO PDF set. In addition to the leading-order diagram, diagrams with up to three additional partons in the hard scatter are considered. WW and WZ events where the W boson decays leptonically to either a muon or a tau and its associated anti-neutrino and the Z boson decays hadronically are used, as these are the dominant decay modes that pass the analysis selection. Again, events containing ZZ bosons

Generator	Process and Fiducial Region	No. of events	$\sigma \times \epsilon_{\text{filter}}$ [pb]	k-factor
MC@NLO	$WW \to l + X$	4977784	23.62	
	$W^+Z \to l + X$	999996	4.471	
	$W^-Z \to l + X$	488798	2.495	
SHERPA	$WW \to \mu\nu qq$	779898	7.297	1.06
	$WW \to \tau\nu qq$	789995	7.274	1.06
	$WZ \to \mu\nu qq$	209900	1.906	1.05
	$WZ \to \tau\nu qq$	210000	1.915	1.05

Table 4.5: List of diboson MC samples used. No k-factors are applied to the MC@NLO samples.

are not used. These additional samples are used to assess the theoretical uncertainty on the diboson background prediction in a procedure described in Section 6.3.2. k-factors are derived from comparing the SHERPA cross-section with the cross-section calculated at NLO in QCD by MCFM [83] using the CT10 NLO PDF, and these are applied.

Details of both sets of diboson samples, such as the number of events in each sample and their cross-sections, are shown in Table 4.5.

4.3 Reconstruction of Physics Objects

Each event from the raw data and the simulated MC samples undergoes a process known as reconstruction, where the output of the detector electronics is analysed to identify potential physics objects originating from the pp collisions. The primary physics objects that are used in these studies are muons and jets. The presence of a b-hadron inside a jet, indicating the jet is a so-called b-jet and originated from a b-quark, is also looked for during reconstruction, and this is used as part of the signal region and control region selections. Some quantities calculated during the analysis involve the neutrino from the W boson decay. The total vector sum of transverse momentum of all the produced particles should be equal to zero, but, as neutrinos are not directly detected and escape the detector, they can be indirectly

reconstructed through the imbalance of total transverse momentum. This is known as missing transverse momentum $E_{\mathrm{T}}^{\mathrm{miss}}$. Although electrons are not used, the analysis selection requires that there be no electrons detected and so electron reconstruction is needed. The algorithms to perform reconstruction of these physics objects are described in the following sub-sections.

4.3.1 Muon Reconstruction

The muons used in this analysis are formed from the combination of a track in the Inner Detector and a track in the Muon Spectrometer. Inner Detector tracks are reconstructed in two ways [84], the inside-out algorithm and the back-tracking algorithm. The inside-out algorithm starts by building the track from a seed of three hits in the silicon detectors. This preliminary track is then input into a Kalman filter, which provides an estimate of where the next hit is likely to be given the current knowledge of the track's parameters. If the next hit is found using the prediction, the Kalman filter is updated with this new information and it revises its estimates. This process of iteratively adding hits is repeated until the track is extended from near the interaction point to the outermost layer of the Inner Detector. The back-tracking algorithm works in much the same way as the inside-out algorithm, but instead starts with segments in the Transition Radiation Tracker and works backwards towards the interaction point. The inside-out algorithm is the primary algorithm by which Inner Detector tracks are reconstructed. The back-tracking algorithm is designed to increase the efficiency of reconstructing tracks from secondary particles, which are formed from primary particles interacting with detector material.

Muon Spectrometer tracks are reconstructed by a different algorithm, known as MUONBOY [85], that operates in four steps. First, regions of activity are identified using hits in the fast-reacting Resistive Plate Chambers and Thin Gap Chambers. Secondly, within the regions of activity local track segments are independently built in each of the three Moni-

tored Drift Tubes layers using straight lines. Approximating the local track segments with straight lines is sufficient because the muon's curvature in the magnetic field is much smaller than the distance between the hits within a layer. Thirdly, the local track segments from each layer are combined by considering which combinations of segments is compatible with the path the muon would take in the magnetic field. Lastly, all the hits from the three segments are refitted together in a so-called global fit to improve the reconstruction of the track's parameters.

After the Inner Detector and Muon Spectrometer tracks have been formed independently, they are then combined to form so-called combined muons using the STACO algorithm. Pairs of Inner Detector and Muon Spectrometer tracks are formed, and, for each pair, a chi-squared value is calculated that assesses how compatible the parameters of the two tracks are. Pairs with a chi-squared above 30 are removed. The pair with the lowest chi-squared value is selected and the parameters of the two tracks are statistically averaged using their covariance matrices to form a combined muon. All pairs that involve those two tracks are now removed, and the last step is repeated until no pairs remain. By adding information from the Inner Detector to the Muon Spectrometer track, the p_{T} resolution for muons with 6 GeV $< p_{\mathrm{T}} <$ 100 GeV is improved.

The efficiency of muon reconstruction in simulation is corrected through the use of a scale factor applied to each event. This is derived by dividing the efficiency in data by the efficiency in simulation. The efficiency in data was measured using the tag-and-probe method on events containing the decay of a Z boson to muons [86], as this has very high purity. This is shown in Figure 4.1. For a muon with $p_{\mathrm{T}} = 50$ GeV (the most common muon p_{T} seen in the signal region of this analysis), the reconstruction efficiency is above 97%. The scale factor is a function of the muon η and ϕ, as it was not found to depend on the muon p_{T} with any statistical significance. The red histogram in Figure 4.2 shows the distribution of the efficiency scale factor for simulated W + jets events in the signal region.

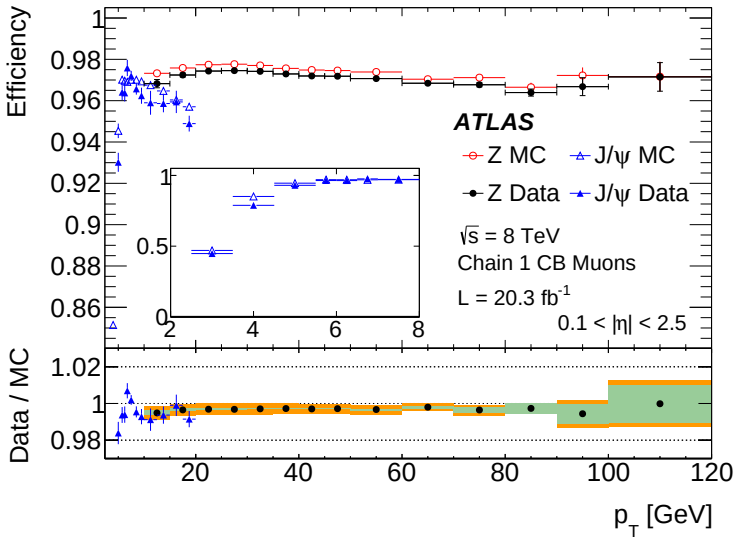

Figure 4.1: Efficiency of muon reconstruction as a function of p_{T} as measured in data and simulation using the tag-and-probe method on $Z \to \mu\mu$ and $J/\psi \to \mu\mu$ events. Source: [86]

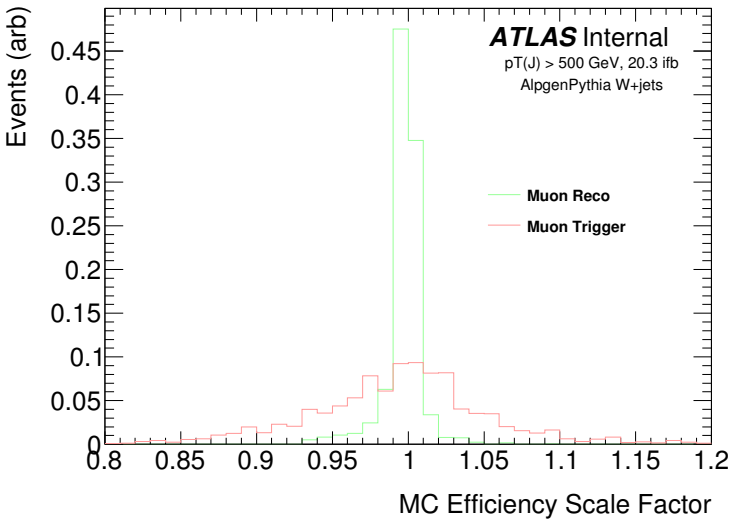

Figure 4.2: Distributions of the scale factors that are applied to simulated W + jets events in the signal region for correcting the muon reconstruction efficiency (red) and the muon trigger efficiency (green).

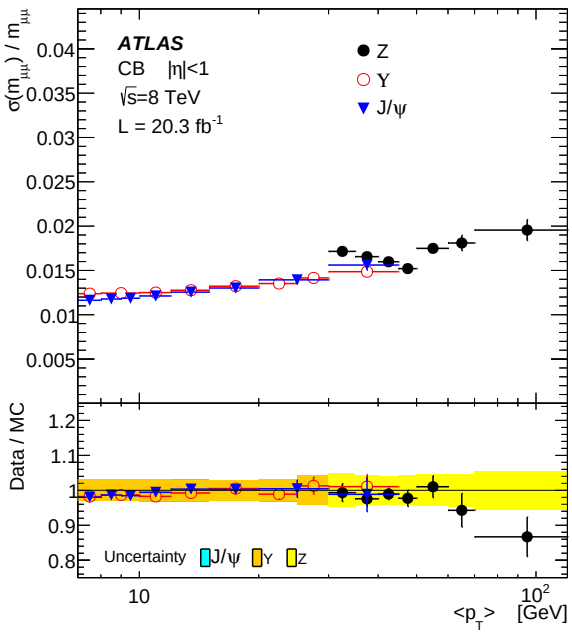

Figure 4.3: Muon energy resolution as a function of p_{T} for muons with $|\eta| < 1$ as measured in data using a dimuon mass resonance. Source: [86]

The muon energy scale and resolution are measured in data using the dimuon invariant mass peak of the Z boson in events, again, containing $Z \to \mu\mu$ decays. The energy resolution, shown in Figure 4.3, is around 1.5% for a muon with $p_{\mathrm{T}} = 50$ GeV and $|\eta| < 1.0$, typical of a muon in the signal region. The modelling of the energy scale and resolution of muons is corrected by applying a scale factor and Gaussian smear to the p_{T} of muons in simulated events. The scale factor and smearing width are a function of muon η and ϕ. The p_{T} of the Inner Detector track and the Muon Spectrometer track of the combined muons are corrected separately, and the combined p_{T} is recalculated with the STACO algorithm.

4.3.2 Jet Building

Jets are reconstructed by a clustering algorithm applied to energy deposits left in the Electromagnetic Calorimeter and the Hadronic Calorimeter by the narrow sprays of particles. Rather than use the individual calorimeter cells directly, jet reconstruction uses clusters of

three-dimensional topologically connected calorimeter cells [87], called topo-clusters. The advantage of this is that topo-clusters have better noise supression and better energy resolution after calibrations are applied.

To build topo-clusters, first the signal significance S of each cell is calculated as $S = E/\sigma_{noise}$, where E is the energy measured in the cell and σ_{noise} is the expected noise in the cell, including both electronic noise and noise from pile-up. Seed cells, defined as those with $S > 4$, form the initial topo-clusters. The neighbouring cells adjacent to the topo-clusters that have $S > 2$ are then added to expand the respective topo-clusters. If one of the neighbouring cells that is added belongs to another topo-cluster, the two topo-clusters are combined. This process of expanding the topo-clusters through the addition of neighbouring cells is repeated until there are no more neighbouring cells that meet the $S > 2$ requirement. Finally, all cells adjacent to each topo-cluster with $S > 0$ are also added. An example of building topo-clusters from seed cells and suitable neighbouring cells is shown in Figure 4.4. Requiring that the seed cells have $S > 4$ dramatically reduces the occurence of fake clusters from noise, but, at the same time, adding on neighbouring cells with a much less stringent S requirement minimises the number of cells with real energy deposits close to the noise levels that would be excluded.

After the topo-clusters are built, they are calibrated using a scheme known as local hadronic cell weighting (LCW). This attempts to correct for several effects such as the Hadronic Calorimeter and the Electromagnetic Calorimeter having different energy responses, the loss of real energy due to the topo-clusters' noise supression and the loss of energy in inactive detector material. These corrections are derived using MC simulations and use information about the shower obtained from the distribution of energy within each topo-cluster. Applying these corrections improves the resolution of jet energies and missing transverse momentum.

The anti-k_t jet clustering algorithm [88], implemented in the FastJet software package [89,

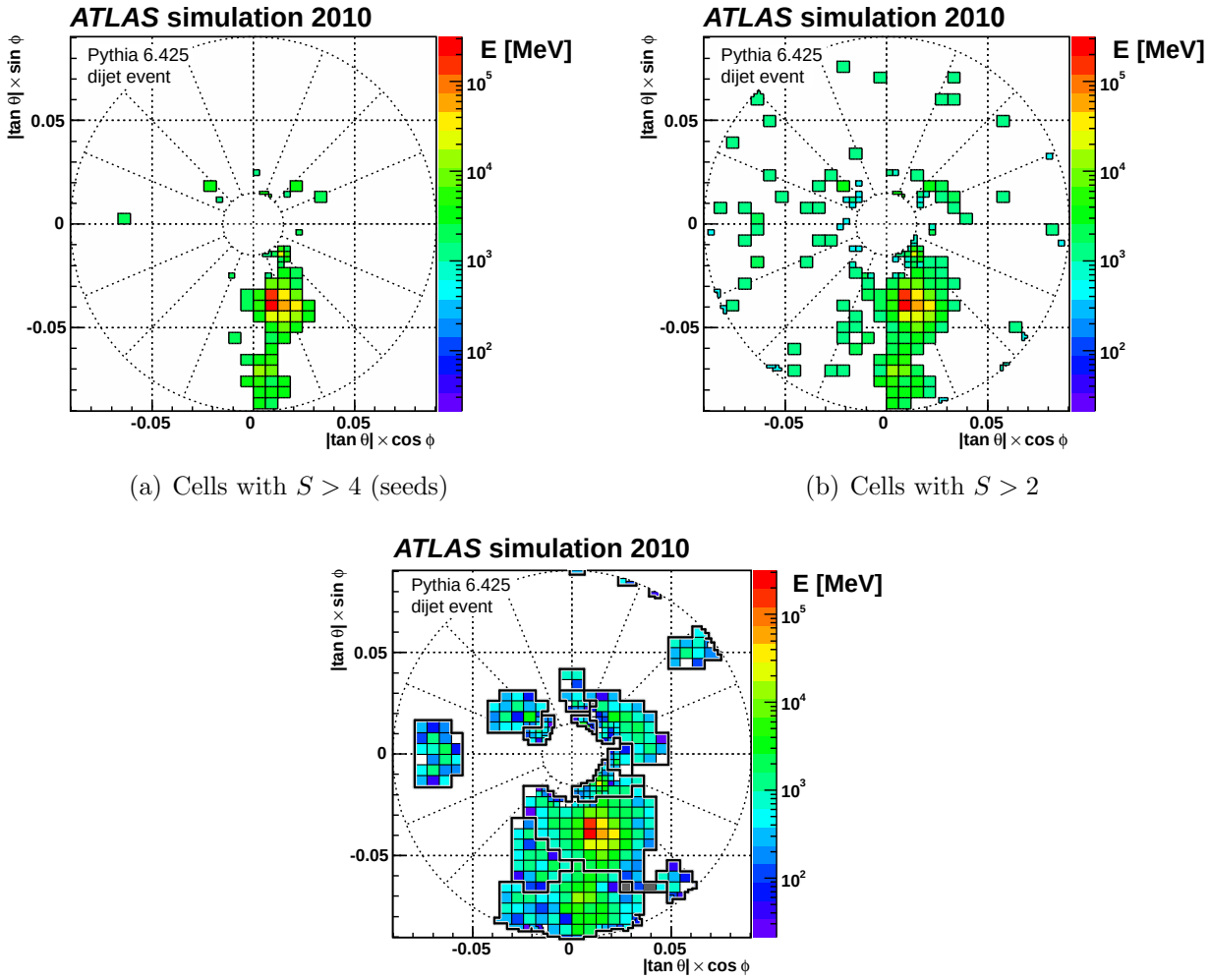

(a) Cells with $S > 4$ (seeds)

(b) Cells with $S > 2$

(c) Built topo-clusters

Figure 4.4: Cells in one layer of the calorimeter and the resulting topo-clusters for a single event. (a) shows seed cells with $S > 4$, (b) shows cells with $S > 2$ that are considered when iteratively adding on neighbouring cells to topo-clusters and (c) shows the resulting topo-clusters with a thicker black outline. Source: [87]

90], is used to build jets from topo-cluster constituents. The algorithm calculates for each constituent a stopping distance d_{iB} and for each possible pair of constituents a p_{T}-weighted distance between the two constituents d_{ij}. These metrics are defined as

$$d_{ij} = \min\left(\frac{1}{p_{\mathrm{T},i}^2},\ \frac{1}{p_{\mathrm{T},j}^2}\right)\frac{\Delta R_{i,j}^2}{R^2},$$
$$d_{iB} = \frac{1}{p_{\mathrm{T},i}^2},$$

where R is a radius parameter. If the smallest distance is a distance between two constituents, the two constituents are merged by adding their four-vectors together. If the smallest distance is a stopping distance for a constituent, this constituent is termed a jet and saved, and it is removed from the list of constituents. The algorithm then repeats until all constituents have been used up and clustered into jets. This is infrared safe and collinear safe, which means the jets found do not depend on collinear splittings or soft emissions. For this analysis, a radius parameter of $R = 0.4$ is used as this provides a good compromise between the jets being large enough to capture most of the shower and not being too large to reduce contamination from pile-up.

Reconstructed jets are calibrated using a series of four independent corrections [91]. The first attempts to mitigate the effects of pile-up by subtracting the expected pile-up contamination from each jet's p_{T}. The expected contamination is calculated for each jet as $\rho \times A_{\mathrm{j}et}$ [92], where ρ is the pile-up p_{T} density of the event estimated as the median p_{T} density of all k_t jets in the event and $A_{\mathrm{j}et}$ is the active area of the jet. The second corrects the direction of the jets so that they point to the event-specific primary vertex instead of the interaction point. The third calibrates the energy scale of the reconstruced jets to the energy scale of jets built with truth particles. A scale factor is derived by comparing the p_{T} and η of reconstructed jets with the p_{T} and η of their respective truth jets, in bins of jet p_{T} and η. The average jet energy response, which is the inverse of this scale factor, is shown

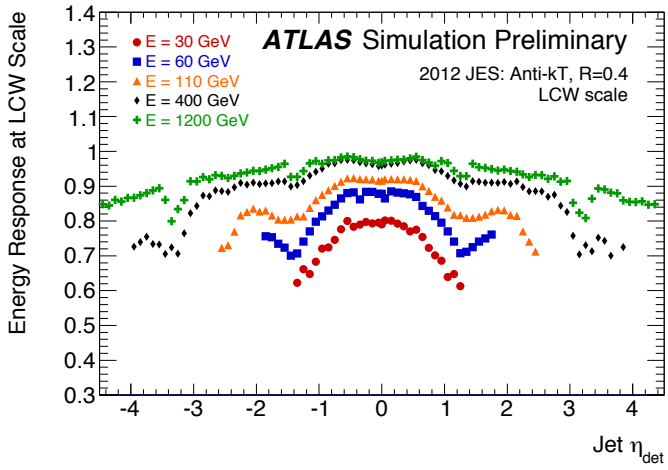

Figure 4.5: Average energy response as a function of $|\eta|$ for jets of different energies in simulated events. This is the inverse of the scale factor used in the energy scale calibration of reconstructed jets. Source: [93]

in Figure 4.5. The fourth is applied only to events from data to correct the energy scale in data to the energy scale in simulation. The energy scale is measured in-situ in both data and simulation by using events where a jet is recoiling against another object such as a photon or Z boson and the knowledge that the transverse momenta must balance. The ratio of the energy scale in simulation to that in data, as a function of jet p_{T} and η, is applied as a scale factor to the p_{T} of each jet in data. After calibration, the jet energy resolution, shown in Figure 4.6, is around 8% for a jet with $p_{\mathrm{T}} = 100$ GeV and decreases to around 4% for a jet with $p_{\mathrm{T}} = 500$ GeV [93].

4.3.3 Electron Reconstruction

Electrons are reconstructed by searching for a cluster of energy deposits in the Electromagnetic Calorimeter that are matched to an Inner Detector track [94]. The clusters of size $\Delta\eta \times \Delta\phi = 0.075 \times 0.125$ must satisfy $E_{\mathrm{T}} > 2.5$ GeV. When the track is extrapolated out to the Electromagnetic Calorimeter, it must be within $\Delta\eta < 0.05$ and $\Delta\phi < 0.05$ ($\Delta\phi < 0.2$

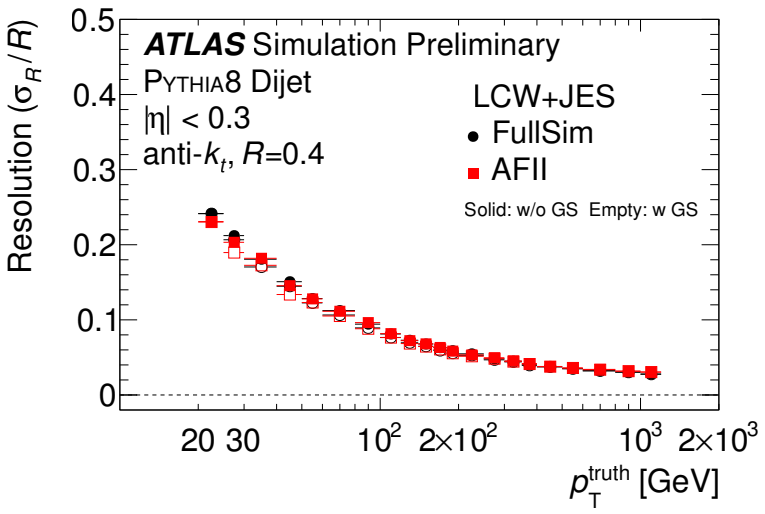

Figure 4.6: Jet energy resolution as a function of truth jet p_{T} in simulated dijet events. The black 'FullSim' data points are the relevant ones for this analysis. Source: [93]

if the track is on the side of the cluster that the track is bending towards to account for changes in direction due to bremsstrahlung) of the cluster. The track is also refitted using a track fitter that is optimised for electrons by considering bremsstrahlung. If multiple tracks match, the closest one is used.

The energies of the electron clusters are calibrated by applying a correction factor. This correction factor is derived from comparing cluster energies with truth electron energies in simulated events and training a multi-variate linear regression based on features of the electromagnetic shower and the position within the detector [95]. Using $Z \to ee$ events, the electron energy scale and resolution is measured in both data and simulation as a function of electron η. The energy resolution is around 2.2% for an electron with $|\eta| = 0.2$ and $E_{\mathrm{T}} = 25$ GeV and improves with increasing E_{T}. Another scale factor correction is applied to the energies in data events and a smearing is applied to the energies in simulated events so that the electron energy scale and resolution are consistent between data and simulation.

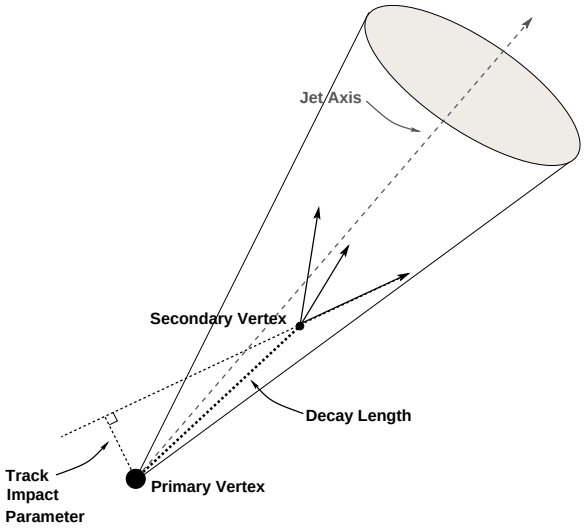

Figure 4.7: Illustration of a b-hadron decay creating a secondary vertex due to its relatively long lifetime. Source: [96]

4.3.4 Identification of b-hadrons

The proper lifetime of a typical b-hadron is around 1–1.5 ps [82], which is much larger compared to the lifetime of most other hadrons. As a result, b-hadrons can travel a few mm within the detector before decaying, resulting in a secondary vertex displaced from the primary hard-scatter vertex, illustrated in Figure 4.7. b-hadrons are also heavier than other hadrons, so they typically decay to a larger number of lighter particles. Their decays are also expected to be less collimated, as an approximate rule of thumb for the angular spread of a decay is $\Delta R \sim 2m/p_{\mathrm{T}}$.

To identify b-jets the MV1 tagging algorithm [97] is used, which exploits these characteristics of b-hadron decays. This is a perceptron neural network, trained on simulated events, that combines three different b-tagging algorithms—IP3D, SV1 and JetFitter—to produce a single discriminant variable. Through this combination the performance at rejecting light-flavour jets is improved by a factor of 2–3 than if just one algorithm were used. This is demonstrated in Figure 4.8, which shows light-flavour jet rejection versus b-jet tagging efficiency for MV1 and its three components. For the studies in this thesis, a MV1 discriminant

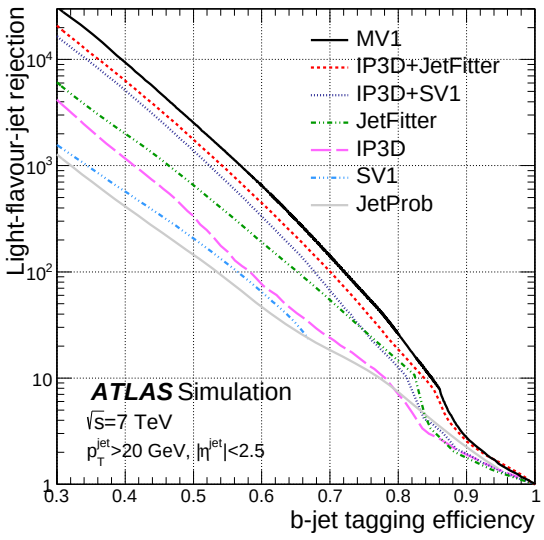

Figure 4.8: Light-flavour jet rejection versus b-jet tagging efficiency for the MV1 tagging algorithm in simulated events. Results are also shown for the three inputs of MV1: IP3D, SV1 and JetFitter. Source: [97]

threshold is chosen such that the efficiency of identifying a b-jet is 70% in simulated semi-leptonic $t\bar{t}$ events. This corresponds to an expected light-flavour jet rejection factor of 137, a c-jet rejection factor of 5 and a τ-jet rejection factor of 13.

IP3D looks at the transverse impact parameter d_0 and the longitudinal impact parameter z_0 with respect to the primary vertex of tracks within the jet, since tracks from a b-hadron decay do not originate from the primary vertex and therefore have large impact parameters. Using simulated events, a two-dimensional probability distribution is obtained for tracks from a b-jet and for tracks from a light-flavour jet. This is used to calculate the likelihood of the observed impact parameters being from a b-jet and being from a light-flavour jet. The log-likelihood ratio is then used as the IP3D discriminant, as this has the highest statistical power according to the Neyman–Pearson lemma [98].

SV1 looks at tracks within the jet that are displaced from the primary vertex—defined as those whose distance of closest approach d_{3D} satisifies $d_{3D}/\sigma(d_{3D})$ where $\sigma(d_{3D})$ is the uncertainty—and attempts to form a secondary vertex from them. Next the vertex mass,

defined as the invariant mass of all tracks associated with the secondary vertex, the vertex energy fraction, defined as the ratio of the energy of all tracks associated with the secondary vertex to the energy of all tracks within the jet, and the angular separation between the jet axis and the b-hadron flight path (the secondary vertex position minus the primary vertex position) are examined. b-jets have a much larger vertex mass and energy fraction than light-flavour jets. In a similar fashion to IP3D, these quantities are compared to probability distributions for b-jets and light-flavour jets, derived from simulation, and a log-likelihood ratio is used as the discriminant.

JetFitter [99] also looks for secondary vertices but does so in a different way compared to SV1. During the decay of a b-hadron, a c-hadron is often produced which also can travel a little bit before decaying, creating another secondary vertex. Rather than just construct one secondary vertex like in SV1, JetFitter attempts to find several under the assumption that they all lie along the same line as the b-hadron flight path. By searching for this cascade topology, the discrimination against light-flavour jets that do not have this topology is improved. The assumption of all the vertices lying on the same line increases the robustness of the vertexing fit. The following information is then examined and combined to form a discriminant using a neural network: the total vertex mass, the total vertex energy fraction, the average of each vertex's decay length divided by its uncertainty, the number of vertices with at least two associated tracks, the number of vertices with just one associated track and the number of tracks that are associated to a vertex with at least two associated tracks. The JetFitter discriminant is actually not one of the inputs of the MV1 algorithm, and the JetFitter+IP3D discriminant is used instead. JetFitter+IP3D is the same as JetFitter but the IP3D discriminant is also added as an input to the neural network.

The efficiency of b-tagging is measured in both data and simulation for light-flavour jets, c-jets [100] and b-jets [101]. A scale factor as a function of jet p_{T}, $|\eta|$ and flavour, calculated as the ratio of the efficiency in data to the efficiency in simulation, is applied for each b-

tagged jet to correct the b-tagging efficiency in simulation. A similar scale factor is derived for the inefficiency of b-tagging and is applied for each jet that is not b-tagged.

4.3.5 Missing Transverse Momentum

The missing transverse momentum is reconstructed by summing up vectorially the negative of the transverse momentum of all topo-clusters (described in Section 4.3.2) and all reconstructed muons (described in Section 4.3.1):

$$\vec{E}_{\mathrm{T}}^{\mathrm{miss}} = -\sum_{\text{topo-clusters}} \vec{E}_{\mathrm{T},i} - \sum_{\text{muons}} \vec{p}_{\mathrm{T},i}.$$

Calibrated muons and topo-clusters are used to improve the resolution. To further improve the resolution, topo-clusters that are associated with reconstructed physics objects—photons, electrons, τ-leptons and jets—are dropped and the calibrated energies of the physics objects are used instead. Low p_{T} particles sometimes do not reach the calorimeter or pass the noise threshold to form a topo-cluster, so tracks that are not associated with a physics object are also added to the missing transverse momentum calculation. If any of these tracks point to a topo-cluster, the topo-cluster is dropped to avoid double-counting the energy. This also improves the resolution because tracks have better resolution at low p_{T} than topo-clusters.

The resolution and scale of missing transverse momentum reconstruction is measured in data and simulation and is found to be in agreement [102]. The resolution goes approximately as $\sigma(E_{\mathrm{T}}^{\mathrm{miss}}) \sim 0.5\sqrt{\sum E_{\mathrm{T}}}$, where $\sum E_{\mathrm{T}}$ is the scalar sum of measured transverse energy in an event.

CHAPTER 5

DEFINITION OF THE MEASUREMENT

5.1 Baseline Event Selection

The topology of collinear W production involves a high-p_{T} jet that emits a W boson. At the LHC, the process with the largest cross-section that produces high-p_{T} jets is QCD dijets. To select this final state, the following baseline event selection is used:

- Events must contain at least one jet with $p_{\mathrm{T}} > 500$ GeV
- Events must have exactly one muon
- Events must have no electrons

The motivation behind this baseline event selection is explained in the following subsections. Further details on the exact selection used for jets, muons and electrons are also provided in Section 5.2.

5.1.1 High p_T Jet Requirement

As collinear W production originates from a high-p_{T} jet, events are therefore required to contain at least one jet with $p_{\mathrm{T}} > 500$ GeV. This lower bound on the jet p_{T} was found to be sufficient to probe the kinematic region of interest.

To estimate the probability p of a collinear W emission from such a jet, dijet events from a PYTHIA v8.210 MC simulation where the leading jet, defined as the jet with the highest p_{T}, has $p_{\mathrm{T}} > 500$ GeV are examined. The probablity of zero collinear W emissions from the two jets is $(1-p)^2$ as the emissions are independent. The probability of at least one

emission is then the complement of that:

$$\begin{aligned} P(\text{at least 1 emission}) &= 1 - P(0 \text{ emissions}) \\ &= 1 - (1-p)^2 \\ &= 2p - p^2. \end{aligned}$$

Since $p \ll 1$, this can be simplified to first-order as $P(\text{at least 1 emission}) \approx 2p$. This probability is equivalent to the fraction of events in the MC simulation that contain at least one emission. Through this, the probability of a collinear W emission from a jet with $p_{\mathrm{T}} > 500$ GeV is estimated to be 0.15%.

While this probability seems low, the production cross-section for dijets is several orders of magnitude larger than the back-to-back W + jets cross-section. When this is multiplied by the small collinear W emission probability to obtain the collinear W cross-section, it becomes comparable in magnitude to the back-to-back W + jets cross-section. As a result, over half of the production of W + jets in the phase space probed in this measurement is in the collinear region.

Although the topology of collinear W production involves two jets, a requirement for a second high-p_{T} jet is not applied. Even though both jets initially recoil from each other and have similar p_{T}, the jet that emits the collinear W boson can lose a significant amount of energy to the muon and neutrino, neither of which are reconstructed as part of the jet energy. The p_{T} of the W boson divided by the leading jet p_{T} is similar to the fraction of energy lost by the second jet due to the emission, and this is shown in Figure 5.1. On average, the collinear W carries away 40% of the emitting jet's p_{T}. Requiring a second high-p_{T} jet would therefore impose an implicit maximum on the energy carried by the W boson and its decay products. Not only would this reduce the overall number of collinear W events that are selected, it would also affect the shape of angular distributions that are measured. This

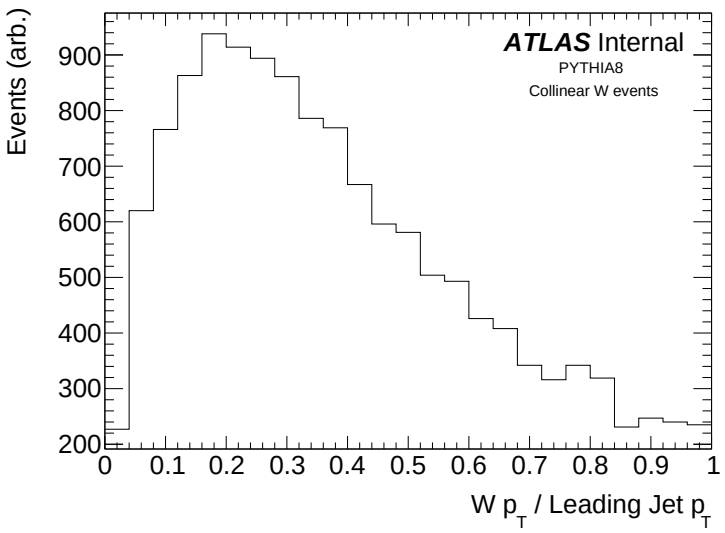

Figure 5.1: Distribution of W boson p_{T} divided by leading jet p_{T} in collinear W events generated using PYTHIA v8.210. This is similar to the fraction of energy lost by the emitting jet due to the collinear W emission. The leading jet is required to have $p_{\mathrm{T}} > 500$ GeV.

is because these angular quantities are functions of the kinematics of the event, including the energy of the W boson.

5.1.2 Single Muon Requirement

The analysis focuses exclusively on the leptonic decays of W bosons to muons, and thus events are required to have exactly one muon and pass a single-muon trigger. By requiring exactly one muon, there is no ambigiuity in choosing which muon to use for the calculation of ΔR. It also significantly reduces the background from Z + jets, which decays to a pair of muons. Some background from Z + jets, which is estimated to be 5% of the events in the signal region, is still present however, as one of its muons could be lost due to misreconstruction or being outside the kinematic acceptance of the muon selection. These inefficiencies occur for each muon with a probability of approximately 20%.

Initially the hadronic decay mode of W bosons was studied, as this is the exact final state that is a background to new physics searches that look for boosted hadronic top quarks.

As mentioned in Chapter 1, the potential of collinear W production to be a background for these searches is one of the main motivations of this study. In addition to measuring the rate of collinear W production, the analysis could have measured its effect on jet substructure, which is one of the main observables that boosted top-tagging algorithms use. Unfortunately though, making a measurement for the hadronic decay mode was not feasible. As stated in Section 5.1.1, the probability of a collinear W emission from a high-p_{T} jet is quite small, so it would be a small signal in the overall dijet topology. For example, using one of the approaches of Ref. [23] for a hadronic analysis would yield a signal purity of approximately 10% and only a few hundred signal events for an integrated luminosity of 20 fb^{-1} [43]. Considering that the statistical and systematic uncertainties on the dijet background could easily reach 10% as well, it would be very challenging to measure the signal with any significant confidence. Raising the leading jet p_{T} requirement would increase the signal purity, but would yield even fewer signal events. Therefore more data needs to be collected in order to make a hadronic analysis viable.

Using decays to electrons was also a possibility. However, the analysis probes topologies where the angular distance between the jet axis and the lepton is very small. Here the calorimeter energy deposits from the jet and from the electron are intermingled, potentially degrading the performance of electron reconstruction. Furthermore, the electron energy deposits would be included during the building of jets, affecting both the jet energy and its direction. Special care would be required to understand and correct for these effects. As a result, it was decided to focus on the muon channel due to its higher reconstruction purity and better understanding.

5.1.3 Electron Veto

Events that contain an electron are rejected. This reduces the background by removing mixed-flavour dileptonic (electron plus muon) $t\bar{t}$ decays. The only $t\bar{t}$ decay modes that

produce a final state involving exactly one muon are where one top quark decays semi-leptonically to produce a muon and the other top quark decays either semi-leptonically to produce an electron or a tau or decays hadronically. The branching ratio of a top quark decaying to produce an electron or a tau is approximately 13% for each mode [82]. For the hadronic decay, the branching ratio is approximately 67%. As a result, vetoing events with electrons reduces the background from $t\bar{t}$ by

$$\frac{\mathrm{Br}(t \to e\nu_e b)}{\mathrm{Br}(t \to e\nu_e b) + \mathrm{Br}(t \to \tau\nu_\tau b) + \mathrm{Br}(t \to q\bar{q}b)} \approx 14\%.$$

Rejecting events with an electron also ensures orthogonality with any future measurements performed in the electron channel. Although none are planned, this flexibility is a free bonus since the primary reason for the veto is the reduction in background from $t\bar{t}$.

5.2 Object Selection

5.2.1 Jet Selection

All jets used in the analysis, built as described in Section 4.3.2 using a radius parameter $R = 0.4$, are required to have $p_{\mathrm{T}} > 100$ GeV and $|\eta| < 2.1$. The value of this p_{T} requirement is chosen so that the selected jet closest to the muon is likely to be either the jet which emitted the W boson in the case of collinear W production or the recoiling jet in the case of back-to-back W + jets production. This was checked in the W + jets MC sample by comparing the distribution of angular separation between the muon and the closest jet to the distribution of angular separation between the muon and the quark or gluon that is created in the W boson's production vertex (obtained from truth information), and finding the two distributions to be similar. In particular, this p_{T} value is high enough to exclude jets originating from pile-up, as pile-up jets tend to have low p_{T}. At the same time, it is not too high to exclude the collinear W emitting jet, which can have significantly less energy

than the leading jet due to the emission.

At first, this study used so-called *fat* jets that were built using a radius parameter $R = 1.0$. Again this was to make the measurement more similar to the new physics searches that look for boosted hadronic top quarks, as they commonly use these fat jets to capture the entire top quark decay inside a single jet [103]. Since these larger jets are more suspectible to collecting contributions from pile-up, as they have a larger active area, a grooming procedure called trimming [104, 105] was used to mitigate this. The distribution of angular separation between the muon and the closest jet was evaluated in simulated W + jets events using $R = 0.4$ jets and $R = 1.0$ jets, and the two distributions that resulted from these different choices for the jet radius were found to be very similar. Given their similar results, the measurement uses jets built with a radius parameter $R = 0.4$, because these smaller jets have a much lower systematic uncertainty in their energy scale. For example, for a jet with $p_{\mathrm{T}} = 500$ GeV, the uncertainty in p_{T} with $R = 1.0$ jets is twice that with $R = 0.4$ jets [106, 107].

To reject fake jets that are caused by non-collision background, all jets are required to satisfy the loosest jet-quality requirements discussed in Ref. [108]. These criteria are designed to reject approximately 50% of fake jets from beam-induced background, cosmic rays and calorimeter noise, while maintaining an efficiency for real jets of greater than 99.8%. The addition of this requirement causes the number of signal region events observed in data to decrease by one, so the impact of fake jets and the quality criteria are negligble for this analysis.

As electrons deposit energy in the calorimeter, they can also be reconstructed as additional jets. Typically to avoid these additional non-hadronic jets, jets that are close to signal electrons are removed. This is called overlap removal. The baseline selection of the analysis requires events to have no isolated electrons with $p_{\mathrm{T}} > 20$ GeV (the electron selection is described in more detail in Section 5.2.5). As a result, jets formed from an electron must have $p_{\mathrm{T}} < 20$ GeV. Since the jets used in this analysis are required to have $p_{\mathrm{T}} > 100$ GeV,

these non-hadronic electron jets can be ignored and overlap removal is not necessary.

5.2.2 Trigger Selection

Events used in this analysis are selected by requiring that they pass at least one of two single-muon triggers [67]. The first trigger requires an isolated muon with $p_{\mathrm{T}} > 24$ GeV. The second trigger requires a muon with $p_{\mathrm{T}} > 36$ GeV with no isolation criteria applied. These p_{T} thresholds are the lowest values that maintain the accepted event rate within the budget allocated to the muon trigger for recording data events. The track-based isolation used in the first trigger requires that the scalar sum of the p_{T} of all tracks with $p_{\mathrm{T}} > 1$ GeV within a cone of radius $\Delta R = 0.2$ around the muon is less than 12% of the muon p_{T}. This isolation value was chosen as it rejects approximately 50% of muons from semi-leptonic b-decays and pion and kaon decays, but accepts almost 100% of muons from $Z \to \mu\mu$ events.

Some triggers do not record every event that passes the selection. This is known as pre-scaling, which reduces the effective integrated luminosity of the recorded dataset. Both triggers that are used in this analysis were not pre-scaled for any of the 2012 data-taking, enabling access to the entire integrated luminosity.

The efficiency of the muon trigger as a function of the muon η and ϕ has been measured in data, primarily using the decay of Z bosons to muons. These results were then compared to predictions from MC simulation, and the ratio of the two calculated. To correct the simulated trigger efficiency, the ratio is used as a scale factor applied to each simulated event. The green histogram in Figure 4.2 shows the distribution of these corrections for simulated W + jets events in the signal region.

5.2.3 Muon Selection

Muons, reconstructed as described in Section 4.3.1, are required to have $p_{\mathrm{T}} > 25$ GeV and $|\eta| < 2.4$. Although the first muon trigger looks for a muon with $p_{\mathrm{T}} > 24$ GeV, the efficiency

as a function of muon p_{T} has a turn-on curve and does not reach the peak efficiency plateau until a higher muon p_{T} is reached. This is shown in Figure 5.2. Within the region of the turn-on, the difference between the efficiency in data and simulation is much larger, as the efficiency is rapidly changing, and, despite the efficiency correction described in Section 5.2.2, small discrepencies are amplified. As a result, the uncertainty in the trigger efficiency is also much larger in this region. By selecting muons with $p_{\mathrm{T}} > 25$ GeV, the peak efficiency plateau is reached and the turn-on region avoided, reducing the uncertainty. The discrepency in efficiency between data and simulation at high p_{T} for $|\eta| < 1.05$ is not a significant concern, because the efficiency correction addresses this and the uncertainty in the correction for this region is still small. The η requirement ensures the muons are within the geometric acceptance of the Level-1 muon trigger, described in more detail in Section 3.2.4.

To reduce contamination from semi-leptonic b-decays, in-flight pion and kaon decays and cosmic muons, the muons' longitudinal impact parameter with respect to the primary vertex z_0 must satsify $|z_0| \sin\theta < 0.5$ mm and their transverse impact parameter with respect to the primary vertex d_0 must satisfy $|d_0|/\sigma(d_0) < 3$, where $\sigma(d_0)$ is the uncertainty in d_0. This is effective because muons from semi-leptonic b-decays, pion and kaon decays are not produced immediately after the hard scatter, due to the longer lifetime of b-hadrons, pions and kaons, and instead are produced later at some distance away from the primary vertex. In the case of cosmic muons, this is extremely effective as it is highly unlikely the cosmic muons would pass through the primary vertex.

In order to ensure the muons have been reconstructed with sufficient quality, requirements are placed on the inner detector track of the reconstruced muons. The inner detector track must consist of at least one hit in the Pixel detector, at least five hits in the SCT detector and at least one hit in the b-layer if a hit in the b-layer is expected. It must also have at most two holes, where a hole is defined as a sensor that is traversed by the track but does not register a hit. When a track crosses a sensor that is known to be dead from the time-

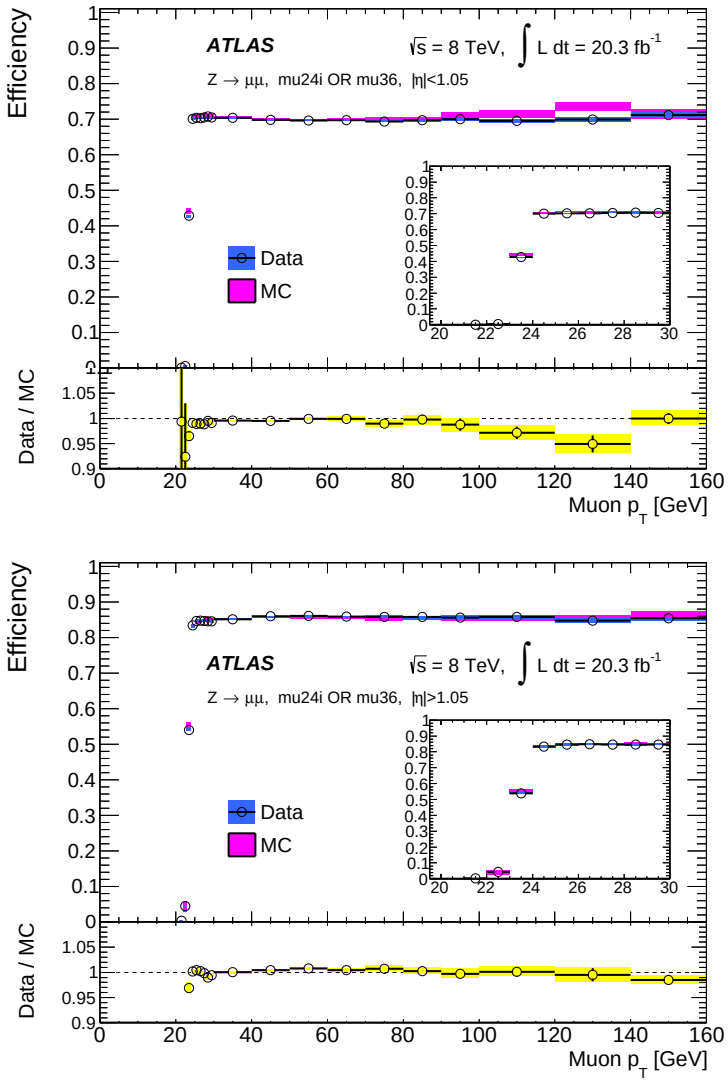

Figure 5.2: Efficiency of passing the muon trigger as a function of muon p_{T} for muons with $|\eta| < 1.05$ (upper) and muons with $1.05 < |\eta| < 2.4$ (lower) as measured in data (black circles) and in MC simulation (purple band). The error bars and bands include both statistical and systematic uncertainties. The lower panel shows the ratio of data to MC simulation. Source: Figure 8 of Ref. [67]

dependent detector conditions database, the sensor is included in the counting of hits and ignored in the counting of holes. If the track is within the geometric acceptance of the TRT detector ($0.1 < |\eta| < 1.9$), the track must be able to be extended within the TRT detector. An extension is considered successful if there are at least six TRT hits and outliers and the outliers comprise less than 90% of this sum.

There is no requirement for the muons to be isolated at this stage. As a result, the exactly one muon requirement of the baseline event selection is more stringent, as events with a second muon that is non-isolated will be rejected. If isolation were applied at this stage, the second non-isolated muon would not be selected, the events would only have one selected muon and would not be rejected. This has the effect of reducing the background from $t\bar{t}$ by 3% and the background from Z + jets by 9%, as both of these processes can produce multiple muons. Isolation requirements on the single selected muon are peformed later during the signal region and control region selections.

The single offline reconstructed muon that is selected must also be consistent with the online trigger muon that fired the muon trigger. The consistency is checked by requiring the angular distance between the offline and online muon $\Delta R(\text{offline } \mu, \text{online } \mu) < 0.1$.

5.2.4 Number of b-tagged Jets

The number of b-tagged jets for a given event is calculated using the MV1 tagger. As described in Section 4.3.4, this algorithm is used to identify jets that contain a b-hadron with an efficiency of 70%. The jets considered for b-tagging have $p_{\mathrm{T}} > 25$ GeV and $|\eta| < 2.1$.

5.2.5 Electron Selection

Electrons, reconstructed as described in Section 4.3.3, are required to have $p_{\mathrm{T}} > 20$ GeV. The calorimeter cluster that forms them must also have $|\eta| < 2.47$ to remain within the geometric acceptance of the inner detector, excluding the crack region of $1.37 < |\eta| < 1.52$

where there is no calorimeter coverage. To avoid selecting electrons that are produced as part of a jet, the electrons are required to be isolated. This isolation is track-based and requires that the scalar sum of the p_{T} of all tracks with $p_{\mathrm{T}} > 1$ GeV in a cone of radius R = 0.2 around the electron be less than 15% of the electron p_{T}.

To reduce contamination from semi-leptonic b-decays, the electrons' longitudinal impact parameter with respect to the primary vertex z_0 must satsify $|z_0| \sin\theta < 0.5$ mm and their transverse impact parameter with respect to the primary vertex d_0 must satisfy $|d_0|/\sigma(d_0) < 3$. Cosmic muons through interactions with inner detector material can also produce electrons [109]. These would also be reduced by the above impact parameter requirements.

To avoid fake electrons from being selected, the electrons must meet a set of identification criteria. The *medium* criteria of Ref. [94] are used. These use attributes of the shower shape, the inner detector track quality and the matching between the calorimeter cluster and the inner detector track to identify electrons with high efficiency. For electrons that originate from a $Z \to ee$ decay, these criteria achieve an identification efficiency of approximately 85%. The same calorimeter cluster can sometimes be reconstructed both as an electron and as a photon. To avoid this ambiguity where the electron could actually be a photon, only electrons that are reconstructed solely as electrons are used.

To ensure the electrons have been reconstructed with sufficient quality, all the calorimeter cells that make up the electron cluster are examined. If any of them have a known problem, the electron is not selected.

5.3 Event Quality Pre-selection

Although the bulk of data that has known quality problems is ignored through the good run list, there can be additional quality problems. The Liquid Argon calorimeter can suffer from noise bursts and data corruption, and data events that are affected by this are vetoed.

Similarly, the Tile calorimeter also can experience data corruption and affected events are removed as well. Ocasionally the timing, trigger and control systems for the detector need to be restarted during a run. Immediately after such a restart, there can be events that have incomplete information from the detector and these are ignored.

For a small amount of time, there was a Tile calorimeter module that reported erroneous energy deposits, and these were not removed before reconstruction was performed. Therefore, events recorded during this time with a jet that is near this module and that has its highest energy fraction in the Tile calorimeter's second layer and that this fraction is more than 60% of the overall jet energy are vetoed.

Throughout the year, there was a persistent problem with Tile calorimeter modules going offline due to various reasons. Although a correction is applied to jets that overlap with or are adjacent to dead modules, it was discovered that this correction was not adequate. In particular, high p_{T} jets such as the ones used in this analysis are particularly affected. This is because high p_{T} jets are more collimated and so a greater fraction of their energy can fall into the small region of a dead module where the correction is used. Figure 5.3 shows the distribution of leading jet η and ϕ from data where the leading jet has $p_{\mathrm{T}} > 1500$ GeV during a time where there are two dead modules. The regions covered by these dead modules are indicated with arrows. The inadequacy of the correction for high p_{T} jets can be seen through the deficiency of events in the two regions of the dead module. To avoid this problem, the list of dead Tile modules is retrieved for each data event and the event vetoed if a jet, reconstructed using non-dead modules in other layers of the Tile calorimeter and the Liquid Argon calorimeter, falls into a dead module. Data events where a jet is adjacent to a dead module are also vetoed if the jet's properties form a combination known to cause problems. This procedure causes a small ineffeciency in data, so the same ineffeciency must be emulated in MC simulation as well. This is done by assigning a random run and lumiblock number, weighted by their integrated luminosity in data, to each simulated event. The dead modules

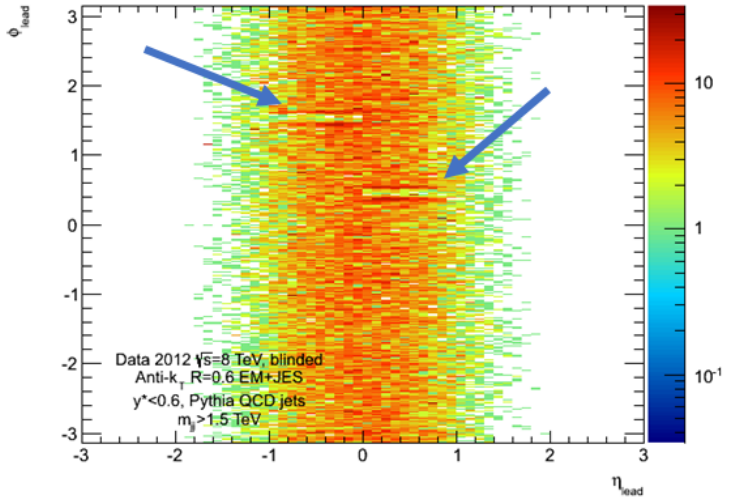

Figure 5.3: Distribution of leading jet η and ϕ from data where the leading jet has $p_{\mathrm{T}} > 1500$ GeV before the dead Tile calorimeter module veto is applied. Two dead Tile modules are present, whose coverage regions are indicated with arrows. Source: Ref. [110]

for this run and lumiblock number are then looked up, and the same event veto criteria are applied to MC simulation. This procedure is validated by finding the leading jet η and ϕ distribution after the event veto to be consistent between data and MC simulation.

5.4 Signal Region Selection

To select the W + jets signal, events are required to meet the baseline event selection: contain at least one jet with $p_{\mathrm{T}} > 500$ GeV, exactly one muon and no electrons. Additionally they must contain no b-tagged jets, the muon must be isolated and the distance between the muon and the closest jet must satisfy $\Delta R > 0.2$. This signal region (SR) selection achieves a purity of 82% and the composition of the background is shown in Table 5.1 for the region of $0.2 < \Delta R < 2.4$, the region of $\Delta R > 2.4$ and inclusively. Collinear W boson production is the dominant process for events with $\Delta R < 2.4$, and thus $\Delta R < 2.4$ is referred to as the collinear region. For events with $\Delta R > 2.4$, the W boson is balanced by a hadronic recoil that may consist of one or more jets, and thus $\Delta R > 2.4$ is referred to as the back-to-back

Signal Region			
Process	$0.2 < \Delta R < 2.4$	$\Delta R > 2.4$	Inclusive
Dijets	5%	2%	4%
$t\bar{t}$	7%	2%	5%
Z + jets	6%	4%	5%
Dibosons	2%	4%	3%
W + jets	80%	88%	82%
Events in Data	1907	833	2740

Table 5.1: The number of events in the signal region (defined in Section 5.4) observed in data, along with the composition of these events as predicted by MC simulation, split by the angular seperation between the muon and the closest jet. The dijet, $t\bar{t}$ and Z + jets backgrounds have been scaled according to their respective control regions. The W + jets signal has been scaled by 0.71.

region. The motivation behind this selection is explained in the following subsections.

5.4.1 Zero b-tagged Jets

Although there can be b-hadrons in the final state of collinear W production, for example from gluons in the jets that split to a pair of b-quarks, in general, signal events do not have any b-hadrons. However, this is not true for the background from $t\bar{t}$, which generates two b-quarks in their decay. The predicted distributions from MC simulation of the number of b-tagged jets per event for the signal and background processes are shown in Figure 5.4, where it can be seen that the distribution for $t\bar{t}$ in red is very different from the distribution for W + jets in green. Requiring that each event have zero b-tagged jets reduces the background from $t\bar{t}$ by over 80%, while only 10% of the W + jets signal is rejected.

5.4.2 Muon Isolation

In collinear W production, as the muon is produced from the decay of a W boson, it is expected that the muon will be isolated. On the other hand, in dijet events muons mostly

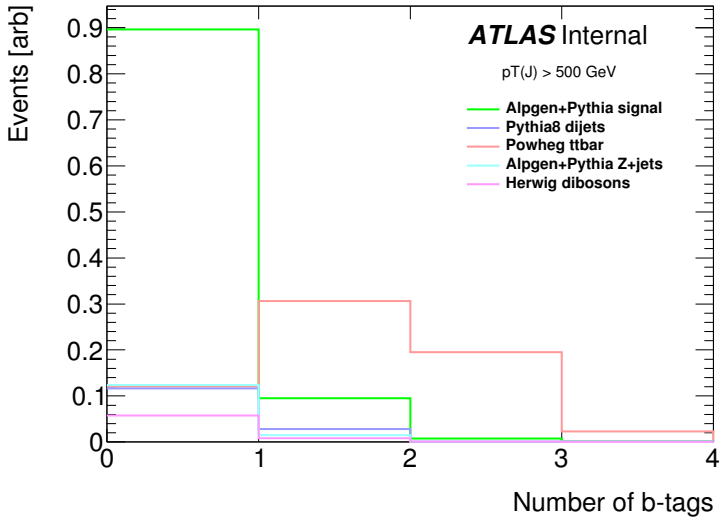

Figure 5.4: Predicted distributions from MC simulation of the number of b-tagged jets per event for the signal and background processes. Here the signal region selections are applied, except for the requirement on the number of b-tagged jets. The signal and total background are both normalized to unity.

originate from heavy-flavour or in-flight pion and kaon decays, and these muons tend to be non-isolated as they are within the core of a jet. As a result, for this measurement the muon is required to be isolated, and this reduces the background from dijet events by over 97%, while retaining over 95% of the W + jets signal.

Both track-based and calorimeter-based isolation criteria are used. The track isolation requires that the scalar sum of the p_{T} of all tracks with $p_{\mathrm{T}} > 1$ GeV in a cone of radius $\Delta R = 0.2$ around the muon be less than 10% of the muon p_{T}. The first muon trigger that is used has a similar track isolation requirement but with a looser cut of 12%. The tighter track isolation requirement of 10% used here ensures that the trigger efficiency reaches its peak plateau efficiency. The calorimeter isolation requires that the scalar sum of the p_{T} in all calorimeter cells in a cone of radius $\Delta R = 0.2$ around the muon be less than 40% of the muon p_{T}. Calorimeter cells that are very close to the muon track (the distance considered as close varies for each calorimeter layer) are excluded in the summation [111], as they contain energy deposits from the muon itself. The predicted distributions from

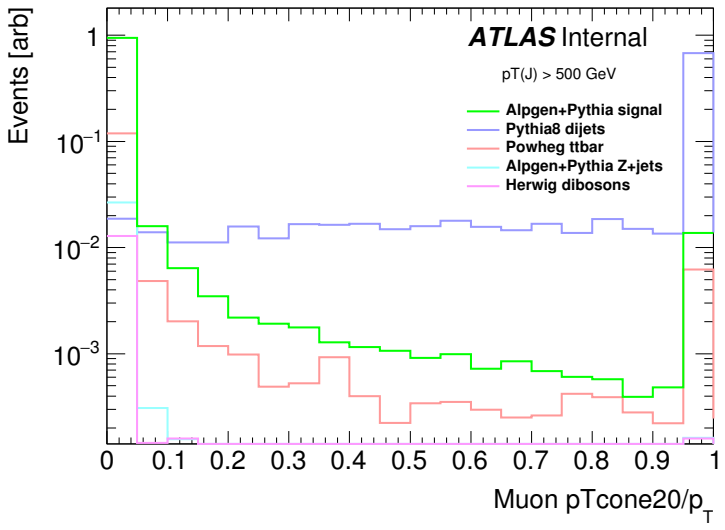

Figure 5.5: Predicted distributions from MC simulation of track isolation energy for the signal and background processes. Track isolation energy is defined as the scalar sum of the p_{T} of all tracks with $p_{\mathrm{T}} > 1$ GeV in a cone of radius $\Delta R = 0.2$ around the muon divided by the muon p_{T}. Here the baseline event selections are applied. The signal and total background are both normalized to unity. The rightmost histogram bin includes overflow values that are larger than the axis range of the plot.

MC simulation of track isolation energy and calorimeter isolation energy for the signal and background processes are shown in Figure 5.5 and Figure 5.6 respectively.

The efficiency of the isolation requirement was studied both in simulated samples and in situ using data events containing high-p_{T} top quarks, and the results from the two studies were in agreement. These results are shown in Figure 5.7 and the method is described in more detail in Appendix A.1. However, in the extremely collinear region, where the distance between the muon and the closest jet is $\Delta R < 0.2$, the limited size of the event sample did not allow the same conclusion. In order to be conservative, events where $\Delta R < 0.2$ are also excluded to avoid this region which could not be validated. This has a relatively minor effect on the overall signal selection efficiency, as approximately only 2% of the W + jets signal is removed.

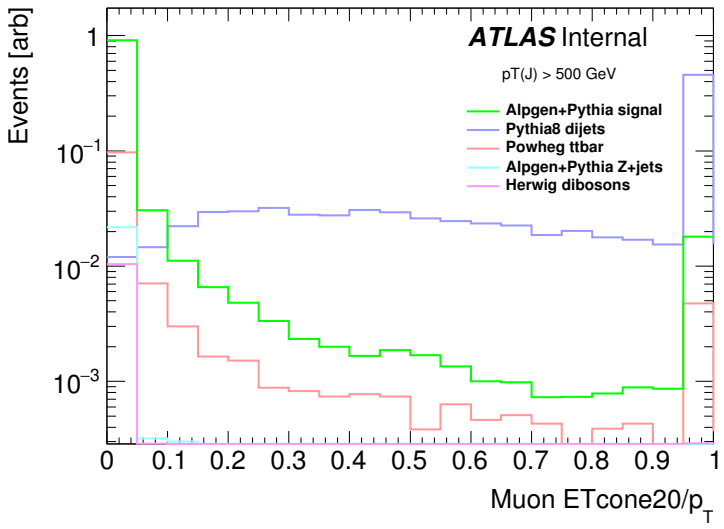

Figure 5.6: Predicted distributions from MC simulation of calorimeter isolation energy for the signal and background processes. Calorimeter isolation energy is defined as the scalar sum of the p_{T} in all calorimeter cells in a cone of radius $\Delta R = 0.2$ around the muon divided by the muon p_{T}. Here the baseline event selections are applied. The signal and total background are both normalized to unity. The rightmost histogram bin includes overflow values that are larger than the axis range of the plot.

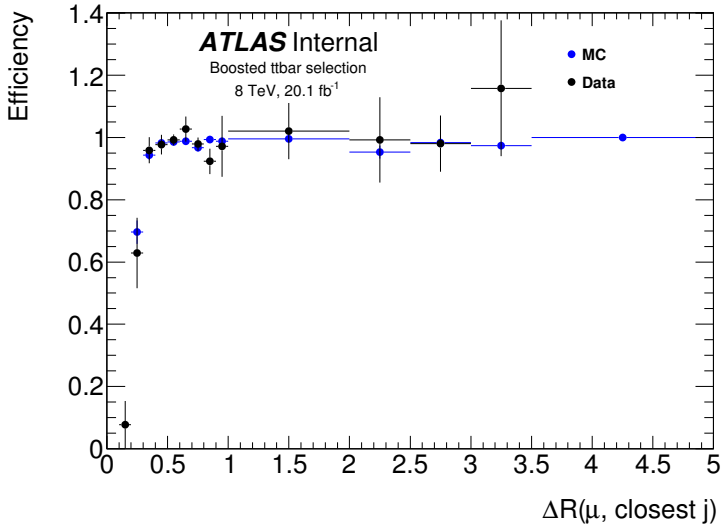

Figure 5.7: Efficiency of the muon isolation requirement measured in boosted $t\bar{t}$ events from MC simulation and from a high-purity data sample as a function of the distance between the muon and the closest jet. More details regarding this study of isolation efficiency are in Appendix A.1, along with the selection used.

5.4.3 Other Details

The signal final state contains a neutrino, which can not be directly detected as it is too weakly interacting. However, the neutrino can be indirectly detected by looking for missing transverse momentum since the total vector sum of transverse momentum must be conserved. Figure 7.4 shows the predicted distributions from MC simulation of missing transverse momentum for the signal and background processes. Applying a requirement on missing transverse momentum was studied, but it was found not to improve the signal selection or the background rejection.

Any additional jets with $p_{\mathrm{T}} > 100$ GeV are included in the analysis. The ΔR distance is always measured with respect to the closest jet, which is not necessarily the leading jet.

5.5 Estimation of Background

For the final state with at least one high-p_{T} jet and a single muon, the dominant background processes that contribute to the signal region are dijets, $t\bar{t}$ and Z + jets. In addition, there is a small background contribution from diboson production. These backgrounds are all modelled using the simulated MC samples described in Section 4.2.

Data from control regions are used to correct the the normalisation of the dijet, $t\bar{t}$ and Z + jets simulated MC samples to that observed in data. This reduces the reliance on MC simulation, which can be inaccurate. For example, detector simulation uncertainties and theoretical uncertainties such as on the parton distribution function and the factorisation and renormalisation scale can be very significant. This data-driven normalisation correction therefore lowers the uncertainty on the background estimation. The definitions of these control regions and the details of the normalisation correction procedure are given in the follow subsections. The distributions from data and from MC simulation, after the normalisation, of the angular seperation between the muon and the closest jet in the control regions are shown in Figures 5.8–5.10.

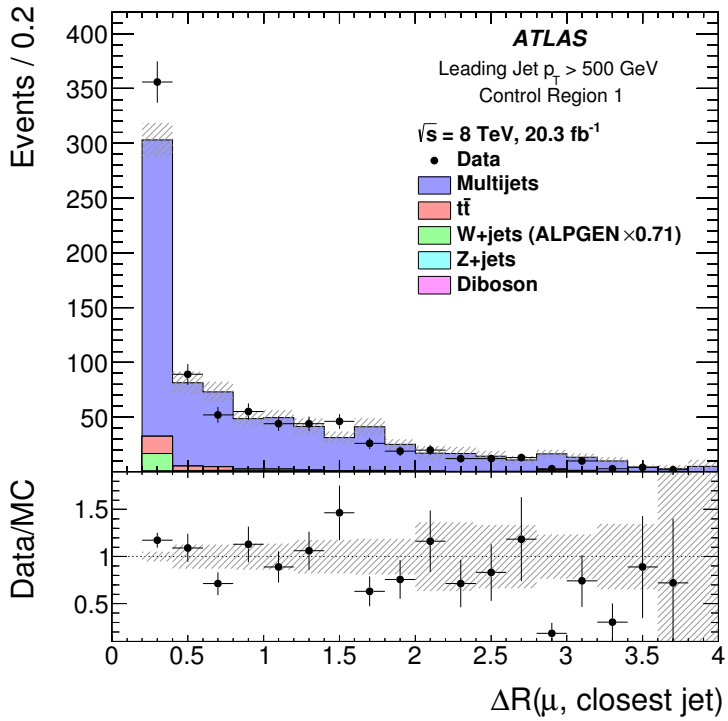

Figure 5.8: Distributions from data and from MC simulation of the angular separation between the muon and the closest jet in Control Region 1. The lower panel shows the ratio of data to MC simulation distribution. The error bars correspond to the statistical uncertainty and the shaded error bands correspond to the systematic uncertainties. The dijet, $t\bar{t}$ and Z + jets backgrounds have been scaled according to their respective control regions. The W + jets signal has been scaled by 0.71.

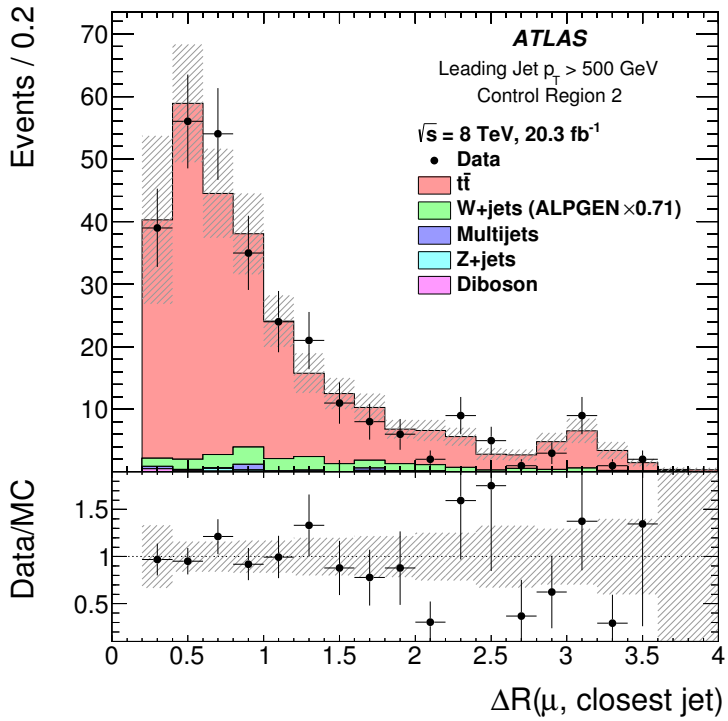

Figure 5.9: Distributions from data and from MC simulation of the angular separation between the muon and the closest jet in Control Region 2. The lower panel shows the ratio of data to MC simulation distribution. The error bars correspond to the statistical uncertainty and the shaded error bands correspond to the systematic uncertainties. The dijet, $t\bar{t}$ and Z + jets backgrounds have been scaled according to their respective control regions. The W + jets signal has been scaled by 0.71.

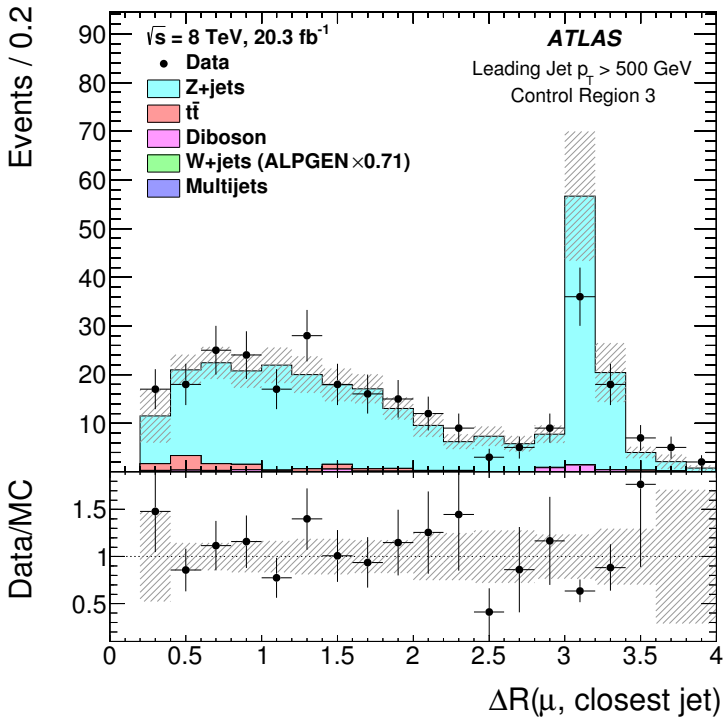

Figure 5.10: Distributions from data and from MC simulation of the angular separation between the muon and the closest jet in Control Region 3. The lower panel shows the ratio of data to MC simulation distribution. The error bars correspond to the statistical uncertainty and the shaded error bands correspond to the systematic uncertainties. The dijet, $t\bar{t}$ and Z + jets backgrounds have been scaled according to their respective control regions. The W + jets signal has been scaled by 0.71.

5.5.1 Control Region Definitions

For each of the three main background processes—dijets, $t\bar{t}$ and Z + jets—a control region utilising an event selection orthogonal to that used to define the signal region is defined such that most of the events in this control region are from the chosen background.

Control Region 1 (CR1) is enriched in dijets, with 93% of events originating from dijet production, by applying the inverse of the signal region isolation selection: the muon must fail either the track-based isolation or the calorimeter-based isolation criteria of Section 5.4.2. It only uses events that pass the second muon trigger of Section 5.2.2, which does not have an isolation requirement. The first muon trigger has an isolation requirement which would bias the selection. As a result, it also requires the muons to have $p_{\mathrm{T}} > 38$ GeV, as events with lower muon p_{T} are mostly rejected by the trigger used. The distance between the muon and the closest jet must satisfy $\Delta R > 0.2$ so that it more closely matches the signal region.

Control Region 2 (CR2) is enriched in $t\bar{t}$, with 91% of events originating from $t\bar{t}$ production, by requiring at least two b-tagged jets.

Control Region 3 (CR3) is enriched in Z + jets, with 94% of events originating from Z + jets production, by using events with exactly two muons, with both muons passing the signal region isolation criteria of Section 5.4.2. It also requires that the dimuon invariant mass satisfies 60 GeV $< m_{\mu\mu} <$ 120 GeV. This mass window is approximately centered around the mass of the Z boson, $m_Z = 91$ GeV. In this case, the muon with the higher p_{T} of the two is chosen during the calculation of ΔR.

The number of events observed in data in each control region and the expected composition of these events are shown in Tables 5.2–5.4. Although the purity of these control regions could be improved with a more stringent selection, this would reduce the number of data events that are in these control regions. With a smaller event sample, the statistical uncertainty in the data-driven normalisation correction would be larger. The above selection has been carefully chosen such that the purity is as high as possible while keeping the statistical

Control Region 1			
Process	$0.2 < \Delta R < 2.4$	$\Delta R > 2.4$	Inclusive
Dijets	93%	94%	93%
$t\bar{t}$	4%	3%	4%
Z + jets	0%	0%	0%
Dibosons	0%	0%	0%
W + jets	3%	4%	3%
Events in Data	763	47	810

Table 5.2: The number of events in Control Region 1 (CR1) (defined in Section 5.5.1) observed in data, along with the composition of these events as predicted by MC simulation, split by the angular seperation between the muon and the closest jet. The dijet, $t\bar{t}$ and Z + jets backgrounds have been scaled according to their respective control regions. The W + jets signal has been scaled by 0.71.

uncertainty in the correction around 5%.

5.5.2 Iterative Scaling

If the control regions were perfect and contained nothing but the chosen background, then a scale factor for that background SF_i could be calculated as

$$\mathrm{SF}_i = \frac{N^{\mathrm{data}}_{\mathrm{CR}i}}{N^{\mathrm{MC\text{-}}i}_{\mathrm{CR}i}},$$

where $N^{\mathrm{data}}_{\mathrm{CR}i}$ is the number of events in data and $N^{\mathrm{MC\text{-}}i}_{\mathrm{CR}i}$ is the number of events from the simulated MC sample for the chosen background in the appropriate control region. This can then be used to scale the simulated MC sample for that background to correct its normalisation to that observed in data.

Unfortunately, the control regions are not perfect and there is some small contamination from other backgrounds and the W + jets signal. Therefore it is necessary to subtract off this contamination before calculating the scale factor as the ratio of data and MC simulation. The best estimates for the contamination are the scaled simulated MC samples, and so the

Control Region 2			
Process	$0.2 < \Delta R < 2.4$	$\Delta R > 2.4$	Inclusive
Dijets	1%	1%	1%
$t\bar{t}$	92%	89%	92%
Z + jets	0%	0%	0%
Dibosons	1%	0%	0%
W + jets	7%	10%	7%
Events in Data	265	22	287

Table 5.3: The number of events in the Control Region 2 (CR2) (defined in Section 5.5.1) observed in data, along with the composition of these events as predicted by MC simulation, split by the angular seperation between the muon and the closest jet. The dijet, $t\bar{t}$ and Z + jets backgrounds have been scaled according to their respective control regions. The W + jets signal has been scaled by 0.71.

Control Region 3			
Process	$0.2 < \Delta R < 2.4$	$\Delta R > 2.4$	Inclusive
Dijets	0%	0%	0%
$t\bar{t}$	6%	1%	4%
Z + jets	93%	97%	94%
Dibosons	2%	3%	2%
W + jets	0%	0%	0%
Events in Data	199	87	286

Table 5.4: The number of events in Control Region 3 (CR3) (defined in Section 5.5.1) observed in observed in data, along with the composition of these events as predicted by MC simulation, split by the angular seperation between the muon and the closest jet. The dijet, $t\bar{t}$ and Z + jets backgrounds have been scaled according to their respective control regions. The W + jets signal has been scaled by 0.71.

Iteration Number	Dijets	$t\bar{t}$	Z + jets	W + jets
1	1.110 ± 0.053	0.834 ± 0.061	0.701 ± 0.051	0.714
2	1.136 ± 0.054	0.861 ± 0.061	0.706 ± 0.052	0.711
3	1.134 ± 0.054	0.861 ± 0.061	0.705 ± 0.052	0.711

Table 5.5: Scale factors for correcting the normalisation of the simulated MC samples for dijets, $t\bar{t}$, Z+jets and W + jets at each iteration of the data-driven scaling procedure. Uncertainties given on the scale factors for the background samples are statistical uncertainties due to the number of events in data and in the simulated MC sample.

scale factor is calculated as:

$$\mathrm{SF}_i = \frac{N_{\mathrm{CR}i}^{\mathrm{data}} - \sum_{i \neq j} N_{\mathrm{CR}i}^{\mathrm{MC}\text{-}j} \mathrm{SF}_j}{N_{\mathrm{CR}i}^{\mathrm{MC}\text{-}i}}.$$

The scaling procedure is also extended to the W + jets signal using data from the signal region, so that contamination from the W + jets signal can be estimated as well.

However, in this procedure there is a circular dependency: the scale factors are used in the calculation of the scale factors themselves. To address this, an iterative approach is applied. First, the scale factors are derived with the contamination subtracted using the uncorrected normalisations. Then the normalisations are updated with the scale factor corrections and the procedure to derive the scale factors is repeated. Since the contamination in each of the regions is quite small, the scale factors converge very rapidly. Table 5.5 shows the scale factors at each iteration of this procedure, and the scale factors converged to within their statistical uncertainties after just three iterations.

As a result of this procedure, the dijet sample is scaled by 1.134 ± 0.054, the $t\bar{t}$ sample is scaled by 0.861 ± 0.061, the Z + jets sample is scaled by 0.705 ± 0.052 and the W + jets sample is scaled by 0.711 ± 0.016. These uncertainties in the scale factors are statistical uncertainties due to the number of events in data and in the simulated MC samples.

5.5.3 Validation of Background Modelling

In order to validate the modelling of main background processes—dijets, $t\bar{t}$ and Z + jets—by the simulated MC samples, data from the three control regions are compared to the predictions from the MC samples.

The distributions of transverse momentum, pseudorapidity and azimuthal angle of the reconstructed physics objects can shed light on potential mismodelling in both the physical event generation and the detector simulation of these events. These distributions for the muon are shown in Figures 5.11–5.13 and for the closest jet to the muon in Figures 5.14–5.16. Reasonably good agreement between the data and the MC predictions to within the uncertainties is seen in all of these distributions.

The missing transverse momentum and the transverse mass of the reconstructed W boson candidate are often used in studies of leptonic W bosons, as these events are expected to have large missing transverse momentum and the transverse mass m_T has a Jacobian peak at $m_T \approx m_W$ [112]. The transverse mass is defined as

$$m_T = \sqrt{2p_{\mathrm{T}}^{\mu} E_{\mathrm{T}}^{\mathrm{miss}} (1 - \cos\Delta\phi)},$$

where p_{T}^{μ} is the transverse momentum of the muon, $E_{\mathrm{T}}^{\mathrm{miss}}$ is the missing transverse momentum and $\Delta\phi$ is the azimuthal angle between the muon and the missing transverse momentum. These distributions are shown in Figures 5.17 and 5.18. Again good agreement is seen, except for the missing transverse momentum in Control Region 1. Since none of the event selections apply requirements on the missing transverse momentum, this disagreement is not a cause for concern.

In addition to the angular separation between the muon and the closest jet, the polar decay angle and the azimuthal decay angle in the rest frame of the jet + W system are also sensitive to collinear W production. These angles are measured with respect to the

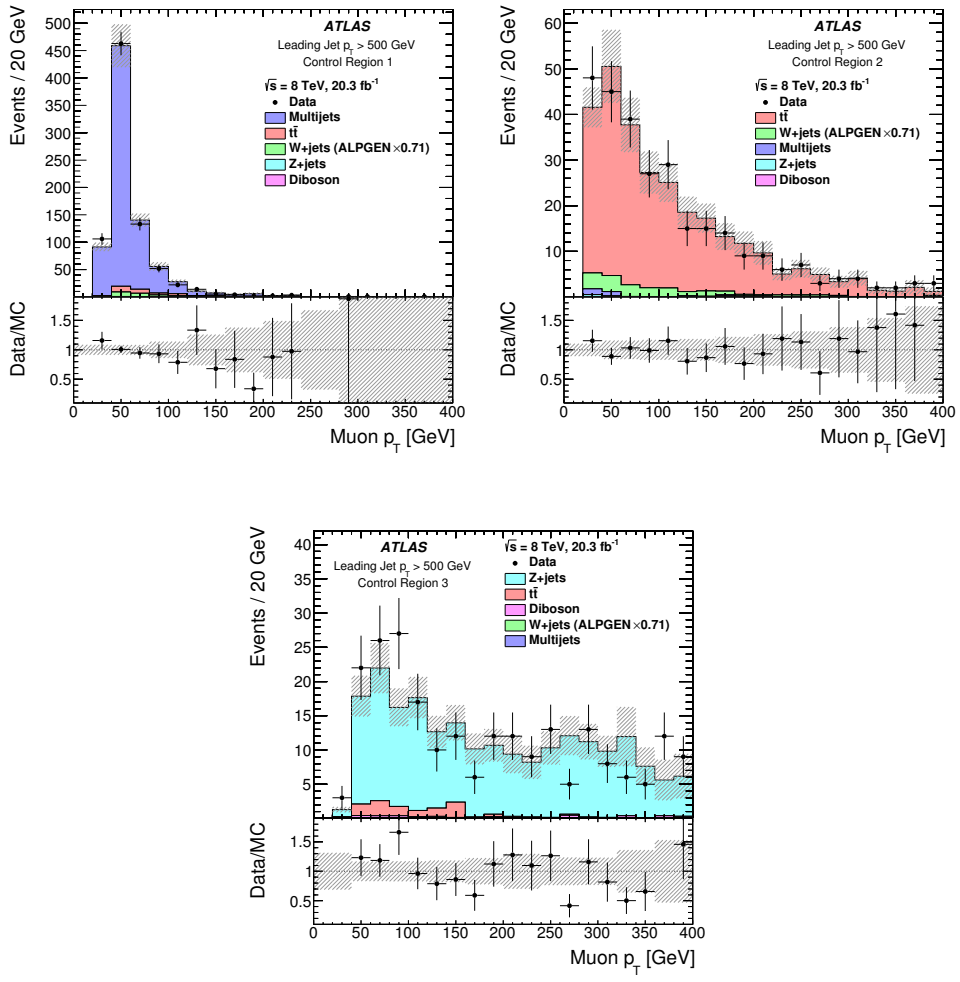

Figure 5.11: Distributions from data and from MC simulation of the muon p_{T} in Control Region 1 (upper left), Control Region 2 (upper right) and Control Region 3 (lower). The lower panel shows the ratio of data to MC simulation distribution. The error bars correspond to the statistical uncertainty and the shaded error bands correspond to the systematic uncertainties. The dijet, $t\bar{t}$ and Z + jets backgrounds have been scaled according to their respective control regions. The W + jets signal has been scaled by 0.71.

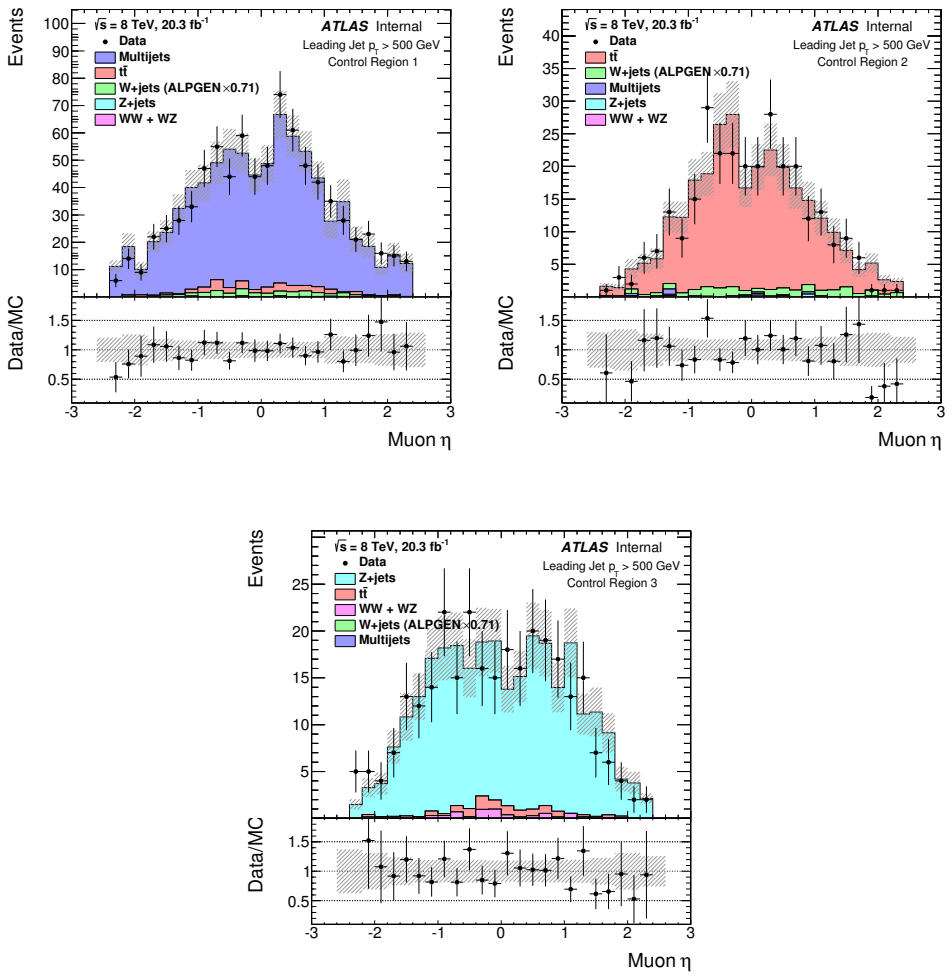

Figure 5.12: Distributions from data and from MC simulation of the muon η in Control Region 1 (upper left), Control Region 2 (upper right) and Control Region 3 (lower). The lower panel shows the ratio of data to MC simulation distribution. The error bars correspond to the statistical uncertainty and the shaded error bands correspond to the systematic uncertainties. The dijet, $t\bar{t}$ and Z + jets backgrounds have been scaled according to their respective control regions. The W + jets signal has been scaled by 0.71.

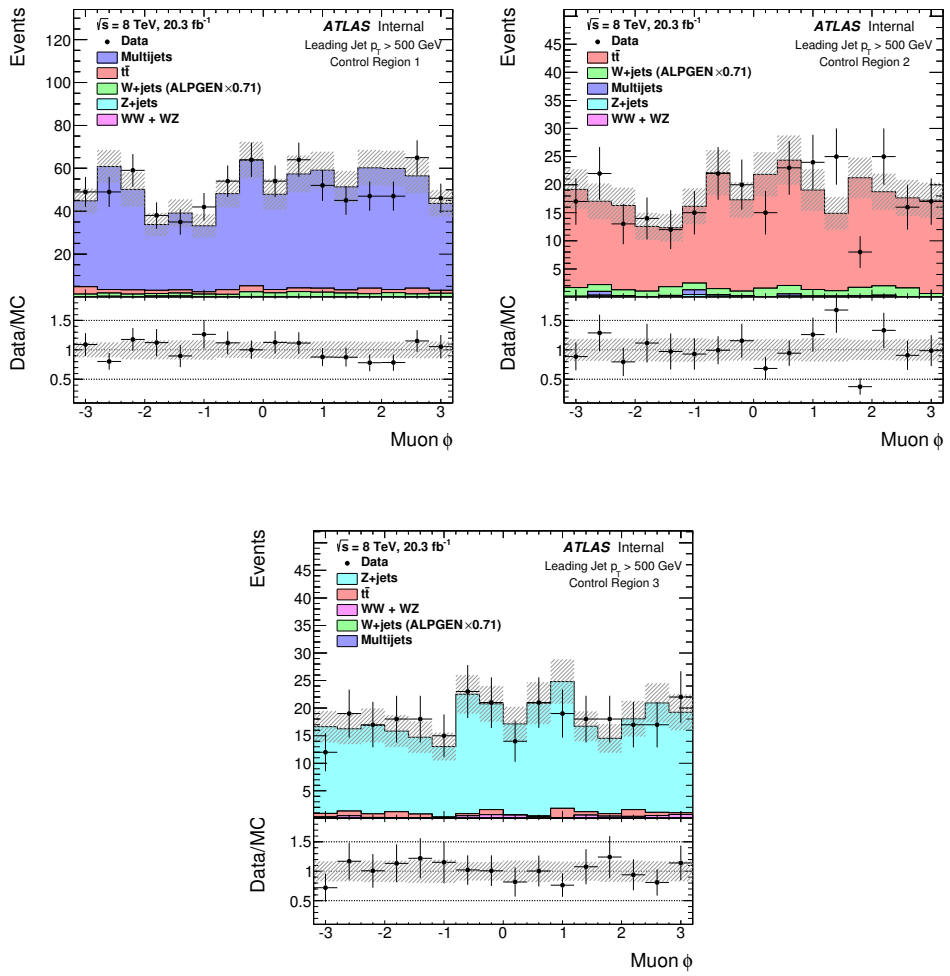

Figure 5.13: Distributions from data and from MC simulation of the muon ϕ in Control Region 1 (upper left), Control Region 2 (upper right) and Control Region 3 (lower). The lower panel shows the ratio of data to MC simulation distribution. The error bars correspond to the statistical uncertainty and the shaded error bands correspond to the systematic uncertainties. The dijet, $t\bar{t}$ and Z + jets backgrounds have been scaled according to their respective control regions. The W + jets signal has been scaled by 0.71.

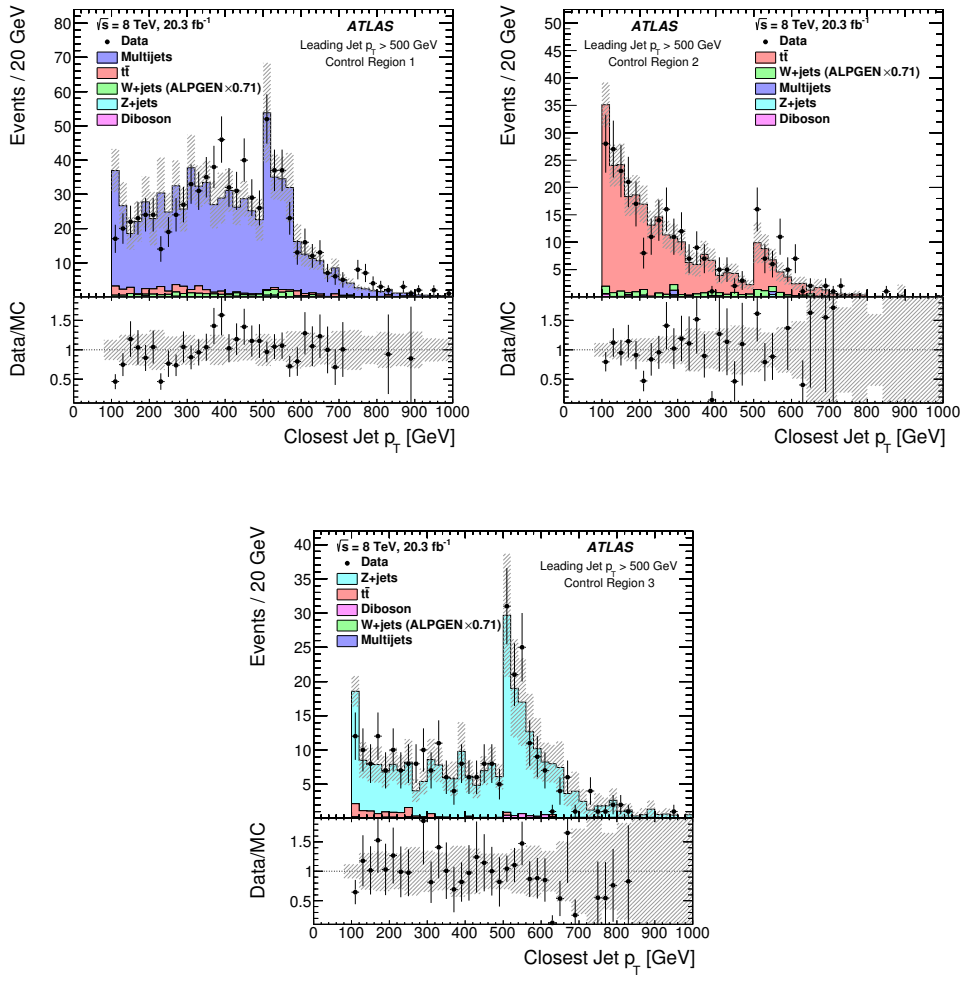

Figure 5.14: Distributions from data and from MC simulation of the p_{T} of the jet closest to the muon in Control Region 1 (upper left), Control Region 2 (upper right) and Control Region 3 (lower). The lower panel shows the ratio of data to MC simulation distribution. The error bars correspond to the statistical uncertainty and the shaded error bands correspond to the systematic uncertainties. The dijet, $t\bar{t}$ and Z + jets backgrounds have been scaled according to their respective control regions. The W + jets signal has been scaled by 0.71.

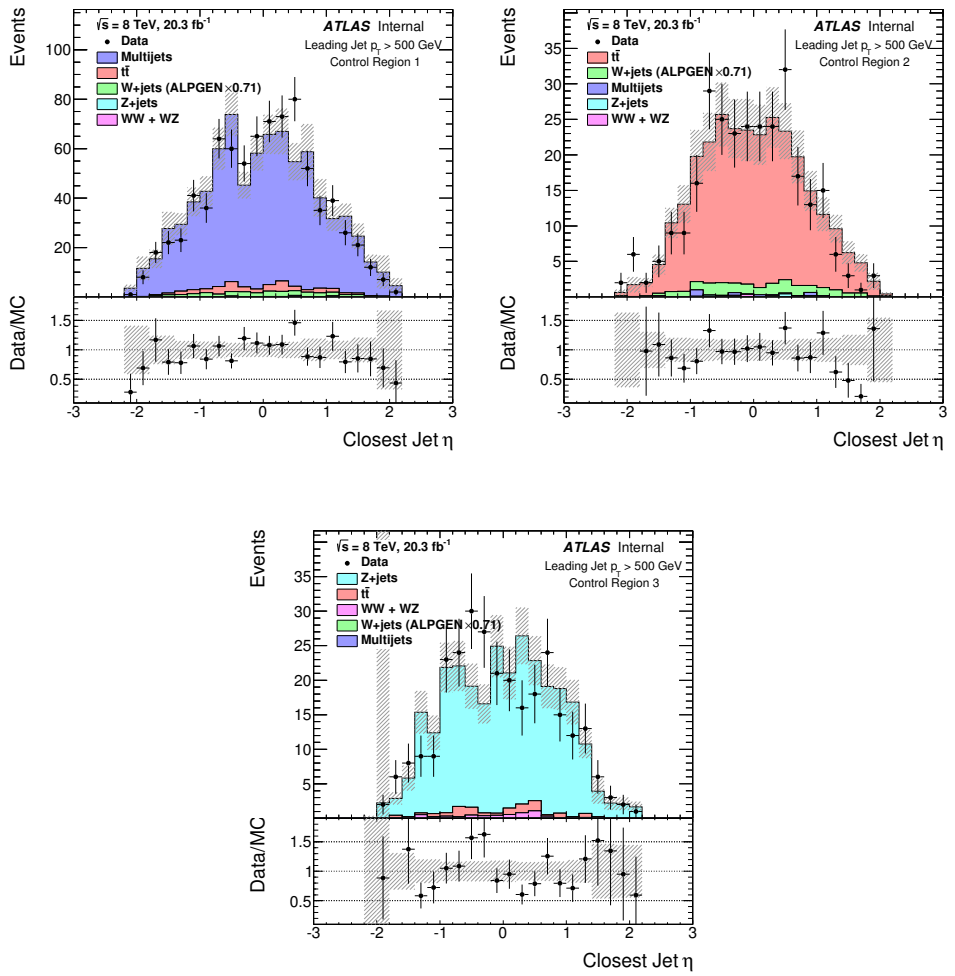

Figure 5.15: Distributions from data and from MC simulation of the η of the jet closest to the muon in Control Region 1 (upper left), Control Region 2 (upper right) and Control Region 3 (lower). The lower panel shows the ratio of data to MC simulation distribution. The error bars correspond to the statistical uncertainty and the shaded error bands correspond to the systematic uncertainties. The dijet, $t\bar{t}$ and Z + jets backgrounds have been scaled according to their respective control regions. The W + jets signal has been scaled by 0.71.

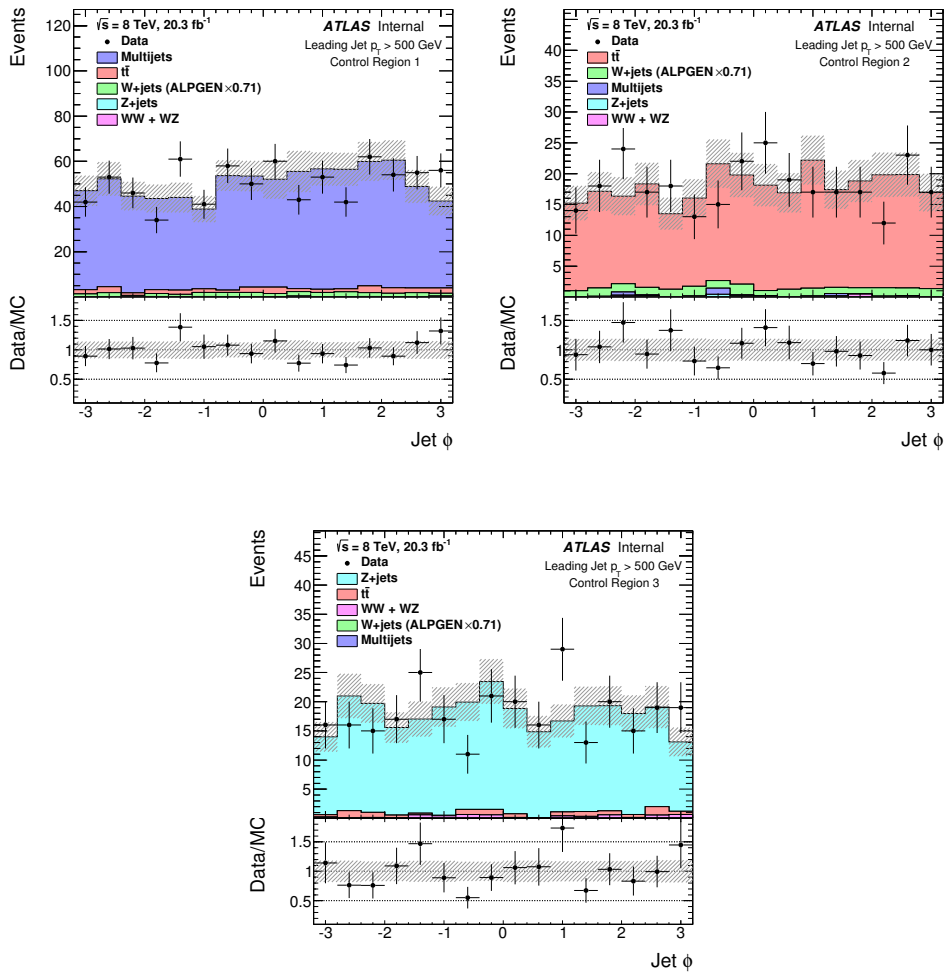

Figure 5.16: Distributions from data and from MC simulation of the ϕ of the jet closest to the muon in Control Region 1 (upper left), Control Region 2 (upper right) and Control Region 3 (lower). The lower panel shows the ratio of data to MC simulation distribution. The error bars correspond to the statistical uncertainty and the shaded error bands correspond to the systematic uncertainties. The dijet, $t\bar{t}$ and Z + jets backgrounds have been scaled according to their respective control regions. The W + jets signal has been scaled by 0.71.

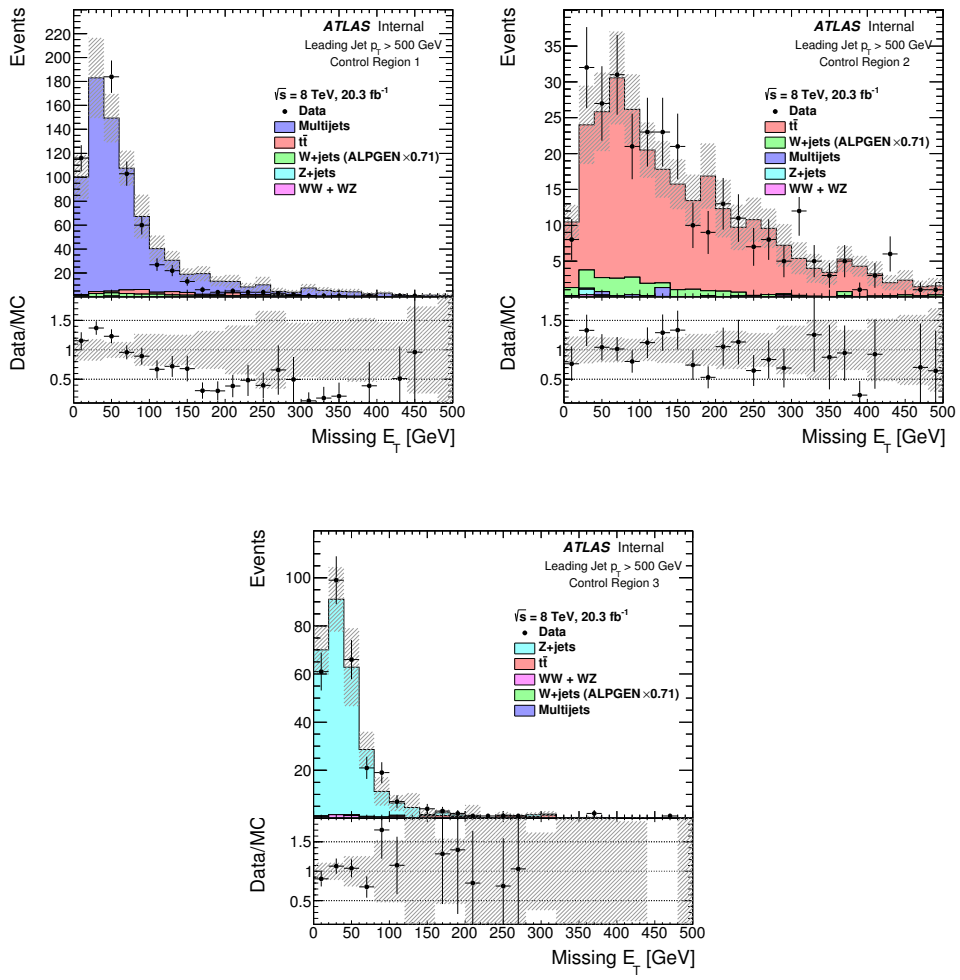

Figure 5.17: Distributions from data and from MC simulation of $E_{\mathrm{T}}^{\mathrm{miss}}$ in Control Region 1 (upper left), Control Region 2 (upper right) and Control Region 3 (lower). The lower panel shows the ratio of data to MC simulation distribution. The error bars correspond to the statistical uncertainty and the shaded error bands correspond to the systematic uncertainties. The dijet, $t\bar{t}$ and Z + jets backgrounds have been scaled according to their respective control regions. The W + jets signal has been scaled by 0.71.

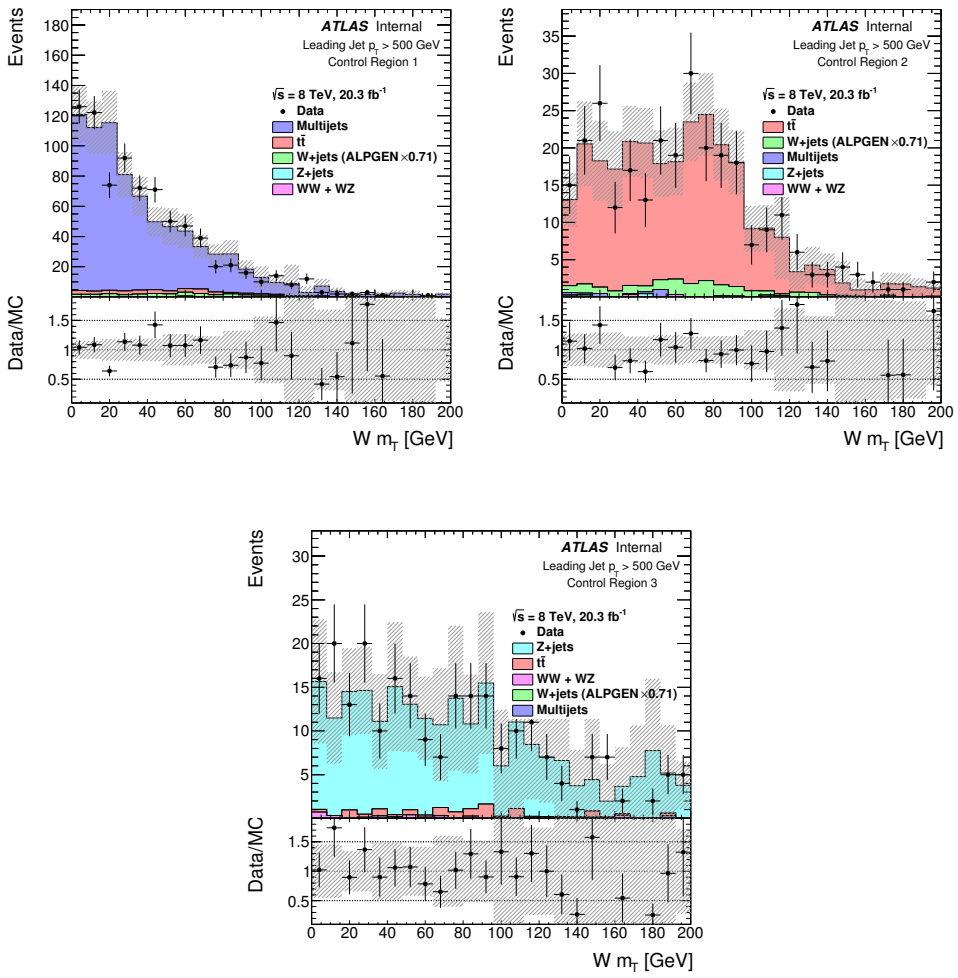

Figure 5.18: Distributions from data and from MC simulation of m_T in Control Region 1 (upper left), Control Region 2 (upper right) and Control Region 3 (lower). The lower panel shows the ratio of data to MC simulation distribution. The error bars correspond to the statistical uncertainty and the shaded error bands correspond to the systematic uncertainties. The dijet, $t\bar{t}$ and Z + jets backgrounds have been scaled according to their respective control regions. The W + jets signal has been scaled by 0.71.

vector connecting the lab frame to the rest frame of the jet + W system. To reconstruct the rest frame of the jet + W system, the missing transverse momentum is used as a proxy for W boson decay's neutrino. Since the missing transverse momentum does not provide any information on the neutrino's momentum in the z direction, an arbitary choice for this is made so that the neutrino has the same rapidity as the jet + muon rapidity. This has the advantage that the two decay angles are invariant under longitudinal boosts. These distributions are shown in Figures 5.19 and 5.20, where good agreement is seen.

Although the charge of the W boson is not expected to be symmetric at the LHC, the three main background processes are expected to be symmetric with respect to the charge of the muon. In the case of $t\bar{t}$ and Z + jets, this is because the top quark and the Z boson are neutrally charged. In the case of dijets, although the charge distribution of the quark partons may not be symmetric and the charge of the hadronization products must sum to the quark charge, the assymmetry is essentially smeared out by the huge numbers of postively and negatively charged hadrons. Figures 5.21 and 5.22 show the distribution of angular separation between the muon and the closest jet, just like Figures 5.8–5.10, but split by the charge of the muon. Again good agreement is seen and, as expected, the charge of the muon from the main background processes is mostly symmetric.

5.6 Summary of Signal and Control Region Definitions

A summary of the most pertinent event selection critera for the signal region and the three control regions is provided in Table 5.6.

5.7 Fiducial Definition

While the detector-level selection used for the analysis has been described earlier, this is not the fiducial definition of the phase space in which the measurement is made. The fiducial

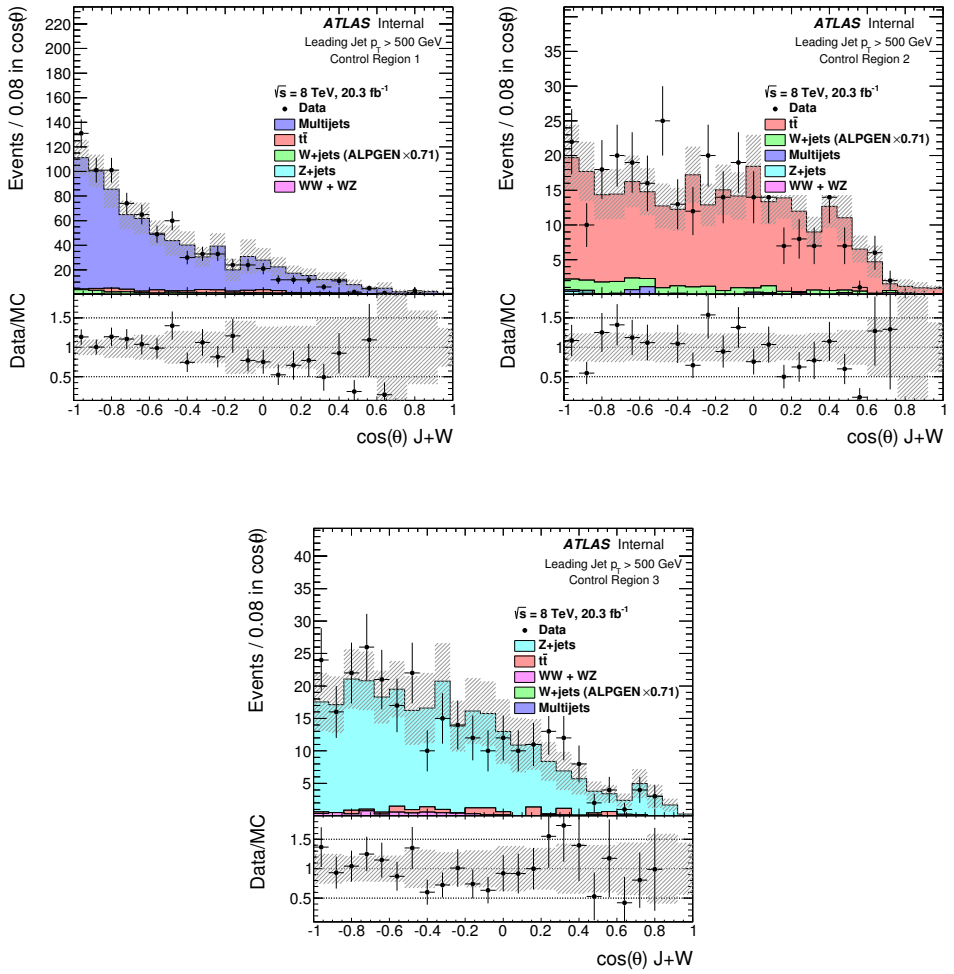

Figure 5.19: Distributions from data and from MC simulation of the cosine of the polar decay angle in the rest frame of the jet + W system in Control Region 1 (upper left), Control Region 2 (upper right) and Control Region 3 (lower). The angle is measured with respect to the vector connecting the lab frame to the rest frame of the jet + W system. The lower panel shows the ratio of data to MC simulation distribution. The error bars correspond to the statistical uncertainty and the shaded error bands correspond to the systematic uncertainties. The dijet, $t\bar{t}$ and Z + jets backgrounds have been scaled according to their respective control regions. The W + jets signal has been scaled by 0.71.

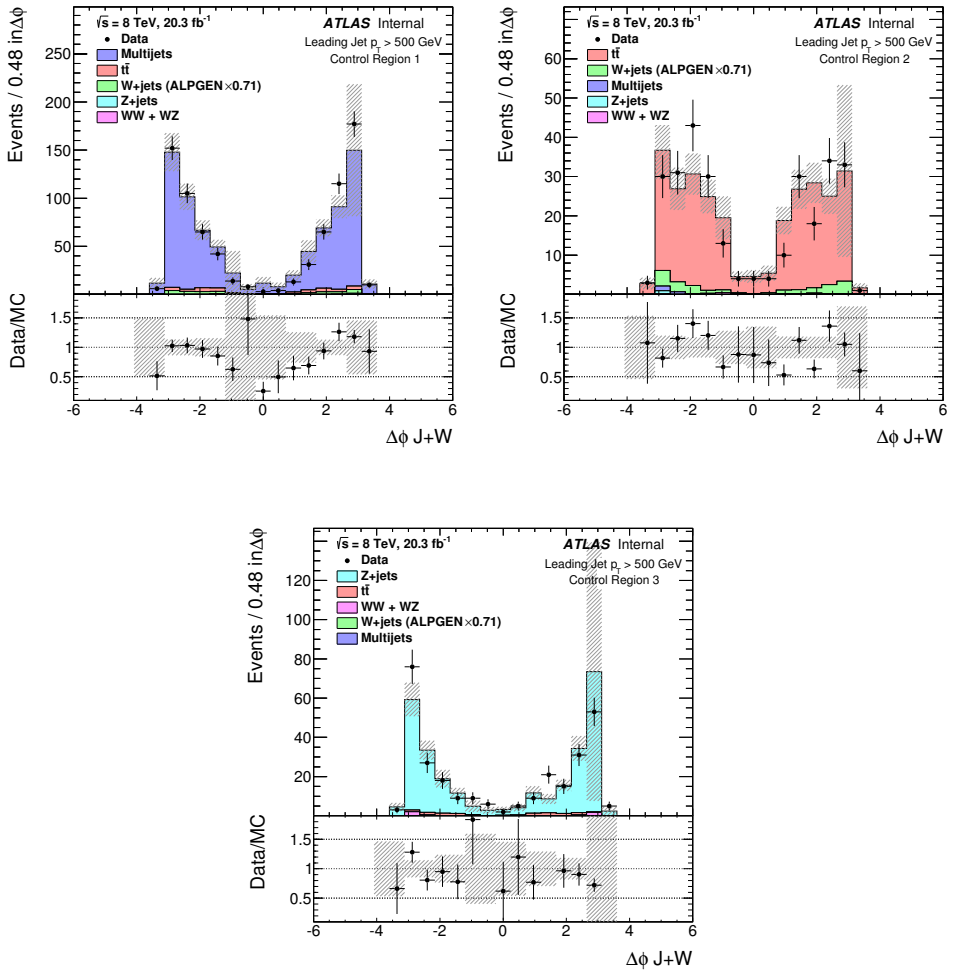

Figure 5.20: Distributions from data and from MC simulation of the azimuthal decay angle in the rest frame of the jet + W system in Control Region 1 (upper left), Control Region 2 (upper right) and Control Region 3 (lower). The angle is measured with respect to the vector connecting the lab frame to the rest frame of the jet + W system. The lower panel shows the ratio of data to MC simulation distribution. The error bars correspond to the statistical uncertainty and the shaded error bands correspond to the systematic uncertainties. The dijet, $t\bar{t}$ and Z + jets backgrounds have been scaled according to their respective control regions. The W + jets signal has been scaled by 0.71.

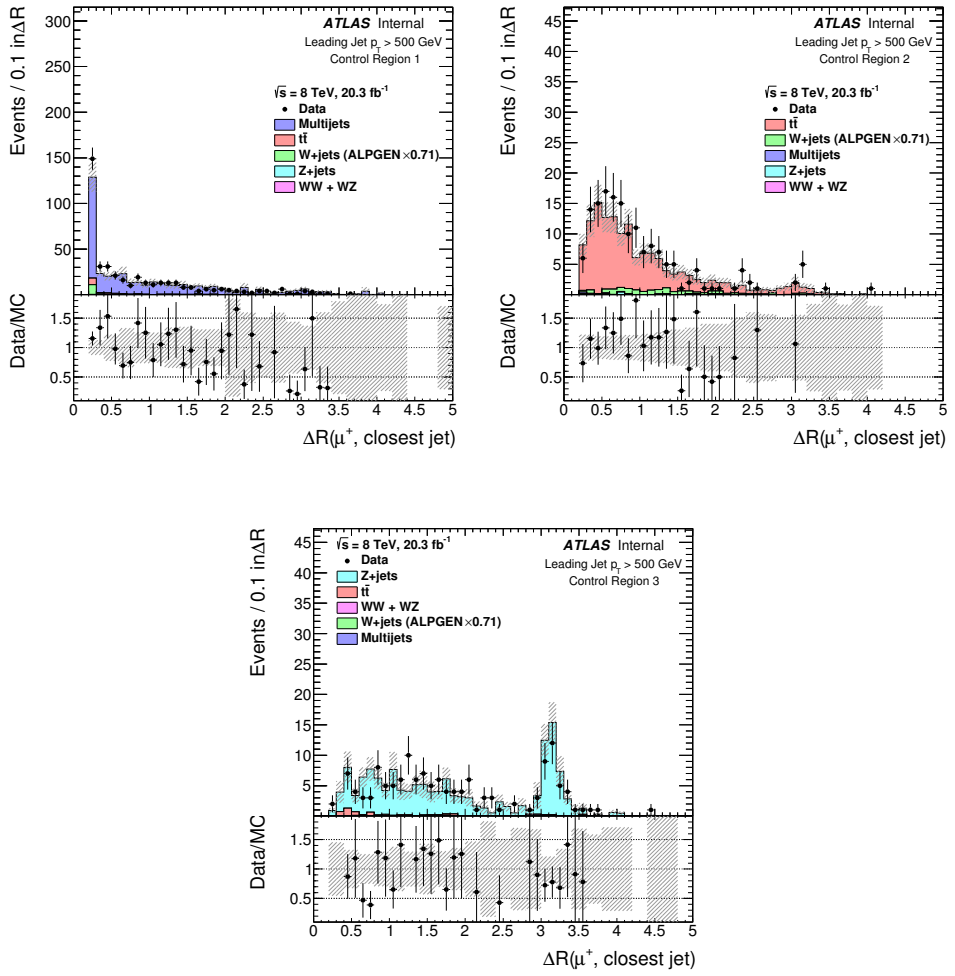

Figure 5.21: Distributions from data and from MC simulation of the angular separation between the muon and the closest jet for events with a postively charged muon in Control Region 1 (upper left), Control Region 2 (upper right) and Control Region 3 (lower). The lower panel shows the ratio of data to MC simulation distribution. The error bars correspond to the statistical uncertainty and the shaded error bands correspond to the systematic uncertainties. The dijet, $t\bar{t}$ and Z + jets backgrounds have been scaled according to their respective control regions. The W + jets signal has been scaled by 0.71.

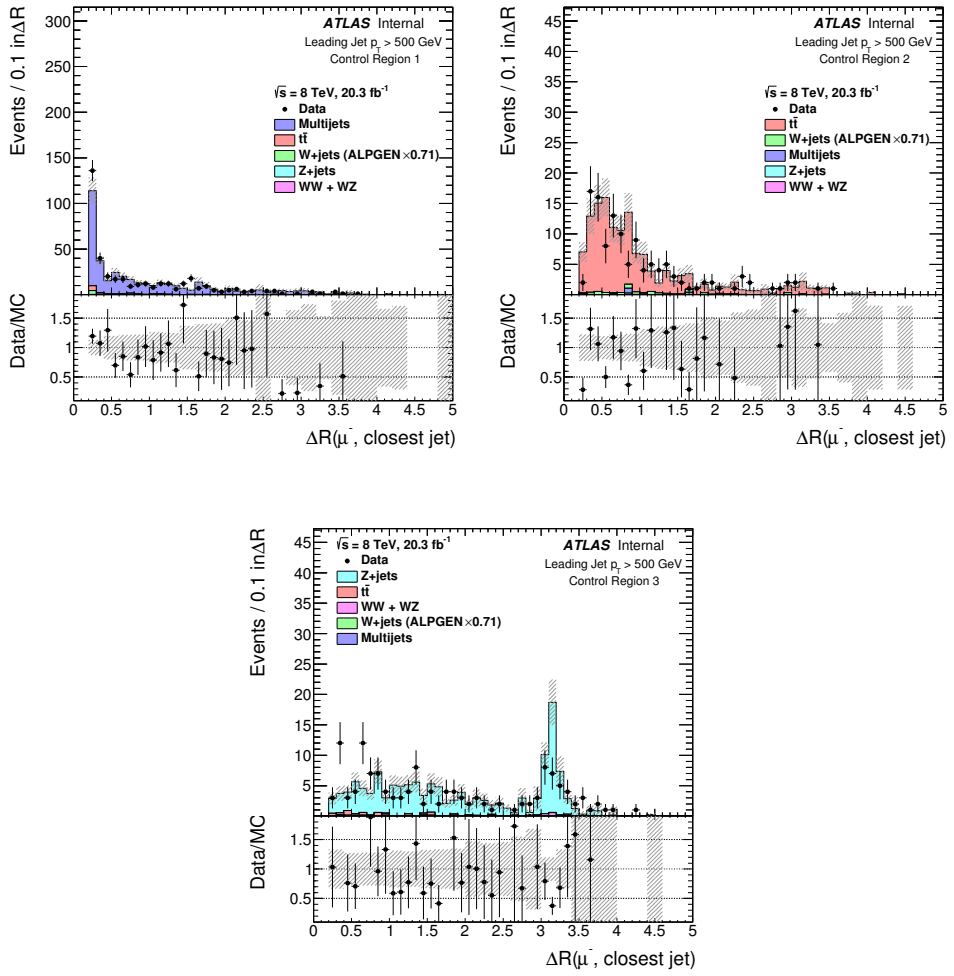

Figure 5.22: Distributions from data and from MC simulation of the angular separation between the muon and the closest jet for events with a negatively charged muon in Control Region 1 (upper left), Control Region 2 (upper right) and Control Region 3 (lower). The lower panel shows the ratio of data to MC simulation distribution. The error bars correspond to the statistical uncertainty and the shaded error bands correspond to the systematic uncertainties. The dijet, $t\bar{t}$ and Z + jets backgrounds have been scaled according to their respective control regions. The W + jets signal has been scaled by 0.71.

	$p_T^{\text{leading jet}}$	N_μ	Muon Isolation	$N_{b\text{-tags}}$	Other
SR	> 500 GeV	1	Yes	0	
CR1	> 500 GeV	1	Inverted	Any	Non-isolated muon trigger, $p_T^\mu > 38$ GeV
CR2	> 500 GeV	1	Yes	≥ 2	
CR3	> 500 GeV	2	Yes	Any	60 GeV $< m_{\mu\mu} <$ 120 GeV

Table 5.6: A summary of the most pertinent event selection critera for the signal region and the three control regions.

selection is similar to the detector-level selection, but it is instead applied at the particle-level. This allows the measurement results to be independent of the specific performance of the ATLAS detector, and thus easily comparable with theoretical calculations and future measurements from other experiments.

Particle-level jets are built using from stable final-state particles—these are defined as those with a proper lifetime τ corresponding to $c\tau < 10$ mm—excluding muons and neutrinos. These particle-level jets must satisfy $p_{\mathrm{T}} > 100$ GeV and $|\eta| < 2.1$.

The four-momentum vector of particle-level muons is corrected for the effects of final-state photon radiation (FSR) [113]. Photons that are contained in a cone of size $\Delta R = 0.1$ around the muon are summed and included as part of the muon energy. This procedure is known as dressing, and it allows the results to be compared with theoretical calculations that use a Born-level muon (this is where the muon does not have FSR). No requirements on promptness are applied to the muons or the dressing photons, which means they can originate from the decay of a hadron.

The fiducial selection requires that events have at least one particle-level jet with $p_{\mathrm{T}} > 500$ GeV and $|\eta| < 2.1$ and a particle-level muon with $p_{\mathrm{T}} > 25$ GeV and $|\eta| < 2.4$. Any additional muons that pass these requirements cause the event to be rejected. Events where the angular seperation between the muon and the closest jet $\Delta R < 0.2$ are also rejected. Unlike the detector-level analysis selection, there are no requirements on b-jets or electrons.

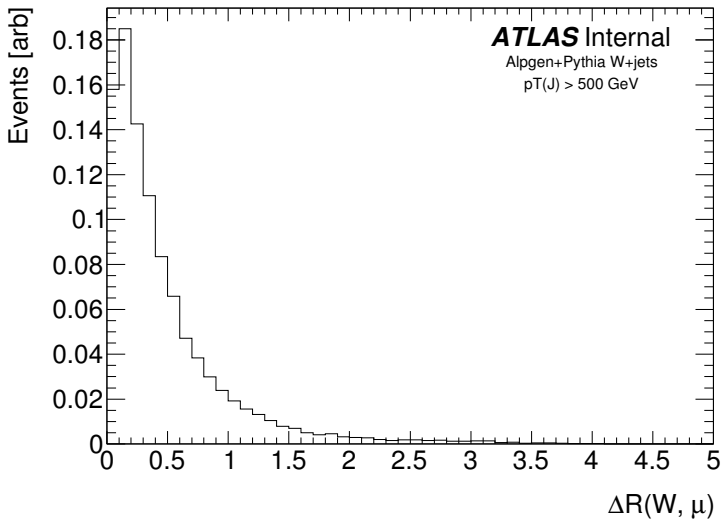

Figure 5.23: Predicted distribution of the angular separation between the muon and the W boson in W + jets events.

In some cases, it can be desirable to have the fiducial selection contain a promptness requirement. Adding this requirement causes the differential cross-section to increase by up to 3%, as events on average have fewer muons and therefore fewer events are rejected due to additional muons. A multiplicative correction factor, defined as $\sigma_{\text{prompt}}/\sigma$, is given for each bin of the measurement, so that the result is provided both with and without the promptness requirement.

Ideally, the angular separation between the W boson and the closest jet would be measured, since this is the angular separation that determines the collinear enhancement of W emission. However, the W boson cannot be fully reconstructed, as the neutrino is not directly detected. Instead, the angular separation between the muon and the closest jet, $\Delta R(\mu, \text{jet}) = \sqrt{(\Delta\phi)^2 + (\Delta\eta)^2}$, often referred to as just ΔR, is measured. In these events, the W boson is Lorentz-boosted and so its decays products are highly collimated. As a result, the difference between the path of the muon and the path of the W boson, shown in Figure 5.23, is small, and the smearing of the angular separation that results from using the direction of the muon instead of the W boson, shown in Figure 5.24, is minor.

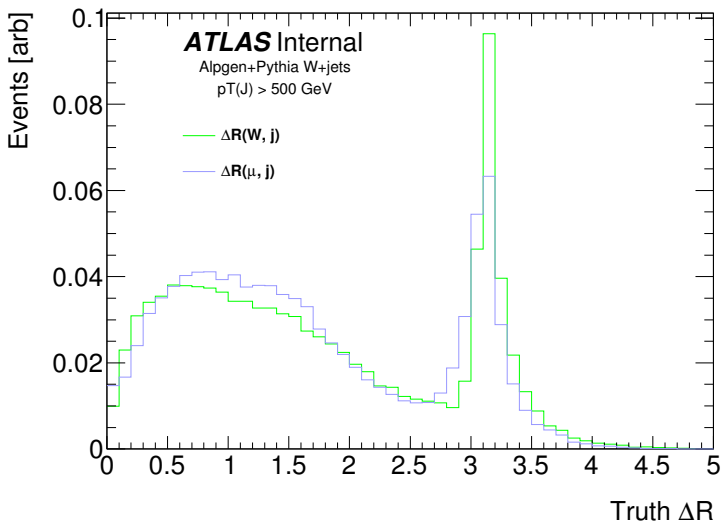

Figure 5.24: Predicted distributions of the angular separation between the W boson and the closest jet (green) and between the muon and the closest jet (blue) in W + jets events.

5.8 Correcting for Selection Efficiency and Detector Effects

While the angular seperation between the muon and the closest jet is measured in the signal region at detector-level and the estimate of background can be subtracted, there are still several confounding effects that need to be corrected for in order to obtain a measurement at particle-level with the fiducial definition of Section 5.7.

The dominant effect is the inefficiency of the signal region selection. An inefficiency occurs when a W + jets event passes the particle-level selection but fails the detector-level selection. While there are obvious sources of ineffeciency, such as in reconstructing the muon, in the muon trigger and in the b-tagging, there are more subtle sources as well. For example, the energy resolution of the detector can cause jets to have a lower p_{T} at detector-level than at particle-level. When a particle-level jet passes the $p_{\mathrm{T}}^{\text{leading jet}} > 500$ GeV requirement, the same jet at detector-level might not pass the same requirement, causing an inefficiency. The efficiency of the signal region selection as a function of the angular separation between the muon and the closest jet is evaluated using the W + jets MC simulation and shown in Figure 5.25.

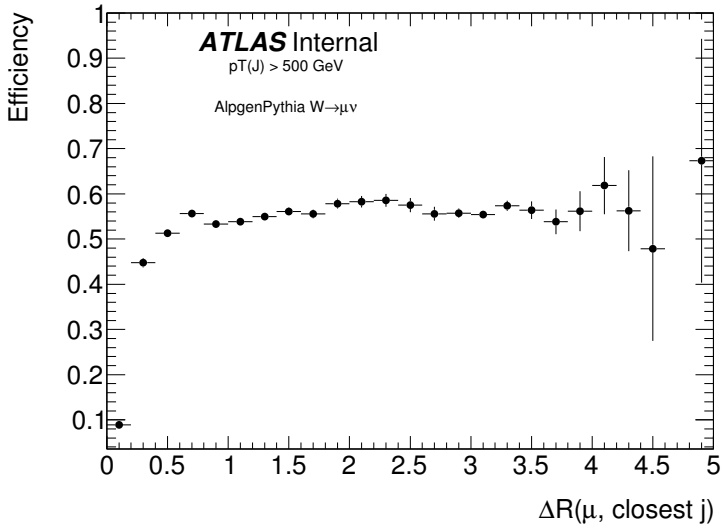

Figure 5.25: Efficiency of the detector-level signal region selection on W + jets events as a function of the angular separation between the muon and the closest jet. This is evaluated using the W + jets MC simulation. The error bars are statistical uncertainty.

Another effect is the presence of fakes. A fake occurs when a W + jets event fails the particle-level selection but passes the detector-level selection. Again this can happen due to effects like the finite resolution of the detector causing the detector-level jet to have higher p_{T} than the particle-level jet. Another source, however, is from $W \to \tau\nu$ events. When the τ-lepton decays into a muon, muon anti-neutrino and a tau neutrino, it is possible for these events to pass the detector-selection. These events are treated as not passing the particle-level selection, so as a result the contribution from $W \to \tau\nu$ is removed from the measurement and the cross-section results are quoted exclusively for the muon decay channel. The fraction of events that are fake as a function of the angular separation between the muon and the closest jet is evaluated using the W + jets MC simulation and shown in Figure 5.26. Approximately 5% of events are fakes from $W \to \tau\nu$ and 10% of events are fakes from $W \to \mu\nu$.

Lastly, there is a smearing effect on the angular seperation between the muon and the closest jet as a result of the detector's finite resolution. This means the measured angular separation at detector-level is not necessarily the same as the true angular separation at

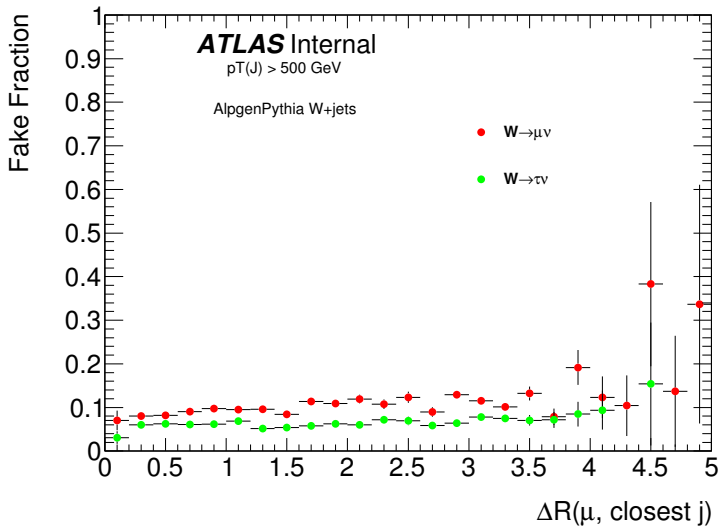

Figure 5.26: Fraction of W + jets events that pass the detector-level signal region selection but do not pass the fiducial particle-level selection, also known as fake events, as a function of the angular separation between the muon and the closest jet. Fakes from $W \to \mu\nu$ events (red) and fakes from $W \to \tau\nu$ events (green) are shown separately. This is evaluated using the W + jets MC simulation. The error bars are statistical uncertainty.

particle-level. The detector's response as a function of the angular separation between the muon and the closest jet is evaluated using the W + jets MC simulation and shown in Figure 5.27.

5.8.1 Iterative Bayesian Unfolding Approach

To correct for the effects of detector resolution, an iterative Bayesian unfolding approach is used [114, 115], implemented within the RooUnfold framework [116]. This approach starts with a single event that passes both the detector-level selection and the particle-level selection and examines the relationship between its location in the true (particle-level) bins T_i and its location in the observed (detector-level) bins O_i. In particular, one is interested in knowing the probability of this event to be in a specific true bin, given that it was in a specific

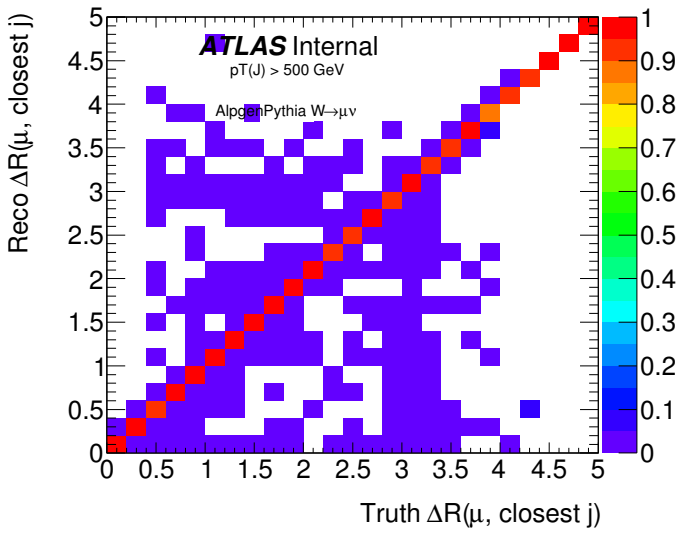

Figure 5.27: The detector response for the angular separation between the muon and the closest jet for W + jets events in the signal region. Each column, corresponding to a single particle-level bin, has been normalized to unity so it represents a probability distribution function. In the axes labels, 'reco' refers to detector-level and 'truth' refers to particle-level. This is evaluated using the W + jets MC simulation.

observed bin, $P(T_i \,|\, O_j)$. This can be calculated using Bayes' theorem:

$$P(T_i \,|\, O_j) = \frac{P(O_j \,|\, T_i)P(T_i)}{P(O_j)}.$$

Through the law of total probability, the denominator can be rewritten as follows:

$$P(T_i \,|\, O_j) = \frac{P(O_j \,|\, T_i)P(T_i)}{\sum_k P(O_j|T_k)P(T_k)}.$$

$P(O_j \,|\, T_i)$ can be calculated from MC simulation and is in fact the detector response r_{ij} shown in Figure 5.27. Thus,

$$P(T_i \,|\, O_j) = \frac{r_{ij}P(T_i)}{\sum_k r_{kj}P(T_k)}.$$

Here lies a problem: the true distribution $P(T_i)$ is not known and in fact this is what this analysis seeks to measure. An approximation is made here by assuming that $P(T_i) = p_i^{T(0)}$, where $p^{T(0)}$ is a prior estimate of the true particle-level distribution taken from W + jets MC. This leads to

$$P(T_i \,|\, O_j) = \frac{r_{ij} p_i^{T(0)}}{\sum_k r_{kj} p_k^{T(0)}}. \tag{5.1}$$

If the number of events observed in a given detector-level bin is $n(O_i)$, the number of W + jets events in this bin is fewer than this. This is because of the so-called fake events which pass the detector-level selection and not the particle-level selection. Accounting for this, the number of W + jets events observed in a bin is $n(O_i)(1 - f_i)$, where f_i is the fraction of fakes shown in Figure 5.26.

The expected contribution of a specific observed bin O_j to another specific true bin T_i can be calculated by multiplying the probability of this occuring for each observed event $P(T_i \,|\, O_j)$ with the number of W + jets events observed in that bin $n(O_i)(1-f_i)$. To calculate the expected total contribution to a specific true bin T_i, one can sum the individual expected contributions from each observed bin as follows:

$$\begin{aligned}
\mathbb{E}[n(T_i)] &= \sum_j P(T_i|O_j) n(O_j)(1 - f_j) \\
&= \sum_j \frac{r_{ij} p_i^{T(0)}}{\sum_k r_{kj} p_k^{T(0)}} n(O_j)(1 - f_j).
\end{aligned}$$

Finally, not every true W + jets event results in an observed event, as some are lost due to ineffeciency. The efficiencies ϵ_i from Figure 5.25 are used to correct for this, and the total

number of true W + jets events in each bin $N_{W+jets}(T_i)$ can be written as follows:

$$\begin{aligned} N_{W+jets}(T_i) &= \frac{1}{\epsilon_i}\mathbb{E}[n(T_i)] \\ &= \frac{1}{\epsilon_i}\sum_j \frac{r_{ij}p_i^{T(0)}}{\sum_k r_{kj}p_k^{T(0)}}.n(O_j)(1-f_j). \end{aligned}$$

With this procedure, an estimate of the particle-level distribution is made from the observed detector-level data. The earlier prior of assuming $P(T_i) = p_i^{T(0)}$, where this came from a MC sample, can now be updated with a new estimate $p_i^{T(1)} = \mathbb{E}[n(T_i)]$ and the process repeated.

5.8.2 Statistical Uncertainty

To assess the effect of statistical fluctuations of the data on the unfolded measurement, 100 psuedo-experiments are generated from the observed data using a MC toy approach. For each of these psuedo-experiments, each bin is drawn from a Poisson distribution with mean equal to the observed data and the estimated background subtracted. The resulting distributions are then unfolded. The average of these unfolded toys is taken as the nominal unfolded distribution and the bin-by-bin root-mean-squared spread of these is used as the statistical uncertainty due to the number of data events on each bin. Increasing the number of pseudo-experiments to 400 was tried, but this increase did not impact the results significantly and was computationally more expensive.

The simulated MC samples used for the background estimation and the simulated W + jets MC sample used for calculating efficiencies, fake rates and the detector response also have statistical uncertainties. These are assessed with the same procedure as above. The only difference is that for generating the pseudo-experiments Gaussian distributions are used instead of Poisson distributions. The variance on each Gaussian distribution is equal to the sum of the MC event weights squared $\sum_i w_i^2$.

Iterations	Uncertainty due to dependence on prior [%]	Total statistical uncertainty [%]
1	3.9	4.8
2	3.8	5.8
3	4.4	6.9
4	3.4	7.2

Table 5.7: Uncertainty on the total measured cross-section due to the bias of the unfolding and due to the size of the event sample as a function of the number of iterations used in the unfolding. Section 6.4 describes how the uncertainty due to the bias of the unfolding is estimated.

5.8.3 Number of Iterations

As the Bayesian unfolding uses a prior taken from the W + jets MC sample, there is some bias in the unfolded results. However, with more iterations, the bias can be reduced as there are more chances to update the prior with the new information of the observed data. Unfortunately, statistical fluctuations that are present in the observed data are also amplified with every iteration. As a result there needs to be a compromise that minimizes the combination of the statistical fluctuations and the bias due to the MC prior.

Up to four unfolding iterations were tried and, for each number of iterations, the uncertainty on the total measured cross-section due to the bias of the unfolding and due to the size of the event sample was evaluated, shown in Table 5.7. Section 6.4 describes how the uncertainty due to the bias of the unfolding is estimated. One unfolding iteration is used, as this was found to minimize the quadrature sum of these two uncertainties.

CHAPTER 6

SYSTEMATIC UNCERTAINTIES

Systematic uncertainty in the cross-section measurement arises from several independent uncertainty sources. These include uncertainties about the detector's performance, the uncertainty in the total integrated luminosity of the data sample, uncertainties in the background estimation and the uncertainty in the unfolding. The following sub-sections describe these uncertainty sources in more detail, and here an overview of how they are combined to form the total systematic uncertainty in the measurement is given.

For each systematic uncertainty, the selection criteria are re-applied, the data-driven scaling of the dijet, $t\bar{t}$ and Z + jets backgrounds are re-evaluated, and the unfolding procedure is repeated with the quantity under consideration varied by ± 1 standard deviation. This provides the $\pm 1\sigma$ effect of each uncertainty on the cross-section measurement. Strictly speaking this is an approximation, since the analysis is non-linear and can distort the probability distribution of the quantity under consideration when it is propogated through the analysis. Expressed algebraically, $\sigma\left(f(X)\right) \neq f\left(\mu(X) + \sigma(X)\right) - f\left(\mu(X)\right)$, where X is the quantity under consideration with nominal value $\mu(X)$ and uncertainty $\sigma(X)$, for any arbitary function f. To evaluate the effect more exactly, the bootstrap method can be used, where the analysis is re-ran many times with the quantity under consideration randomly sampled from its probability distribution, and, from this, the propogated probability distribution can be built. However, this is not done because it is very computationally intensive. For each systematic uncertainty, the bootstrap method requires the analysis to be re-run hundreds of times to sample enough of the probability distribution, but the approximate method used here only needs the analysis to be re-run twice. The average of the up and down variations of the final cross-section measurement are summed in quadrature, as the variations are assumed to be independent and therefore uncorrelated. This assumption is reasonable because each systematic uncertainty relates to a different aspect of the reconstruction or the background

estimation, and so the correlations between them are expected to be very small. This sum is then used as the full systematic uncertainty.

By re-evaluating the data-driven scaling of the dijet, $t\bar{t}$ and Z + jets backgrounds, uncertainties in the normalisation of predictions from simulation are essentially cancelled by an equal and opposite change in the data-driven scale factor. While there is an uncertainty in this scale factor, at 6–8% it is much smaller than the systematic uncertainties that are cancelled—for example, theoretical uncertainties on physics modelling can be several tens of percent. This therefore reduces the overall uncertainty in the background estimate. The exceptions to this cancellation are the uncertainties in the b-tagging efficiency, as the b-tagging requirements are different between the various control regions, and the muon systematic uncertainties for the dijets, as the muon p_{T} and trigger is different for Control Region 1. As this cancellation only applies to uncertainties in the normalisation, uncertainties in the shape of distributions are still present.

The systematic uncertainties, grouped by source, in the number of predicted events from MC simulation in the signal region are shown in Table 6.1. The largest source of systematic uncertainty for the W + jets signal is the uncertainty in the jet energy scale at just under 5%. For the dijet and Z + jets backgrounds, the largest is the uncertainty due to data/MC disagreement in their respective control regions at 21% and 13% respectively. For the $t\bar{t}$ background, the largest is the uncertainty in the b-tagging efficiency at 21%. Lastly the uncertainty in the diboson background estimate is dominated by the theoretical uncertainty of the diboson prediction at 49%. While the total systematic uncertainties for the background predictions seem large, they do not have a big effect on the cross-section measurement result because only a small fraction—18%—of events in the signal region are expected to be from these backgrounds.

Table 6.2 shows the systematic uncertainties in the cross-section measurement for the inclusive cross-section, the collinear region ($0.2 < \Delta R < 2.4$) and the back-to-back region

Systematic Source [%]	W + jets	Dijets	$t\bar{t}$	Z + jets	Dibosons
Muon reconstruction efficiency	0.35	0.33	–	–	0.37
Muon momentum scale and resolution	0.02	0.98	–	–	0.25
Muon trigger efficiency	1.79	1.77	–	–	1.82
Jet energy scale	4.82	–	–	–	5.33
Jet energy resolution	0.59	–	–	–	0.48
b-tagging efficiency	1.08	7.87	20.70	1.17	1.52
Scaling of dijets to data	–	6.20	–	–	–
Scaling of $t\bar{t}$ to data	–	–	7.11	–	–
Scaling of Z + jets to data	–	–	–	7.45	–
Data/MC disagreement for dijets	–	20.55	–	–	–
Data/MC disagreement for $t\bar{t}$	–	–	14.59	–	–
Data/MC disagreement for Z + jets	–	–	–	13.15	–
Diboson background estimate	–	–	–	–	48.54
Luminosity	1.90	–	–	–	1.90
Data Statistical	0.60	7.07	4.59	4.97	4.74

Table 6.1: Systematic uncertainties on the number of predicted events from MC simulation in the signal region. Multiple independent systematic components have been combined into groups. Entries with '–' indicate the specific systematic uncertainty has no effect.

($\Delta R > 2.4$). The total systematic uncertainty, excluding the luminosity uncertainty, in the inclusive cross-section measurement is 7.3%. The largest contributions to this are the uncertainties in the jet energy scale at 5% and the uncertainties in the b-tagging efficiency at 3%. All the other systematic uncertainties are smaller than the statistical uncertainty in the data and in the MC samples, both of which are at just over 2%.

The systematic uncertainties in the differential cross-section measurement as a function of the angular separation between the muon and closest jet are shown in Figure 6.1. In each bin across the entire ΔR range, the total systematic uncertainty is smaller than the statistical uncertainty due to the limited size of the data sample.

Systematic Source	$0.2 < \Delta R < 2.4$	$\Delta R > 2.4$	Inclusive
Muon reconstruction efficiency	0.4%	0.4%	0.4%
Muon momentum scale and resolution	0.0%	0.1%	0.1%
Muon trigger efficiency	2.0%	1.9%	1.9%
Jet energy scale	4.6%	5.8%	5.0%
Jet energy resolution	0.6%	0.8%	0.6%
b-tagging efficiency	3.7%	1.2%	2.9%
Scaling of dijets to data	0.4%	0.1%	0.3%
Scaling of $t\bar{t}$ to data	0.6%	0.2%	0.5%
Scaling of Z + jets to data	0.6%	0.3%	0.5%
Data/MC disagreement for dijets	0.9%	0.6%	0.8%
Data/MC disagreement for $t\bar{t}$	1.2%	0.4%	1.0%
Data/MC disagreement for Z + jets	0.6%	1.5%	0.9%
Diboson background estimate	2.2%	0.1%	1.5%
Unfolding dependence on prior	1.1%	1.8%	1.3%
MC background statistical	2.4%	1.8%	2.3%
MC response statistical	1.7%	2.2%	1.9%
Total systematic (excluding luminosity)	7.6%	7.4%	7.3%
Luminosity	1.9%	2.0%	2.0%
Data statistical	2.7%	3.6%	2.2%

Table 6.2: Systematic uncertainties in the cross-section measurement. Multiple independent systematic components have been combined into groups.

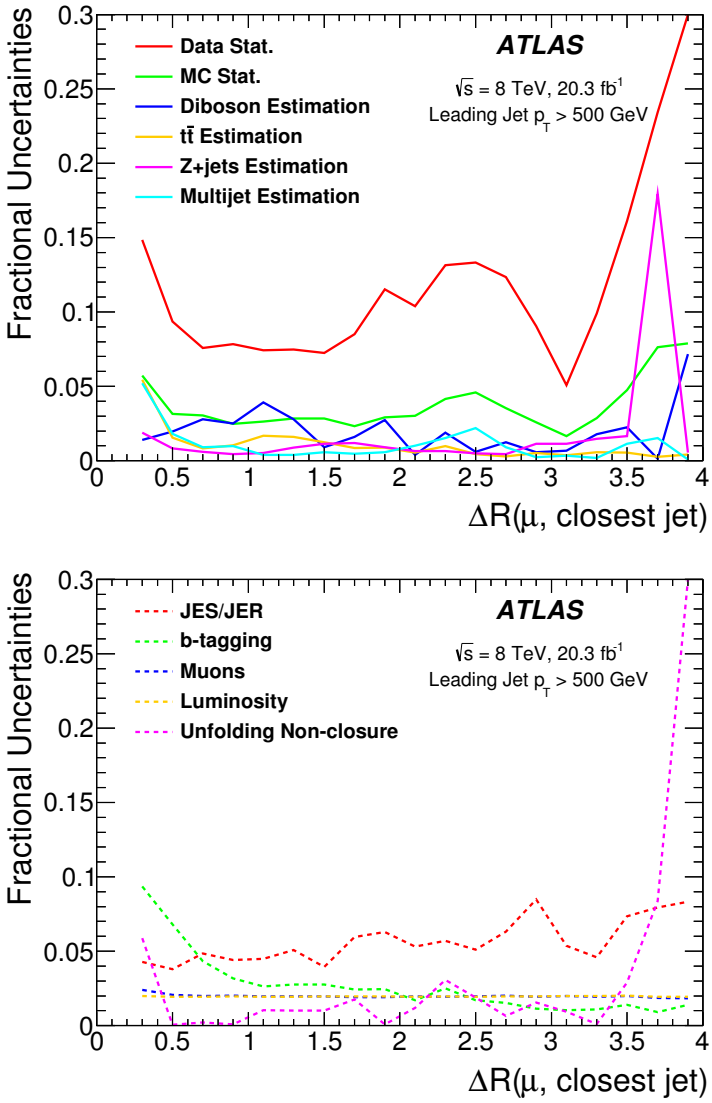

Figure 6.1: Fractional uncertainties, grouped by source, in the differential cross-section measurement as a function of the angular separation between the muon and the closest jet.

6.1 Detector Uncertainties

6.1.1 Muons

The corrections of the muon reconstruction efficiency and the muon momentum scale and resolution in simulated events, described in Section 4.3.1, contain some uncertainties [86]. The resulting uncertainty is around 0.1% for the reconstruction efficiency and around 0.05%–0.2% for the momentum scale. The uncertainty in the momentum resolution is divided into two components, both evaluated independently: the uncertainty in the Inner Detector track p_{T} resolution and the uncertainty in the Muon Spectrometer track p_{T} resolution. Together the total uncertainty in the momentum resolution is between 3% and 10%.

The correction of the muon trigger efficiency in simulated events, described in Section 5.2.2, also contains an uncertainty. The resulting uncertainty in the trigger efficiency is 0.6% [67].

6.1.2 Jets

The uncertainty in the jet energy scale calibration, described in Section 4.3.2, is comprised of 17 independent components [91]. While there are originally 50 components derived from various in-situ analyses, such as Z + jet balance, γ + jet balance and multi-jet balance, by combining many smaller components into several larger ones, this is reduced to six components, decreasing the computational cost of evaluating these uncertainties. This is done in a way that still maintains 97% of the correlation information. Two components are related to the η intercalibration of the jets, and one component is related to a correction for jets whose shower is not fully contained in the calorimeter, so-called punch-through jets. There are also four components that account for the mismodelling of the p_{T} response with respect to pile-up and three topology components that account for the dependence of the p_{T} response uncertainty on the relative fractions of jets initiated by light quarks, gluons and

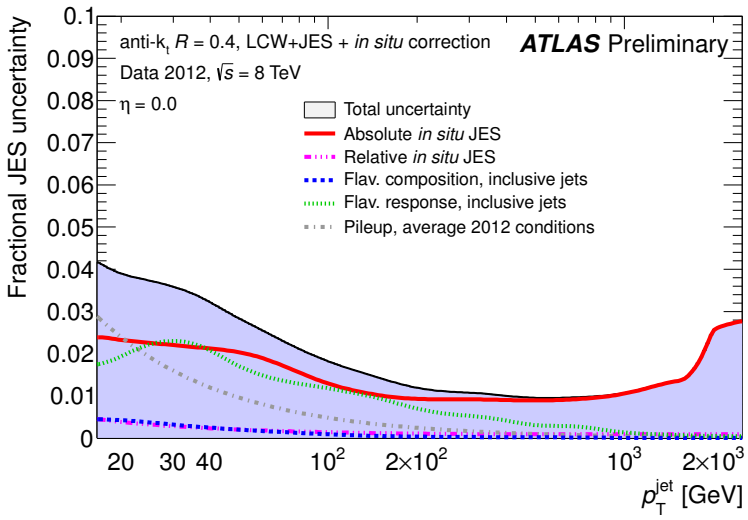

Figure 6.2: Fractional uncertainty in the jet energy scale as a function of jet p_{T}. Source: [107]

b-quarks. For extremely high p_{T} jets with $p_{\mathrm{T}} > 1$ TeV, the calibration is performed using measurements of the single hadron energy response in the calorimeter, and one uncertainty component is derived from this.

The total uncertainty in the jet energy scale is shown in Figure 6.2. For the jets used in this analysis, the uncertainty in p_{T} is between 1% and 2%. Although this seems small, the uncertainty in the jet energy scale is actually the largest source of uncertainty in the cross-section measurement. This is because the leading jet p_{T} distribution is steeply falling in W + jets events and so a small change in jet energy scale can cause a large change in the number of events that pass the leading jet $p_{\mathrm{T}} > 500$ GeV requirement of the analysis. This is demonstrated in Figure 6.3, which shows that a $\pm 1\sigma$ variation in the energy scale causes approximately a $\pm 5\%$ change in the number of W + jets events passing the leading jet p_{T} requirement.

The uncertainty in the jet energy resolution is derived from the difference between the resolution measured in data and the resolution measured in simulated events. For the p_{T} range of this analysis, the resolution uncertainty is around 1% of the jet p_{T} [117].

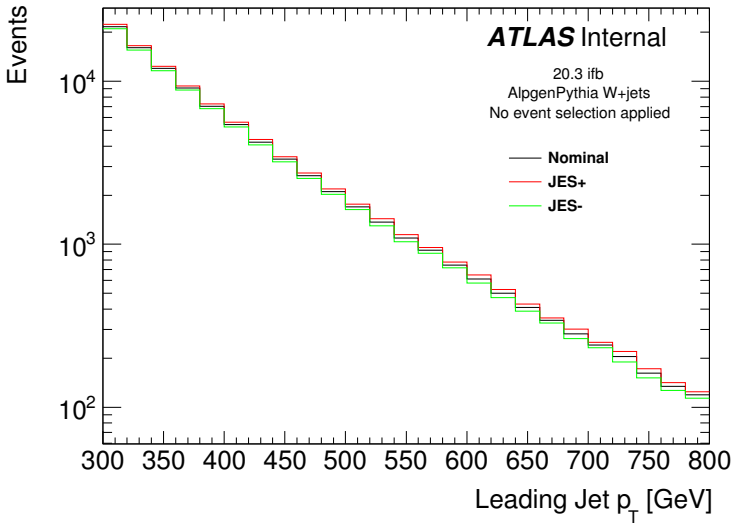

Figure 6.3: The effect of the uncertainty in the jet energy scale on the leading jet p_{T} in simulated W + jets events. The black represents the nominal scale, and the red and green represents a $\pm 1\sigma$ shift in jet energy scale. No event selection criteria are applied.

6.1.3 b-tagging

The b-tagging efficiency and inefficiency corrections applied to simulated events, described in Section 4.3.4, have some uncertainties [100, 101]. For example, the uncertainty in the efficiency of tagging a b-jet, shown in Figure 6.4, varies from 1.8% to 8.4% for b-jets with 20 GeV $< p_{\mathrm{T}} <$ 300 GeV. For b-jets with higher p_{T}, the calibration is extrapolated from the measurement at lower p_{T}, and an additional uncertainty due to this extrapolation is included. The uncertainties for b-, c- and τ-jets are assessed independently from those for light jets, and the uncertainties in the efficiency scale factors are fully anti-correlated with those in the inefficiency scale factors. Figure 6.5 shows the effect of a $\pm 1\sigma$ variation in the b-tagging efficiencies and inefficiencies on the number of b-tags in simulated $t\bar{t}$ events.

6.1.4 Electrons

The effects of uncertainties in the electron energy scale and resolution [95] are evaluated, but they are a negligible contribution to the overall uncertainties—less than 0.01% on the final

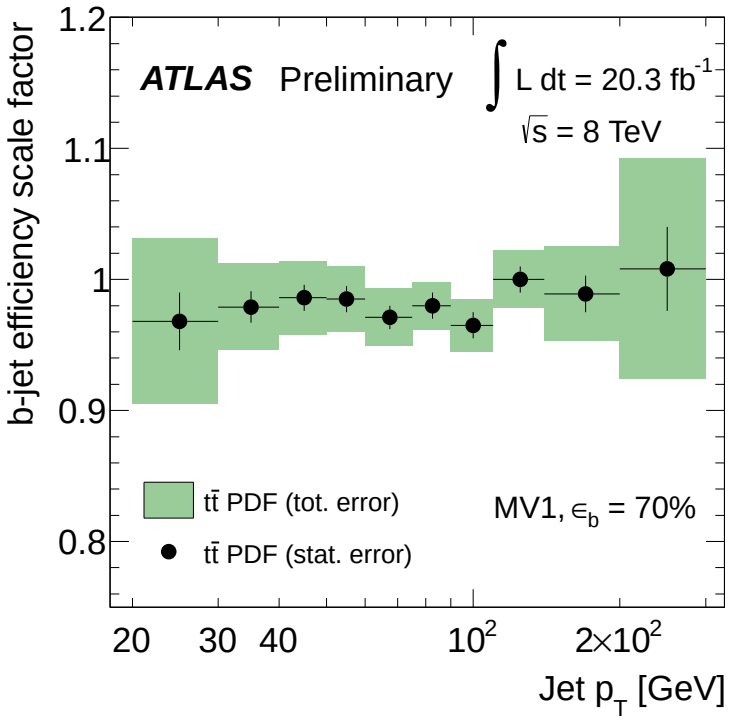

Figure 6.4: The b-tagging efficiency scale factors as a function of jet p_{T} in $t\bar{t}$ events. The shaded bands are the total uncertainties in the scale factors. Source: [101]

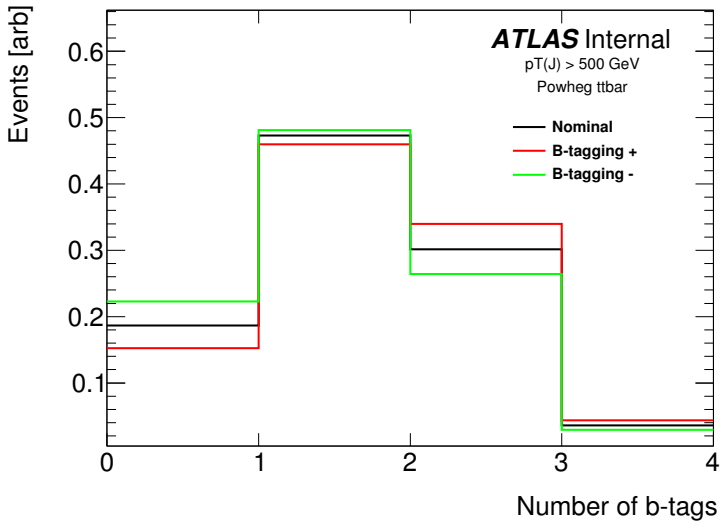

Figure 6.5: The effect of the uncertainty in the b-tagging efficiency and inefficiency on the number of b-tags in simulated $t\bar{t}$ events. The black represents the nominal efficiencies, and the red and green represents a $\pm 1\sigma$ shift. The signal region selection, except for the requirement on the number of b-tags, has been applied.

cross-section result. This is why they are not displayed in Tables 6.1 and 6.2 and Figure 6.1.

6.1.5 Missing Transverse Momentum

Although the missing transverse momentum $E_{\mathrm{T}}^{\mathrm{miss}}$ is not used in the measurement—hence its uncertainties do not appear in Tables 6.1 and 6.2 and Figure 6.1—it is used in the calculation of a few distributions that are plotted. To provide uncertainties on these distributions, the uncertainty in the missing transverse momentum scale and resolution is evaluated. One set of inputs to the calculation of $E_{\mathrm{T}}^{\mathrm{miss}}$, described in Section 4.3.5, are calibrated physics objects. When their uncertainties are assessed through varying their energy scales and resolutions, they are propogated through by simply recalculating $E_{\mathrm{T}}^{\mathrm{miss}}$ with the varied quantities.

The other set of inputs, often termed the soft term, are topo-clusters that are not associated with any physics objects. The uncertainties in the energy scale and resolution of the soft term are derived by comparing $E_{\mathrm{T}}^{\mathrm{miss}}$ in events from data and simulation that contain $Z \to \mu\mu$ and no jets [118]. They are found to be 3.6% for the scale and 2.3% for the resolution. The soft term energy scale and resolution are also varied, and the uncertainties propogated through by recalculating $E_{\mathrm{T}}^{\mathrm{miss}}$.

6.2 Luminosity Uncertainty

The total uncertainty in the integrated luminosity of the data sample is $\pm 1.9\%$ [51]. The two largest components of this are the uncertainties in measuring the beam width for the van der Meer calibration and the uncertainties in transfering this calibration from the low-luminosity environment of the van der Meer scan to the high-luminosity environment of physics running. This uncertainty primarily affects the calculation of the cross-section, which is computed as $\sigma = N/\int \mathcal{L}\, dt$. However, it also affects the diboson background estimate, since this is the only background where the luminosity uncertainty is not cancelled as it is not scaled to data.

6.3 Uncertainty in the Background Estimation

6.3.1 Dijets, $t\bar{t}$ and Z + jets

Since the dijet, $t\bar{t}$ and Z + jets simulated samples are scaled to data in their respective control regions through the procedure of Section 5.5.2, there is a systematic uncertainty in the scaling that arises from the statistical uncertainty in the data and MC samples in these control regions. These uncertainties in the background estimate are 4.8% for dijets, 7.1% for $t\bar{t}$ and 7.5% for Z + jets.

In each control region, any disagreement between the ΔR distributions from data and from MC simulation, shown in Figures 5.8–5.10, is taken as a systematic uncertainty for the ΔR prediction from that specific background in the signal region. This introduces additional data-driven systematic uncertainties that are a function of ΔR for the dijet, $t\bar{t}$ and Z + jets background estimates, shown in Figure 6.6. The binning is chosen such that statistical uncertainty in each bin is not too large, yielding a smooth distribution. The effects of this on the uncertainty in the signal region background estimate are 21% for dijets, 15% for $t\bar{t}$ and 13% for Z + jets.

As the control region for dijets (Control Region 1) does not have the same kinematic selection as the signal region—a different muon isolation and p_{T} requirement are used—there could be some bias due to mismodelling of the dijet kinematics in the simulated sample. To assess this, the kinematic selection of the control region is varied and the dijet scale factor re-evaluated. When the muon p_{T} requirement is increased to $p_{\mathrm{T}}^{\mu} > 50$ GeV, the scale factor decreases by 0.8%. When the muon isolation requirement is loosened such that the muon must have a track isolation energy greater than 35% or a calorimeter isolation energy greater than 50% of the muon p_{T}, the scale factor increases by 4.0%. To account for this potential bias, the largest change in the scale factor, i.e. 4.0%, is introduced as an additional uncertainty in the dijet background estimate.

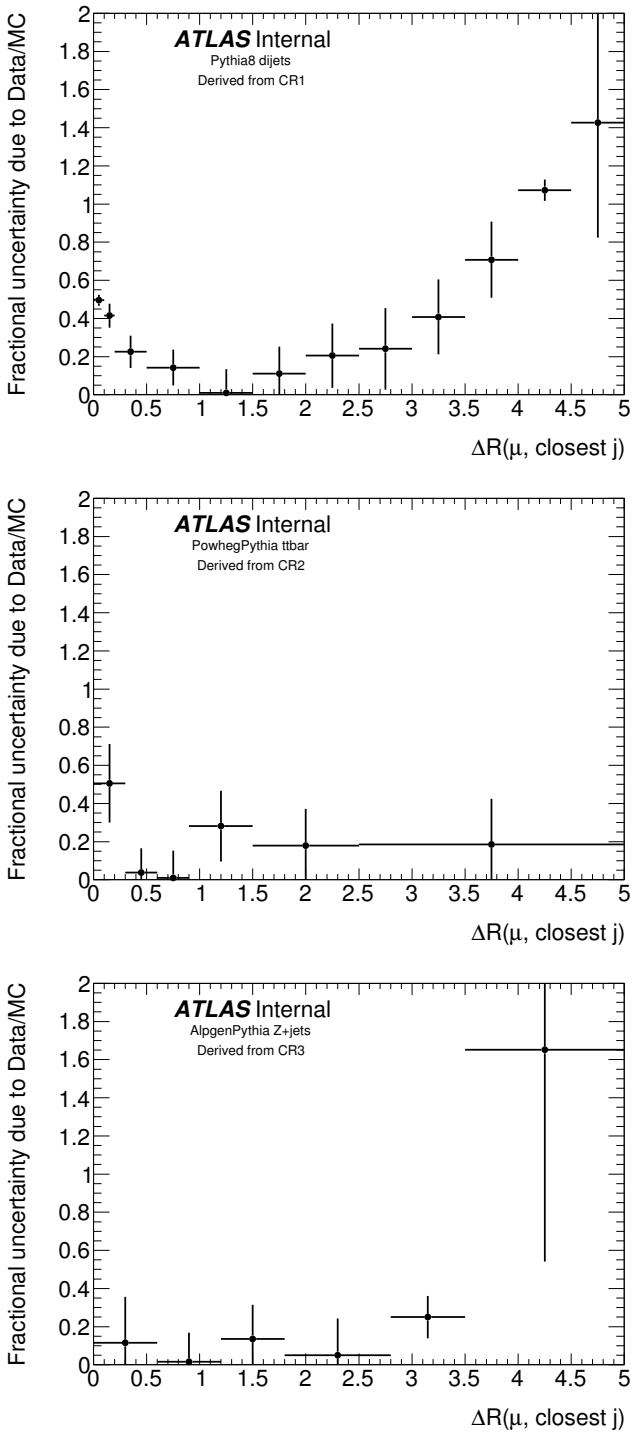

Figure 6.6: Additional systematic uncertainty in the dijet (top), $t\bar{t}$ (middle) and Z + jets (bottom) prediction of the the angular separation between the muon and the closest jet, derived from the agreement of data and MC simulation in the control regions.

6.3.2 Dibosons

Since the diboson background prediction is not constrained by data from a control region, an alternative prediction is obtained from a simulated sample using a different MC generator, SHERPA. The difference between the nominal MC@NLO prediction and the SHERPA prediction is taken as the generator modelling uncertainty in the diboson background estimate. For the overall number of diboson events predicted in the signal region, this uncertainty is almost 50%. Both predictions of the distribution of angular separation between the muon and the closest jet are shown in Figure 6.7, where the lower ratio panel's deviation from one shows the bin-by-bin uncertainty in the diboson background estimate for the signal region. Although this uncertainty is quite large, it only has a moderate 1.5% effect on the uncertainty in the cross-section measurement, as the diboson background is so small—only 3% of events in the signal region are estimated to be diboson events.

Other sources of theoretical uncertainty, such as parton distribution function uncertainties and initial-state radiation (ISR) and final-state radiation (FSR) scale uncertainties, are not evaluated for the diboson background estimate. This is because they are expected to be much smaller than the generator modelling uncertainty and, therefore, have a negligble effect on the cross-section measurement, given the diboson background is so small.

6.4 Unfolding Uncertainty

The iterative Bayesian unfolding, described in Section 5.8.1, requires a prior of the signal distribution, which is obtained from a MC sample of W + jets events generated by ALPGEN. The dependence on this prior introduces a bias in the unfolded results, and, although the iterative approach attempts to reduce this, some residual bias nonetheless remains.

The systematic uncertainty due to this bias in the unfolded cross-section measurement is evaluated through a data-driven closure test [119]. First, the simulated W + jets signal sample is reweighted using a smooth function at particle-level such that the distribution

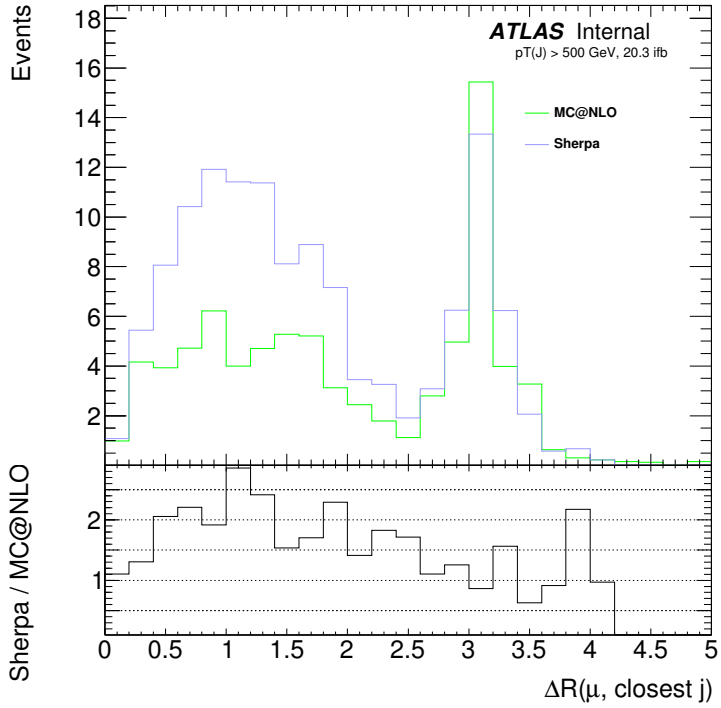

Figure 6.7: The distributions of angular separation between the muon and the closest jet in simulated diboson events generated by SHERPA and MC@NLO. The lower panel shows the ratio of the prediction from SHERPA to MC@NLO. The signal region selection is used, except for the requirement on the number of b-tags.

of the fully simulated detector-level ΔR more closely matches the observed background-subtracted data. The reweighting function used is a fourth-order polynomial of ΔR, whose parameters are derived by performing a fit on the ratio of unfolded data to the particle-level prior. After reweighting, the agreement between the simulated detector-level distribution and the data, shown in the upper plot of Figure 6.8, is improved.

The reweighted detector-level distribution is then unfolded using the same response matrix and prior that is used in the unfolding of the actual data. It is then compared with the reweighted particle-level distribution. If the unfolding were perfect and unbiased, the two would agree perfectly. However, as the lower plot in Figure 6.8 shows, there are differences, and these differences are taken as the systematic uncertainty in the unfolding due to its dependence on the prior. The effect of this non-closure on the uncertainty in the cross-section measurement is 1.3%.

6.5 W + jets Theoretical Uncertainties

Although there are theoretical uncertainties in the W + jets signal prediction, such as uncertainties in the generator modelling, parton distribution function and ISR/FSR scales, these are not evaluated as they do not affect the measurement of the differential cross-section. This is because these theoretical uncertainties only have a negligble impact on the detector efficiency and response, and these are the only calculated quantities from the simulated W + jets sample that are used in unfolding the background-subtracted data. While the iterative Bayesian unfolding does rely on a particle-level prior that is taken from the simulated W + jets sample, the bias due to this dependence is already taken as an uncertainty (see Section 6.4), and so the uncertainty in the prior does not need to be considered. Since they are not evaluated, W + jets theoretical uncertainties are not included in the total uncertainty bands of detector-level distribution plots.

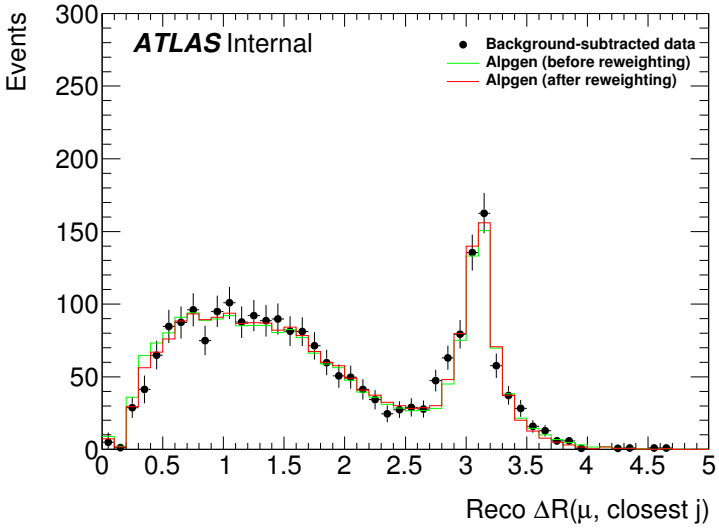

(a)

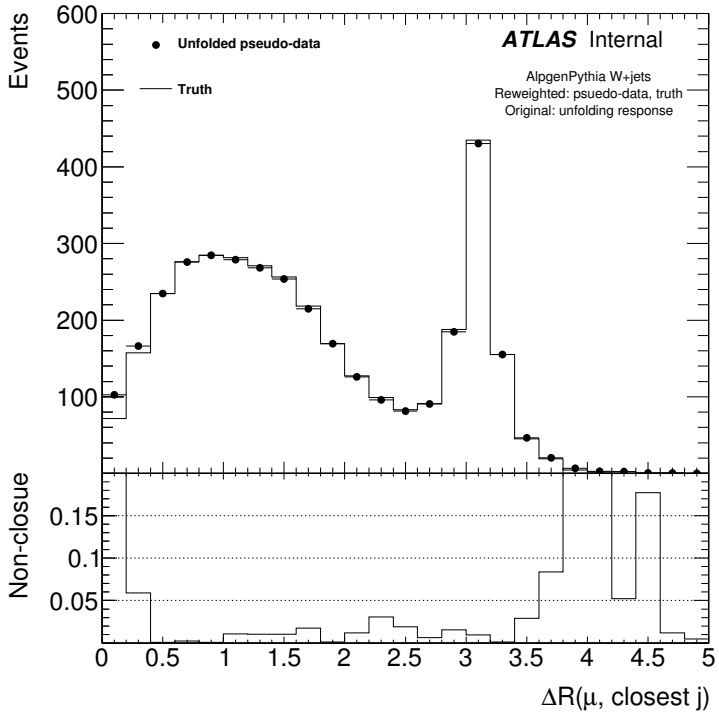

(b)

Figure 6.8: Evaluation of the systematic uncertainty in the unfolding due to its dependence on the prior. (a) shows the detector-level distributions of ΔR in simulated W + jets events before and after a smooth reweighting at particle-level, along with the distribution in background-subtracted data. (b) shows the unfolded reweighted detector-level distribution of ΔR, along with the true reweighted particle-level distribution. The lower panel of (b) shows the fractional difference between the two, and this non-closure is taken as the uncertainty in the unfolding.

CHAPTER 7

RESULTS

7.1 Detector-level Results

After applying the event selection of the signal region, detailed in Section 5.4, to the data collected during 2012, which corresponds to an integrated luminosity of $\int \mathcal{L}\, dt = 20.3$ fb^{-1}, just over 2700 events remain. Based on the estimated composition of these events from MC simulation in Table 5.1, approximately 2250 are expected to be W + jets signal events, split into roughly 1520 events in the $0.2 < \Delta R < 2.4$ collinear region and 730 events in the $\Delta R > 2.4$ back-to-back region.

The distribution from data and the distribution predicted from MC simulation of the angular separation between the muon and the closest jet at detector-level in the signal region are shown in Figure 7.1. Since the W + jets MC sample is scaled using the iterative procedure of Section 5.5.2, the total number of events predicted from MC simulation is almost the same as the number of events in data by construction. Therefore it is unsuprising that the normalisations of data and MC prediction agree in Figure 7.1. As regards the shape, the data is consistent with the MC prediction to within uncertainties in every ΔR bin, except for the regions of $0.3 < \Delta R < 0.4$ and $2.7 < \Delta R < 2.9$. Compared to the MC prediction, there is a 25% deficit in data for $0.3 < \Delta R < 0.4$ and a 40% excess in data for $2.7 < \Delta R < 2.9$. Despite these two small disagreements, the shape of the ALPGEN+PYTHIA6 W + jets MC simulation is a reasonably good description of the W + jets shape in data. This is also supported by the reduced chi-squared statistic for the agreement between data and MC simulation having a value around one, which indicates good agreement. However, from its scale factor of 0.711 ± 0.016, the overall number of W + jets events predicted by ALPGEN+PYTHIA6 is much less accurate.

The same distributions shown in Section 5.5.3 (Figures 5.11–5.22) for validating the

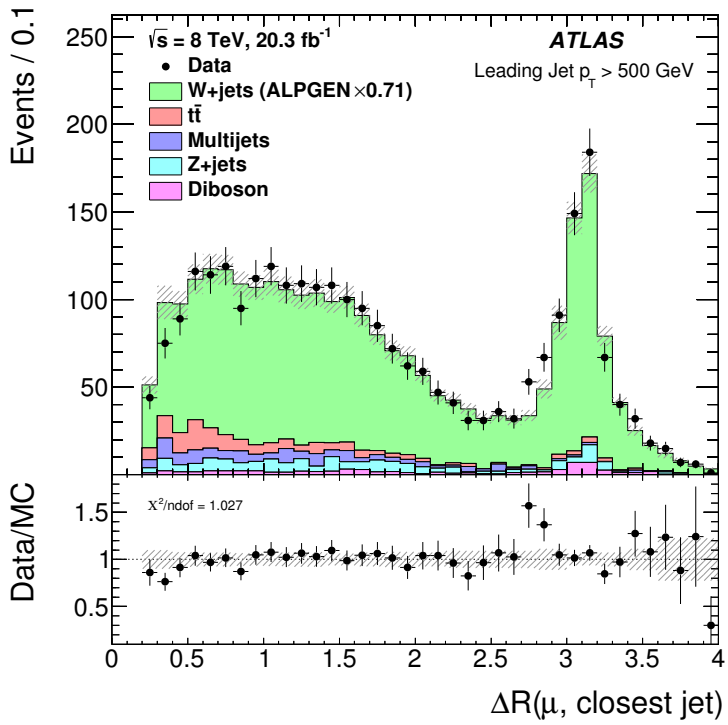

Figure 7.1: Distributions from data and from MC simulation of the angular separation between the muon and the closest jet in the signal region. The lower panel shows the ratio of data to MC simulation. The error bars correspond to the statistical uncertainty and the shaded error bands correspond to the systematic uncertainties. The dijet, $t\bar{t}$ and Z + jets backgrounds have been scaled according to their respective control regions. The W + jets signal has been scaled by 0.71. The reduced chi-squared statistic for the agreement between data and MC simulation is also shown.

modelling of the main background processes are examined in the signal region. To focus on the collinear W boson fraction and remove the back-to-back W + jets production, the same distributions are also examined with an additional cut of $\Delta R < 2.5$ applied. The distributions of transverse momentum, pseudorapidity and azimuthal angle are shown in Figure 7.2 for the muon and in Figure 7.3 for the closest jet to the muon. The distributions of missing transverse energy and candidate W boson transverse mass are shown in Figure 7.4. The distributions of the cosine of the polar decay angle and the azimuthal decay angle in the rest frame of the jet + W system, measured with respect to the vector connecting the lab frame to the rest frame of the jet + W system, are shown in Figure 7.5. The distributions of the angular separation between the muon and the closest jet for events with a positively and a negatively charged muon are shown in Figure 7.6. Generally good agreement within the uncertainties between the data and the MC prediction is seen in these distributions, indicating again that ALPGEN+PYTHIA6 performs well at modelling W + jets production, except for the overall cross-section.

Notably, the transverse mass distribution of Figure 7.4 shows the expected Jacobian peak at the W boson mass of 80 GeV. This demonstrates that the analysis selection used is successful at selecting leptonic W boson decays and reconstructing them using the correctly-chosen muon.

As mentioned earlier, the cosine of the polar decay angle and the azimuthal decay angle in the rest frame of the jet + W system are also able to discriminate collinear W boson production from back-to-back W + jets production. This is because the topologies for these two production modes are very different, leading to the distributions having dissimilar shapes. Figure 7.7 shows these distributions from MC simulation for collinear W boson events in magenta and back-to-back W + jets events in cyan. Qualitatively comparing these to the right-hand plots of Figure 7.5, it is clear the two angular distributions observed in data events with $\Delta R < 2.5$ closely resemble the collinear W boson distributions of Figure 7.7 and

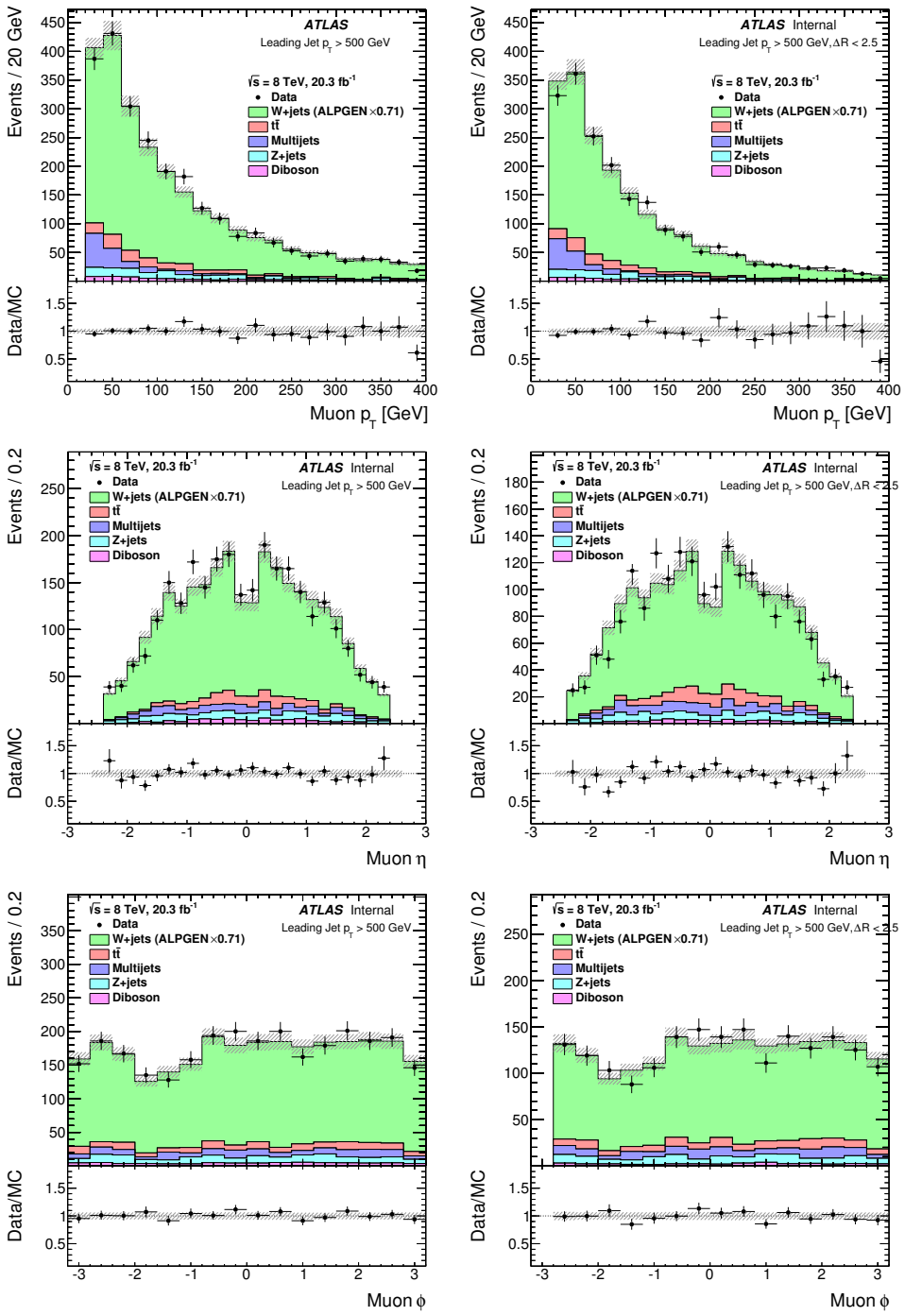

Figure 7.2: Distributions from data and from MC simulation of the muon p_{T} (upper), η (middle) and ϕ (lower) in the signal region. The right plots have a $\Delta R < 2.5$ cut applied. The lower panel shows the ratio of data to MC simulation. The error bars correspond to the statistical uncertainty and the shaded error bands correspond to the systematic uncertainties. The dijet, $t\bar{t}$ and Z + jets backgrounds have been scaled according to their respective control regions. The W + jets signal has been scaled by 0.71.

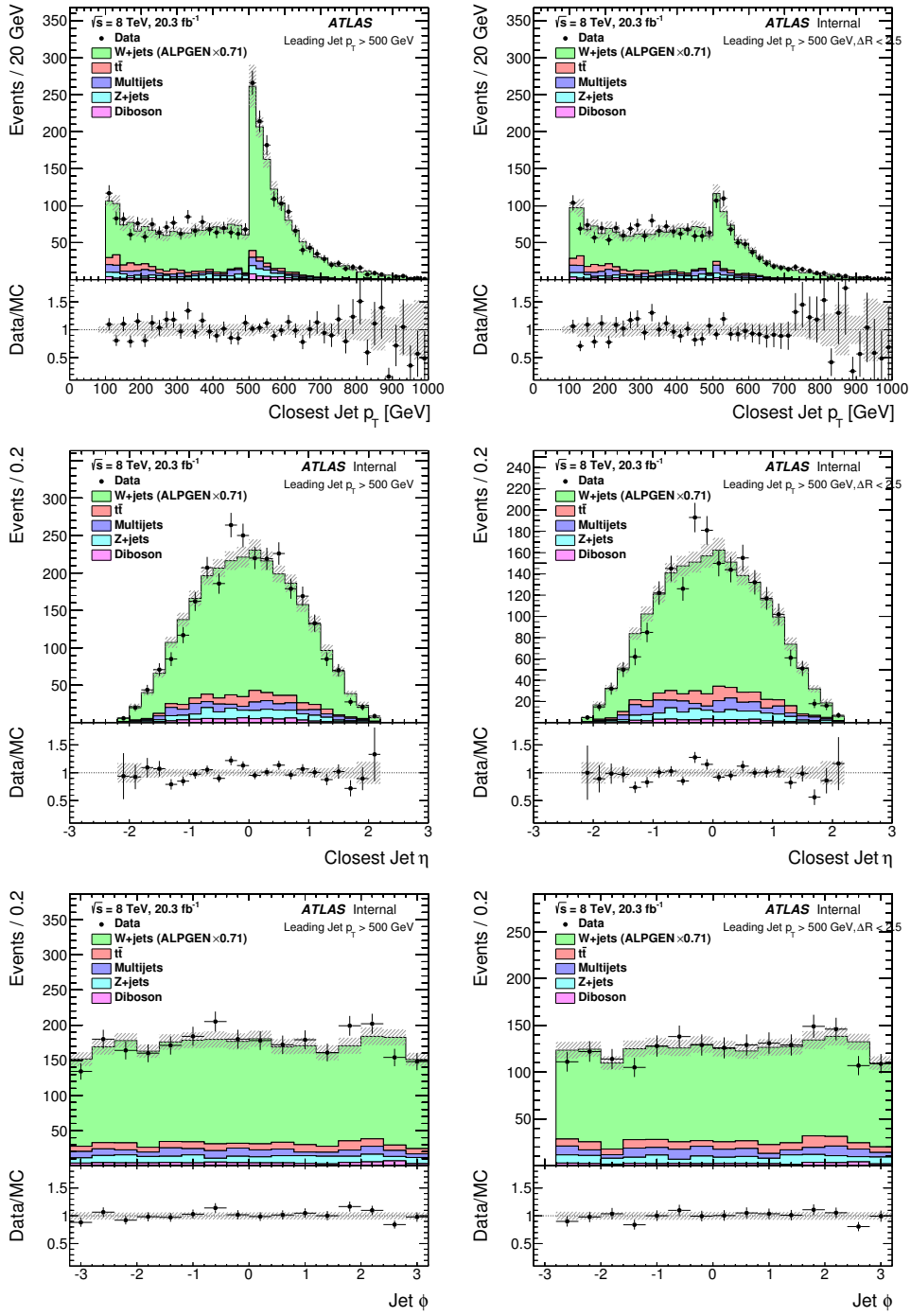

Figure 7.3: Distributions from data and from MC simulation of the p_{T} (upper), η (middle) and ϕ (lower) of the jet closest to the muon in the signal region. The right plots have a $\Delta R < 2.5$ cut applied. The lower panel shows the ratio of data to MC simulation. The error bars correspond to the statistical uncertainty and the shaded error bands correspond to the systematic uncertainties. The dijet, $t\bar{t}$ and Z + jets backgrounds have been scaled according to their respective control regions. The W + jets signal has been scaled by 0.71.

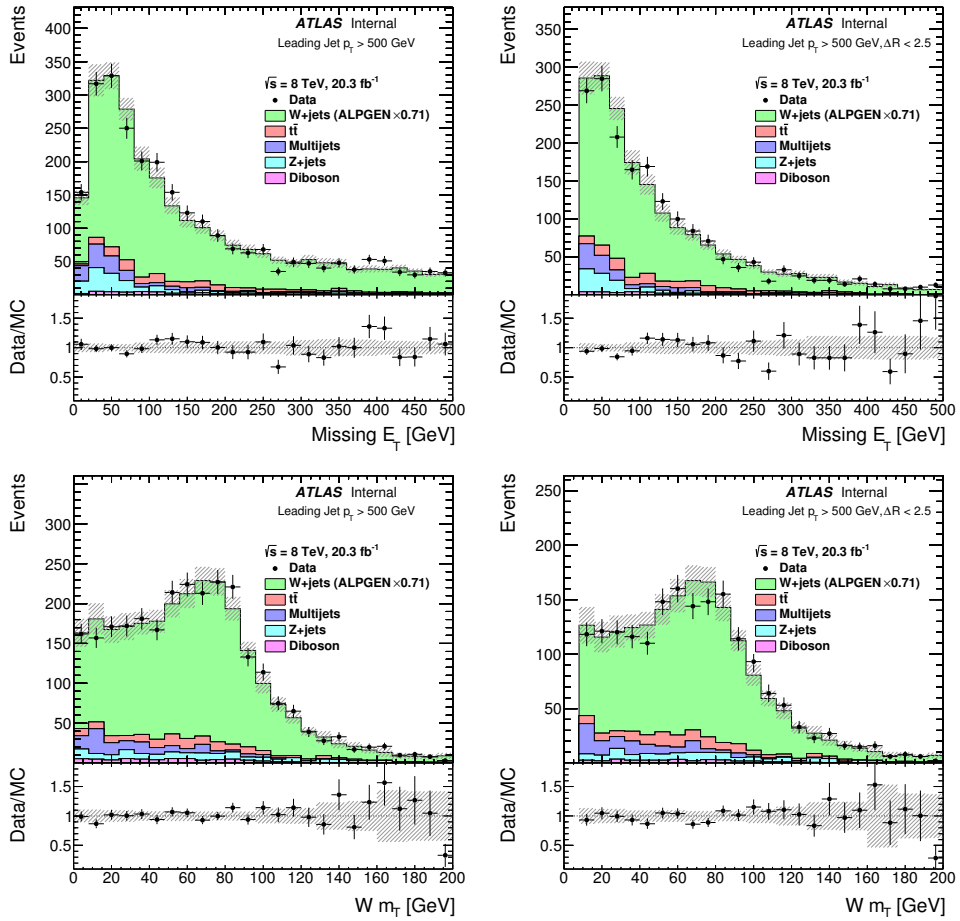

Figure 7.4: Distributions from data and from MC simulation of the $E_{\mathrm{T}}^{\mathrm{miss}}$ (upper) and m_T (lower) in the signal region. The right plots have a $\Delta R < 2.5$ cut applied. The lower panel shows the ratio of data to MC simulation. The error bars correspond to the statistical uncertainty and the shaded error bands correspond to the systematic uncertainties. The dijet, $t\bar{t}$ and Z + jets backgrounds have been scaled according to their respective control regions. The W + jets signal has been scaled by 0.71.

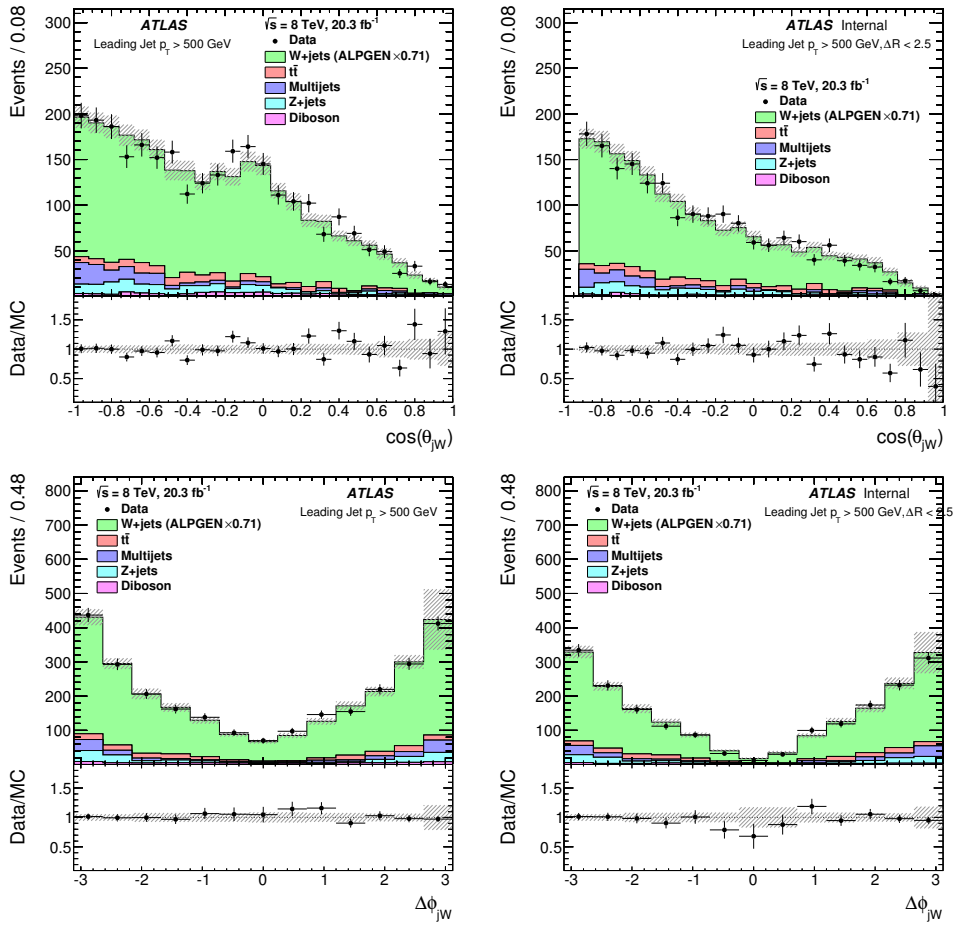

Figure 7.5: Distributions from data and from MC simulation of the cosine of the polar decay angle (upper) and the azimuthal decay angle (lower) in the rest frame of the jet + W system in the signal region. The angles are measured with respect to the vector connecting the lab frame to the rest frame of the jet + W system. The right plots have a $\Delta R < 2.5$ cut applied. The lower panel shows the ratio of data to MC simulation. The error bars correspond to the statistical uncertainty and the shaded error bands correspond to the systematic uncertainties. The dijet, $t\bar{t}$ and Z + jets backgrounds have been scaled according to their respective control regions. The W + jets signal has been scaled by 0.71.

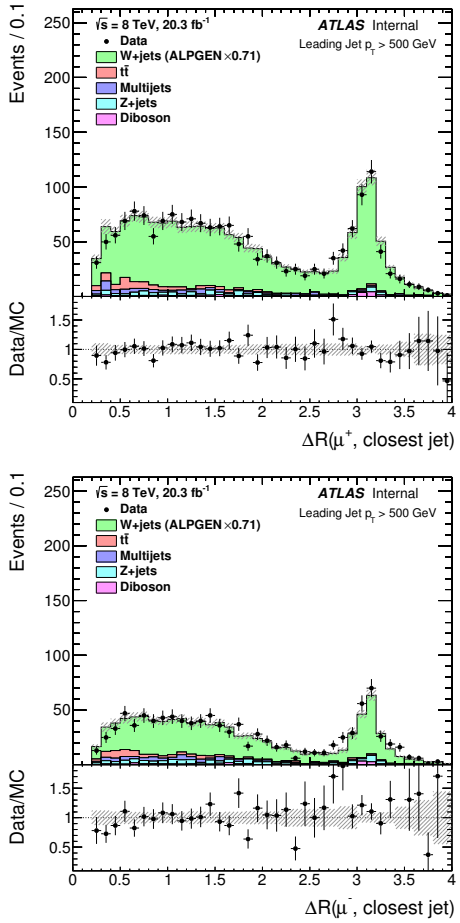

Figure 7.6: Distributions from data and from MC simulation of the angular separation between the muon and the closest jet for events with a postively (upper) and a negatively (lower) charged muon in the signal region. The lower panel shows the ratio of data to MC simulation. The error bars correspond to the statistical uncertainty and the shaded error bands correspond to the systematic uncertainties. The dijet, $t\bar{t}$ and Z + jets backgrounds have been scaled according to their respective control regions. The W + jets signal has been scaled by 0.71.

not the back-to-back W + jets distributions. This further validates the presence of collinear W production in data events from the collinear region.

Although W^+ boson production is expected to outnumber W^- boson production at the LHC and this charge asymmetry has been measured before [120], the amount of charge asymmetry might differ between collinear W boson production and back-to-back W + jets production. The fraction of events that are W^+ boson events as a function of the angular separation between the muon and the closest jet from W + jets MC simulation and from background-subtracted data are shown in Figure 7.8. The positive fraction from data is constant within statistical uncertainty across the ΔR range, suggesting that the charge asymmetry is the same for both collinear W production and back-to-back W + jets production. Overall, the positive fraction is 0.652 ± 0.012 in data, where the quoted uncertainty is statistical uncertainty in the data and background MC samples.

7.2 Differential Cross-section Measurement

The background is estimated using MC simulation that is constrained to control region data through the scaling procedure of Section 5.5.2, and this is then subtracted from the ΔR distribution measured at detector-level in data (Figure 7.1). Next, the background-subtracted data distribution is unfolded using the procedure of Section 5.8 to correct for the signal region selection efficiency and detector effects. The resulting differential cross-section of $W(\rightarrow \mu\nu) + \geq 1$ jet as a function of the angular separation between the muon and the closest jet is shown in Figure 7.9. The measured total cross-section is also listed in Table 7.1, and in Tables 7.2 and 7.3 for the collinear $0.2 < \Delta R < 2.4$ region and back-to-back $\Delta R > 2.4$ region respectively.

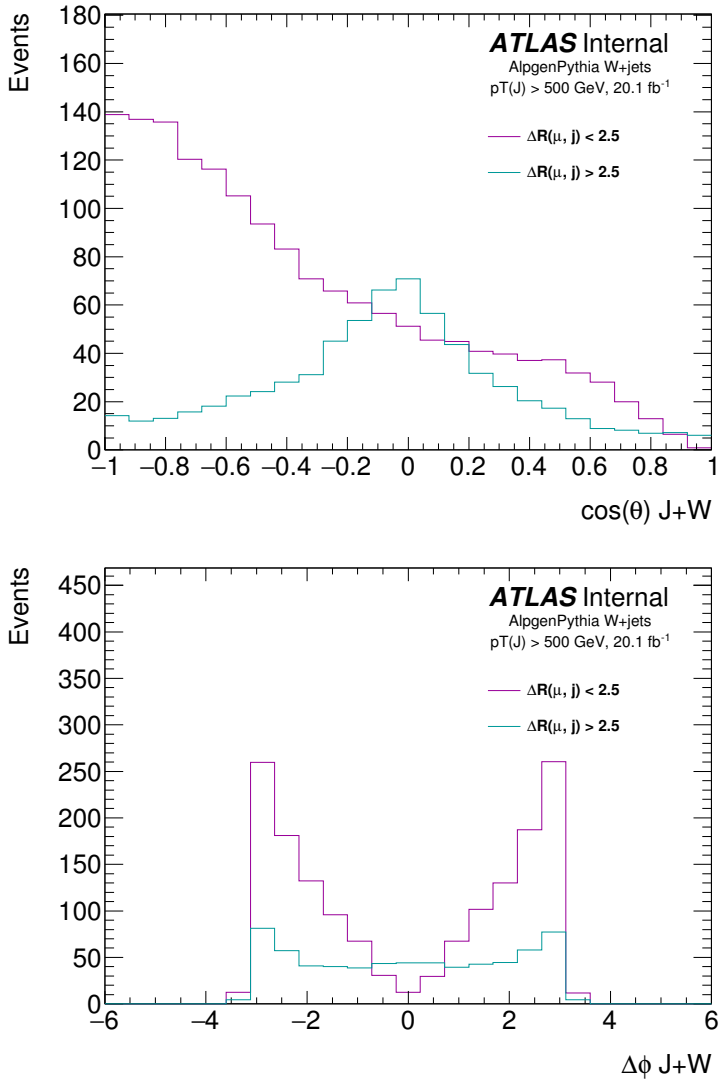

Figure 7.7: Predicted distribution from MC simulation of the cosine of the polar decay angle (upper) and the azimuthal decay angle (lower) in the rest frame of the jet + W system for collinear W boson events (magenta) and back-to-back W + jets events (cyan) in the signal region. Here, collinear is defined as $\Delta R < 2.5$ and back-to-back is defined as $\Delta R > 2.5$.

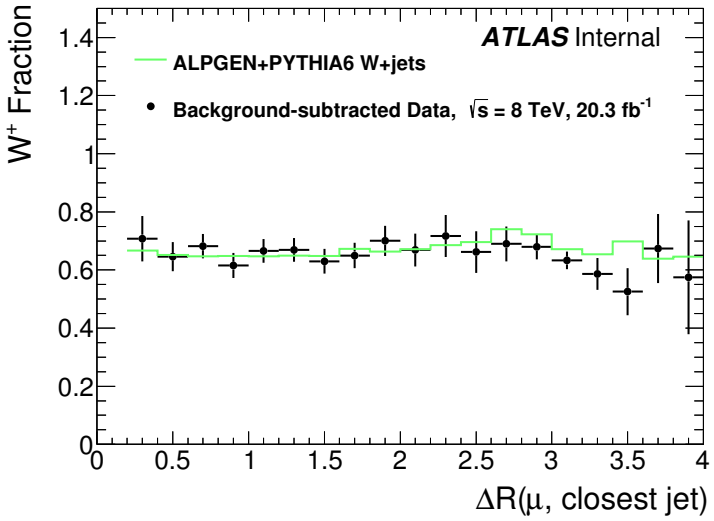

Figure 7.8: Fraction of events with a positively charged muon as a function of the angular separation between the muon and the closest jet from W + jets MC and from background-subtracted data in the signal region. The error bars correspond to the statistical uncertainty only.

Process	$\sigma\,(W(\to \mu\nu) + \geq 1$ jet) [fb]
Data ($\sqrt{s} = 8$ TeV, 20.3 fb^{-1})	169.2 ± 3.7 (stat.) ± 12.3 (syst.) ± 3.3 (lumi.)
ALPGEN+PYTHIA6 W+jets	236.6 ± 1.1 (stat.)
PYTHIA8 W+j & jj+weak shower	134.8 ± 0.9 (stat.) ± 7.3 (pdf)
SHERPA+OpenLoops W+j & W+jj	183 ± 25 (scale)
$W + \geq 1$ jet N_{jetti} NNLO	181 ± 14 (scale)

Table 7.1: Cross-section of $W(\to \mu\nu) + \geq 1$ jet as measured in data, along with several predictions from theory calculations.

Process	$\sigma\,(W(\to \mu\nu) + \geq 1$ jet, $0.2 < \Delta R < 2.4)$ [fb]
Data ($\sqrt{s} = 8$ TeV, 20.3 fb^{-1})	116.2 ± 3.2 (stat.) ± 8.8 (syst.) ± 2.3 (lumi.)
ALPGEN+PYTHIA6 W+jets	167.1 ± 0.9 (stat.)
PYTHIA8 W+j & jj+weak shower	83.4 ± 0.7 (stat.) ± 4.4 (pdf)
SHERPA+OpenLoops W+j & W+jj	128 ± 20 (scale)
$W + \geq 1$ jet N_{jetti} NNLO	123 ± 9 (scale)

Table 7.2: Cross-section of $W(\to \mu\nu) + \geq 1$ jet in the collinear ($0.2 < \Delta R < 2.4$) region as measured in data, along with several predictions from theory calculations.

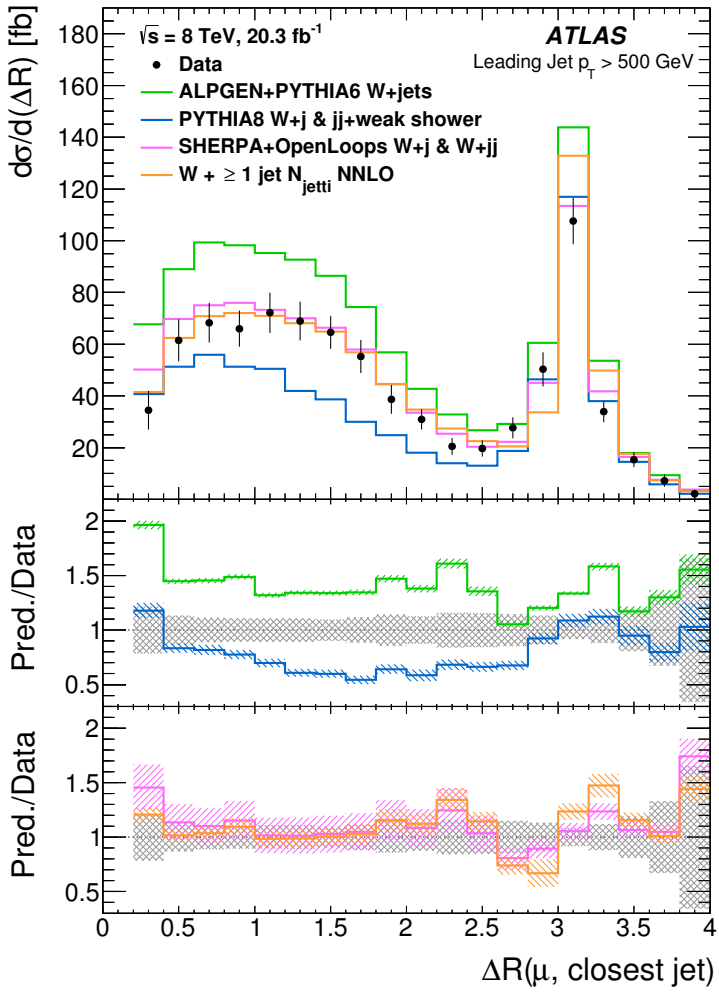

Figure 7.9: Differential cross-section of $W(\rightarrow \mu\nu) + \geq 1$ jet as a function of the angular separation between the muon and the closest jet as measured in data, along with several predictions from theory calculations. The lower panels show the ratio of the theory predictions to the measurement from data. The error bars in the upper panel and the grey shaded error bands in the lower ratio panels are the sum of the statistical and systematic uncertainties in the measurement. The shaded error band on the ALPGEN+PYTHIA6 calculation is statistical uncertainty, the band on the PYTHIA8 calculation is statistical and PDF uncertainties and those on the SHERPA+OpenLoops calculation and the $W + \geq 1$ jet N_{jetti} NNLO calculation are scale uncertainties.

Process	$\sigma\,(W(\to \mu\nu) + \geq 1$ jet, $\Delta R > 2.4)$ [fb]
Data ($\sqrt{s} = 8$ TeV, 20.3 fb^{-1})	53.0 ± 1.9 (stat.) ± 3.9 (syst.) ± 1.0 (lumi.)
ALPGEN+PYTHIA6 W+jets	69.5 ± 0.6 (stat.)
PYTHIA8 $W+j$ & jj+weak shower	51.4 ± 0.6 (stat.) ± 2.9 (pdf)
SHERPA+OpenLoops $W+j$ & $W+jj$	55 ± 5 (scale)
$W + \geq 1$ jet N_{jetti} NNLO	58 ± 5 (scale)

Table 7.3: Cross-section of $W(\to \mu\nu) + \geq 1$ jet in the back-to-back ($\Delta R > 2.4$) region as measured in data, along with several predictions from theory calculations.

7.3 Comparison with Theory Predictions

The cross-section measurements in Figure 7.9 and Tables 7.1–7.3 are compared to four predictions from theory calculations. The details and setup of these theory calculations are given in Sections 2.4.1–2.4.4.

The uncertainties given on the ALPGEN+PYTHIA6 calculation are the statistical uncertainties of the MC sample. The uncertainties given on the PYTHIA8 calculation are the sums of the statistical uncertainties of the MC sample and the uncertainties from the CT10 NLO PDF set. The uncertainties given on the SHERPA+OpenLoops calculation and the $W + \geq 1$ jet N_{jetti} NNLO calculation are scale uncertainties. These were derived by varying the renormalisation scale and the factorisation scale independently by a factor of two, excluding the anti-diagonal. This leads to the following combinations of renormalisation scales μ_{R} and factorisation scales μ_{F} being evaluated: $(\mu_{\text{R}}, \mu_{\text{F}}) = (\mu_0, \mu_0)$, $(2\mu_0, \mu_0)$, $(\mu_0, 2\mu_0)$, $(2\mu_0, 2\mu_0)$, $(\mu_0, \mu_0/2)$, $(\mu_0/2, \mu_0)$, $(\mu_0/2, \mu_0/2)$.

Ideally, all four predictions would be given with the same set of uncertainties, for example PDF and scale uncertainties, evaluated to enable a more fair comparison. However, this is not done for the following reasons. PDF uncertainties are not included for the ALPGEN+PYTHIA6 calculation, because the authors of Ref. [29] did not provide any uncertainties on the CTEQ6L1 LO PDF that is used. The SHERPA+OpenLoops calculation and the $W + \geq 1$ jet N_{jetti} NNLO calculation were provided by the authors of Ref. [35] and Ref. [44]

respectively, and they did not evaluate PDF uncertainties. Scale uncertainties are not included for the ALPGEN+PYTHIA6 and PYTHIA8 calculations, because the computational cost of producing new MC samples with the scales varied was prohibitive.

The comparison of the differential cross-section measurement to predictions from ALPGEN+PYTHIA6 in Figure 7.9 shows good shape agreement to within uncertainties, except for the $0.2 < \Delta R < 0.4$ and $2.6 < \Delta R < 2.8$ bins, but ALPGEN+PYTHIA6 predicts an integrated cross-section that is 40% higher. The comparison to predictions from PYTHIA8 at large angular separation, $\Delta R > 2.8$ where it is dominated by back-to-back W + jets production in which the W boson is balanced by the hadronic recoil system, shows good agreement to within uncertainties. At smaller angular seperation, $\Delta R < 2.8$ where the collinear process dominates, the shape disagrees and the predicted cross-section is approximately 30% lower. The comparisons to the SHERPA+OpenLoops calculation and the $W + \geq 1$ jet N_{jetti} NNLO calculation show much better agreement across most of the ΔR distribution, and the predicted total cross-sections are consistent with the measurement to within uncertainties.

7.4 Enhancement with Jet p_{T}

The relative rate of collinear W boson production is expected to depend on the jet energies, as the NLO corrections to $W + \geq 1$-jet production have a leading logarithmic term that scales with the jet p_{T}. To probe this, the events of the signal region are divided into two categories based on the transverse momentum of the leading jet: 500 GeV $< p_{\mathrm{T}}^{\text{leading jet}} <$ 600 GeV and $p_{\mathrm{T}}^{\text{leading jet}} > 650$ GeV. For each of these two categories, the ΔR distribution is unfolded independently in the same manner as Section 7.2. The 50 GeV gap between the two categories reduces the migration of events from one category to the other during unfolding, as the jet energy resolution is approximately half of the gap. As a result, unfolding both independently is a good approximation to a more precise two-dimensional simultaneous unfolding.

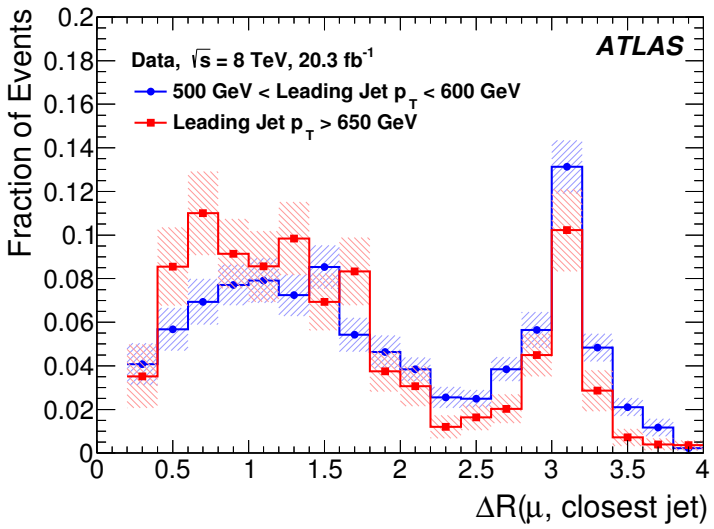

Figure 7.10: Normalised differential cross-sections of $W(\rightarrow \mu\nu) + \geq 1$ jet as a function of the angular separation between the muon and the closest jet as measured in data for 500 GeV $< p_{\mathrm{T}}^{\text{leading jet}} <$ 600 GeV (blue circles) and $p_{\mathrm{T}}^{\text{leading jet}} >$ 650 GeV (red squares). Distributions are normalised to unit area. The shaded error band corresponds to the sum of the statistical and systematic uncertainties.

The resulting differential $W(\rightarrow \mu\nu) + \geq 1$ jet cross-sections for the two leading jet p_{T} categories are shown in Figure 7.10. They are shown normalised to unit area so the shape of the angular separation distribution can be easily compared between the two categories. As the leading jet p_{T} requirement increases, the fraction of the cross-section in the lower ΔR (collinear) region increases and the fraction in the higher ΔR (back-to-back) region decreases. This may be interpreted as an increase in the collinear W boson emission probability, as the quarks become more energetic and are able to emit the massive W boson more easily. With higher p_{T} the collinear peak is also shifted to smaller ΔR, indicating the W boson is emitted closer to the jet axis. This is also understood, since the mass of the W boson becomes proportionally smaller compared to the energy of the jet. In the limit of very high p_{T}, the W boson would be effectively massless and be emitted perfectly collinearly like with gluon emission.

The full non-normalised measurement results are shown in Figures 7.11 and 7.12, along

with predictions from theory calculations. The same theory calculations as in Section 7.3 are used, except the $W + \geq 1$ jet N_{jetti} NNLO calculation is not used as the authors did not provide results for these different leading jet p_{T} categories. Comparing the measurements to theory predictions shows results similar to the ones obtained for $p_{\text{T}}^{\text{leading jet}} > 500$ GeV in Section 7.3.

The possibility of measuring the double differential cross-section using many leading jet p_{T} bins, which would be a much stronger probe of the p_{T} dependence of collinear W boson production, was explored. However, the total integrated luminosity of the 2012 dataset, $\int \mathcal{L}\ dt = 20.3\ \text{fb}^{-1}$, was not sufficient to peform such a double differential measurement. Each bin of $(p_{\text{T}}, \Delta R)$ would only contain a few W + jets events, and so the statistical uncertainty would be very large, rendering the results not useful. Even increasing the number of leading jet p_{T} categories that are used in this section from two to three would cause large statistical fluctuations to appear in the measurement results.

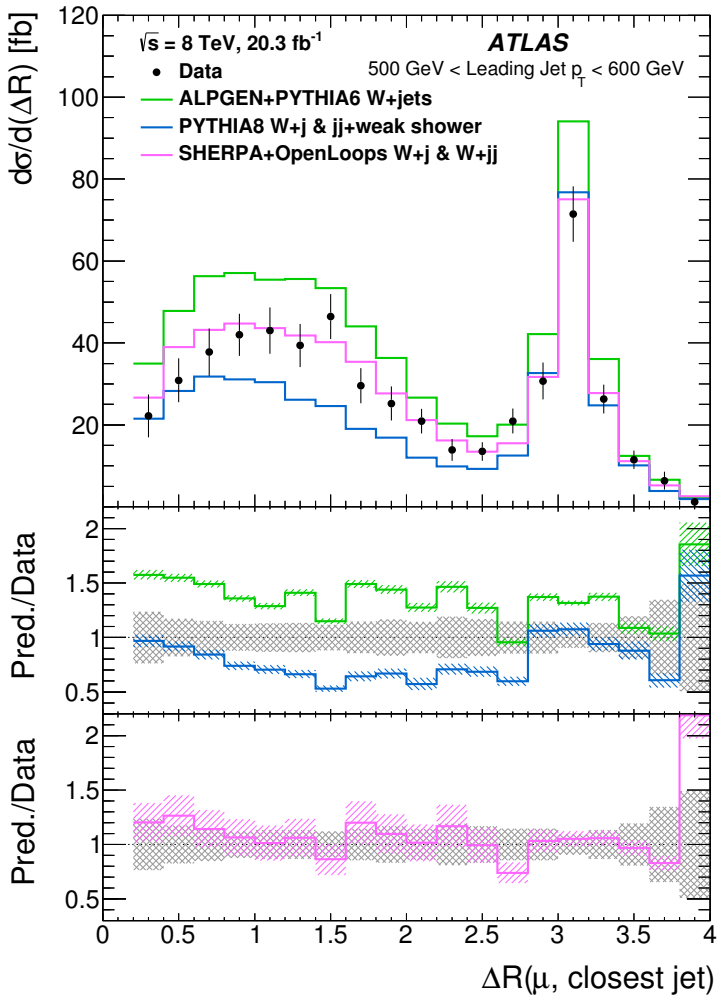

Figure 7.11: Differential cross-section of $W(\rightarrow \mu\nu) + \geq 1$ jet as a function of the angular separation between the muon and the closest jet as measured in data for 500 GeV $< p_{\mathrm{T}}^{\text{leading jet}} <$ 600 GeV, along with several predictions from theory calculations. The lower panels show the ratio of the theory predictions to the measurement from data. The error bars in the upper panel and the grey shaded error bands in the lower ratio panels are the sum of the statistical and systematic uncertainties in the measurement. The shaded error band on the ALPGEN+PYTHIA6 calculation is statistical uncertainty, the band on the PYTHIA8 calculation is statistical and PDF uncertainties and the band on the SHERPA+OpenLoops calculation is scale uncertainty.

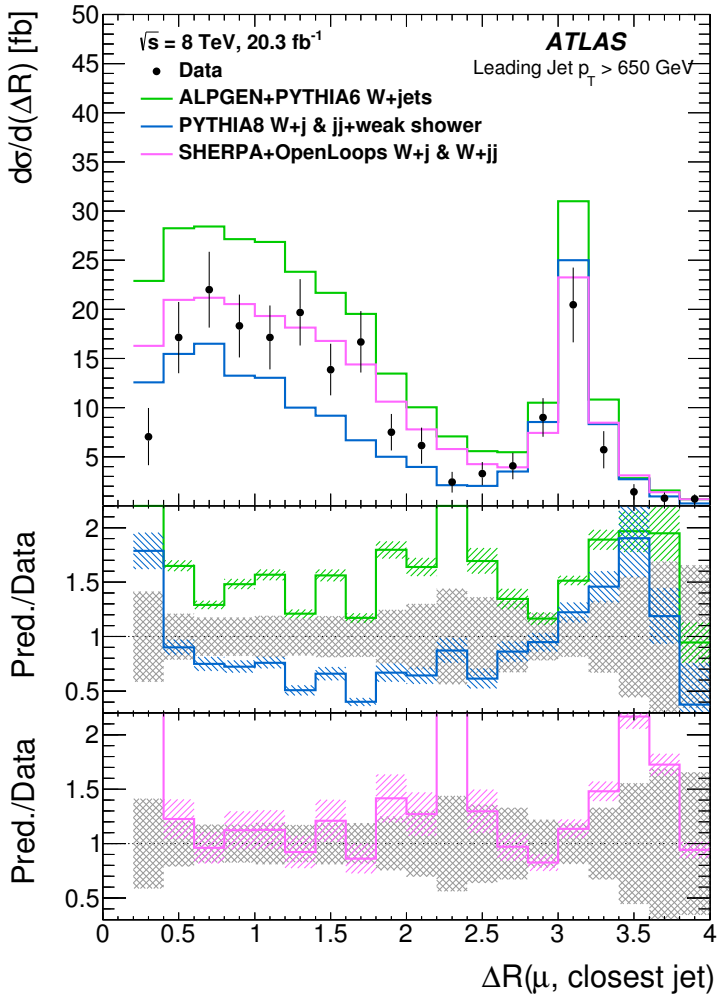

Figure 7.12: Differential cross-section of $W(\rightarrow \mu\nu) + \geq 1$ jet as a function of the angular separation between the muon and the closest jet as measured in data for $p_{\mathrm{T}}^{\text{leading jet}} >$ 650 GeV, along with several predictions from theory calculations. The lower panels show the ratio of the theory predictions to the measurement from data. The error bars in the upper panel and the grey shaded error bands in the lower ratio panels are the sum of the statistical and systematic uncertainties in the measurement. The shaded error band on the ALPGEN+PYTHIA6 calculation is statistical uncertainty, the band on the PYTHIA8 calculation is statistical and PDF uncertainties and the band on the SHERPA+OpenLoops calculation is scale uncertainty.

CHAPTER 8

CONCLUSION

In this thesis, the cross-section for $W \to \mu\nu$ in association with a high-p_{T} jet is measured as a function of the angular separation between the muon from the W boson decay and the closest jet. This measurement utilises data recorded by the ATLAS detector from pp collisions at a centre-of-mass energy $\sqrt{s} = 8$ TeV at the LHC, corresponding to an integrated luminosity of 20.3 fb^{-1}. These are the first studies that explicitly focus on understanding the contribution of real W boson emission from high-p_{T} partons to W + jets processes.

Comparisons of the measurement results to several theoretical predictions of W + jets production show varying levels of agreement. The leading-order calculation from ALPGEN+PYTHIA6 overestimates the total cross-section, whereas the calculation from PYTHIA8, which is modified to include W boson emission through electroweak parton showering, underestimates the cross-section in the collinear region. On the other hand, agreement with the SHERPA+OpenLoops NLO QCD+EW calculation and the $W + \geq 1$ jet N_{jetti} NNLO QCD calculation of Ref. [44] is well within the uncertainties of the predictions and the measurement.

This measurement has implications for Monte Carlo generators that incorporate real W boson emission, a process which is only just now being probed directly at the energy of the LHC. It is also highly relevant for many searches for new physics at the LHC, such as those involving Lorentz-boosted top quarks, where collinear W production can be a significant background through its resemblance to the rare signatures being sought. As the rate increases with jet p_{T} and thus also with centre-of-mass energy, this once scarce process will become a ubiquitous consideration at future higher-energy colliders.

References

[1] ATLAS Collaboration, *Measurement of W boson angular distributions in events with high transverse momentum jets at $\sqrt{s} = 8$ TeV using the ATLAS detector*, Phys. Lett. **B765** (2017) 132–153, arXiv:1609.07045 [hep-ex].

[2] K. Rehermann and B. Tweedie, *Efficient Identification of Boosted Semileptonic Top Quarks at the LHC*, JHEP **03** (2011) 059, arXiv:1007.2221 [hep-ph].

[3] ATLAS Collaboration, *Measurements of the W production cross sections in association with jets with the ATLAS detector*, Eur. Phys. J. C **75** (2015) 82, arXiv:1409.8639 [hep-ex].

[4] CMS Collaboration, *Differential cross section measurements for the production of a W boson in association with jets in protonproton collisions at $\sqrt{s} = 7$ TeV*, Phys. Lett. B **741** (2015) 12, arXiv:1406.7533 [hep-ex].

[5] A. Purcell, *Go on a particle quest at the first CERN webfest. Le premier webfest du CERN se lance la conqute des particules*, https://cds.cern.ch/record/1473657.

[6] M. Kobayashi and T. Maskawa, *CP Violation in the Renormalizable Theory of Weak Interaction*, Prog. Theor. Phys. **49** (1973) 652–657.

[7] H. Harari, *A New Quark Model for Hadrons*, Phys. Lett. **B57** (1975) 265–269.

[8] F. Englert and R. Brout, *Broken Symmetry and the Mass of Gauge Vector Mesons*, Phys. Rev. Lett. **13** (1964) 321–323.

[9] P. W. Higgs, *Broken Symmetries and the Masses of Gauge Bosons*, Phys. Rev. Lett. **13** (1964) 508–509.

[10] G. S. Guralnik, C. R. Hagen, and T. W. B. Kibble, *Global Conservation Laws and Massless Particles*, Phys. Rev. Lett. **13** (1964) 585–587.

[11] D0 Collaboration, *Observation of the top quark*, Phys. Rev. Lett. **74** (1995) 2632–2637, arXiv:hep-ex/9503003 [hep-ex].

[12] CDF Collaboration, *Observation of top quark production in $\bar{p}p$ collisions*, Phys. Rev. Lett. **74** (1995) 2626–2631, arXiv:hep-ex/9503002 [hep-ex].

[13] CMS Collaboration, *Observation of a new boson at a mass of 125 GeV with the CMS experiment at the LHC*, Phys. Lett. **B716** (2012) 30–61, arXiv:1207.7235 [hep-ex].

[14] ATLAS Collaboration, *Observation of a new particle in the search for the Standard Model Higgs boson with the ATLAS detector at the LHC*, Phys. Lett. B **716** (2012) 1, arXiv:1207.7214 [hep-ex].

[15] A. Collaboration, *Summary plots from the ATLAS Standard Model physics group*, https://atlas.web.cern.ch/Atlas/GROUPS/PHYSICS/CombinedSummaryPlots/SM/index.html.

[16] Muon g-2 collaboration, *Measurement of the negative muon anomalous magnetic moment to 0.7 ppm*, Phys. Rev. Lett. **92** (2004) 161802, arXiv:hep-ex/0401008 [hep-ex].

[17] V. C. Rubin, N. Thonnard, and W. K. Ford, Jr., *Rotational properties of 21 SC galaxies with a large range of luminosities and radii, from NGC 4605 /R = 4kpc/ to UGC 2885 /R = 122 kpc/*, Astrophys. J. **238** (1980) 471.

[18] Planck Collaboration, *Planck 2013 results. I. Overview of products and scientific results*, Astron. Astrophys. **571** (2014) A1, arXiv:1303.5062 [astro-ph.CO].

[19] R. Massey et al., *Dark matter maps reveal cosmic scaffolding*, Nature **445** (2007) 286, arXiv:astro-ph/0701594 [astro-ph].

[20] J. M. Cline, *Baryogenesis*, in *Les Houches Summer School - Session 86: Particle Physics and Cosmology: The Fabric of Spacetime Les Houches, France, July 31-August 25, 2006*. 2006. arXiv:hep-ph/0609145 [hep-ph].

[21] A. D. Martin, W. J. Stirling, R. S. Thorne, and G. Watt, *Parton distributions for the LHC*, Eur. Phys. J. **C63** (2009) 189–285, arXiv:0901.0002 [hep-ph].

[22] J. Stirling, *Parton Luminosity and Cross Section Plots*, http://www.hep.ph.ic.ac.uk/~wstirlin/plots/plots.html.

[23] F. Krauss, P. Petrov, M. Schöenherr, and M. Spannowsky, *Measuring collinear W emissions inside jets*, Phys. Rev. **D89** (2014) 114006, arXiv:1403.4788 [hep-ph].

[24] J. H. Kuhn, A. Kulesza, S. Pozzorini, and M. Schulze, *Electroweak corrections to large transverse momentum production of W bosons at the LHC*, Phys. Lett. **B651** (2007) 160–165, arXiv:hep-ph/0703283 [HEP-PH].

[25] T. Sjöstrand, *Monte Carlo – 1. Introduction and Parton Showers*, http://home.thep.lu.se/~torbjorn/talks/van1ho.pdf.

[26] J. R. Christiansen and T. Sjöstrand, *Weak Gauge Boson Radiation in Parton Showers*, JHEP **04** (2014) 115, arXiv:1401.5238 [hep-ph].

[27] J. R. Christiansen and S. Prestel, *Merging weak and QCD showers with matrix elements*, Eur. Phys. J. **C76** (2016) 39, arXiv:1510.01517 [hep-ph].

[28] M. L. Mangano et al., *ALPGEN, a generator for hard multiparton processes in hadronic collisions*, JHEP **07** (2003) 001, arXiv:hep-ph/0206293 [hep-ph].

[29] J. Pumplin et al., *New generation of parton distributions with uncertainties from global QCD analysis*, JHEP **07** (2002) 012, arXiv:hep-ph/0201195.

[30] T. Sjöstrand, S. Mrenna, and P. Z. Skands, *PYTHIA 6.4 Physics and Manual*, JHEP **05** (2006) 026, arXiv:hep-ph/0603175.

[31] S. Hoeche, F. Krauss, N. Lavesson, L. Lonnblad, M. Mangano, A. Schalicke, and S. Schumann, *Matching parton showers and matrix elements*, pp. , 288–289. 2005. arXiv:hep-ph/0602031 [hep-ph].

[32] R. Gavin, Y. Li, F. Petriello, and S. Quackenbush, *FEWZ 2.0: A code for hadronic Z production at next-to-next-to-leading order*, Comput. Phys. Commun. **182** (2011) 2388–2403, arXiv:1011.3540 [hep-ph].

[33] T. Sjöstrand, S. Mrenna, and P. Z. Skands, *A Brief Introduction to PYTHIA 8.1*, Comput. Phys. Commun. **178** (2008) 852, arXiv:0710.3820 [hep-ph].

[34] H.-L. Lai, M. Guzzi, J. Huston, Z. Li, P. M. Nadolsky, J. Pumplin, and C. P. Yuan, *New parton distributions for collider physics*, Phys. Rev. **D82** (2010) 074024, arXiv:1007.2241 [hep-ph].

[35] S. Kallweit, J. M. Lindert, P. Maierhöfer, S. Pozzorini, and M. Schönherr, *NLO electroweak automation and precise predictions for W+multijet production at the LHC*, JHEP **04** (2015) 012, arXiv:1412.5157 [hep-ph].

[36] F. Cascioli, P. Maierhofer, and S. Pozzorini, *Scattering Amplitudes with Open Loops*, Phys. Rev. Lett. **108** (2012) 111601, arXiv:1111.5206 [hep-ph].

[37] A. Denner, S. Dittmaier, and L. Hofer, *COLLIER - A fortran-library for one-loop integrals*, PoS **LL2014** (2014) 071, arXiv:1407.0087 [hep-ph].

[38] T. Gleisberg, S. Höche, F. Krauss, M. Schönherr, S. Schumann, et al., *Event generation with SHERPA 1.1*, JHEP **02** (2009) 007, arXiv:0811.4622 [hep-ph].

[39] F. Krauss, R. Kuhn, and G. Soff, *AMEGIC++ 1.0: A Matrix element generator in C++*, JHEP **02** (2002) 044, arXiv:hep-ph/0109036 [hep-ph].

[40] T. Gleisberg and F. Krauss, *Automating dipole subtraction for QCD NLO calculations*, Eur. Phys. J. **C53** (2008) 501–523, arXiv:0709.2881 [hep-ph].

[41] S. Kallweit, J. M. Lindert, P. Maierhöfer, S. Pozzorini, and M. Schnherr, *NLO QCD+EW predictions for V + jets including off-shell vector-boson decays and multijet merging*, JHEP **04** (2016) 021, arXiv:1511.08692 [hep-ph].

[42] NNPDF Collaboration, *Parton distributions with QED corrections*, Nucl. Phys. **B877** (2013) 290–320, arXiv:1308.0598 [hep-ph].

[43] M. Schöenherr. Private communication, 2016.

[44] R. Boughezal, X. Liu, and F. Petriello, *W-boson plus jet differential distributions at NNLO in QCD*, arXiv:1602.06965 [hep-ph].

[45] R. Boughezal, C. Focke, X. Liu, and F. Petriello, *W-boson production in association with a jet at next-to-next-to-leading order in perturbative QCD*, Phys. Rev. Lett. **115** (2015) 062002, arXiv:1504.02131 [hep-ph].

[46] J. R. Gaunt, M. Stahlhofen, F. J. Tackmann, and J. R. Walsh, *N-jettiness Subtractions for NNLO QCD Calculations*, JHEP **09** (2015) 058, arXiv:1505.04794 [hep-ph].

[47] S. Dulat et al., *New parton distribution functions from a global analysis of quantum chromodynamics*, Phys. Rev. D **93** (2016) 033006, arXiv:1506.07443 [hep-ph].

[48] L. Evans and P. Bryant, *LHC Machine*, JINST **3** (2008) S08001.

[49] C. Service graphique, *Overall view of the LHC. Vue d'ensemble du LHC*, https://cds.cern.ch/record/1708849, General Photo.

[50] ATLAS Collaboration, *Characterization of Interaction-Point Beam Parameters Using the pp Event-Vertex Distribution Reconstructed in the ATLAS Detector at the LHC*, ATLAS-CONF-2010-027, 2010, https://cds.cern.ch/record/1277659.

[51] ATLAS Collaboration, *Luminosity determination in pp collisions at $\sqrt{s}$ = 8 TeV using the ATLAS detector at the LHC*, Eur. Phys. J. **C76** (2016) 653, arXiv:1608.03953 [hep-ex].

[52] ATLAS Collaboration, *LuminosityPublicResults*, https://twiki.cern.ch/twiki/bin/view/AtlasPublic/LuminosityPublicResults.

[53] ATLAS Collaboration, *The ATLAS Experiment at the CERN Large Hadron Collider*, JINST **3** (2008) S08003.

[54] C. AC, *Layout of ATLAS. Dessin representant le detecteur ATLAS*, Mar, 1998, https://cds.cern.ch/record/39038.

[55] J. Pequenao, *Computer generated image of the ATLAS inner detector*, Mar, 2008, http://cds.cern.ch/record/1095926.

[56] ATLAS Collaboration, *Particle Identification Performance of the ATLAS Transition Radiation Tracker*, ATLAS-CONF-2011-128, 2011, https://cds.cern.ch/record/1383793.

[57] ATLAS Collaboration, *Alignment of the ATLAS Inner Detector and its Performance in 2012*, ATLAS-CONF-2014-047, 2014, https://cds.cern.ch/record/1741021.

[58] ATLAS Collaboration, *Reconstruction of primary vertices at the ATLAS experiment in Run 1 proton-proton collisions at the LHC*, arXiv:1611.10235 [physics.ins-det].

[59] J. Pequenao, *Computer Generated image of the ATLAS calorimeter*, Mar, 2008.

[60] Y. A. Kulchitskii, *Hadron Energy Reconstruction for the ATLAS Barrel Prototype Combined Calorimeter in the Framework of the Non-parametrical Method*, Tech. Rep. JINR-E1-2000-73, Joint Inst. Nucl. Res., Dubna, 2000. arXiv:0004009 [hep-ex]. http://cds.cern.ch/record/433762.

[61] M. A. et al., *Energy linearity and resolution of the {ATLAS} electromagnetic barrel calorimeter in an electron test-beam*, Nuclear Instruments and Methods in Physics Research Section A: Accelerators, Spectrometers, Detectors and Associated Equipment **568** (2006) 601 – 623, http://www.sciencedirect.com/science/article/pii/S0168900206013222.

[62] ATLAS Collaboration, A. Airapetian et al., *ATLAS: Detector and physics performance technical design report. Volume 1*, https://cds.cern.ch/record/391176.

[63] ATLAS Collaboration, G. Aad et al., *Expected Performance of the ATLAS Experiment - Detector, Trigger and Physics*, arXiv:0901.0512 [hep-ex].

[64] T. Djobava, A. Henriques-Coreira, M. Mosidze, and G. Mchedlidze, *Study of ATLAS tile calorimeter energy resolution, linearity and sampling fraction at electromagnetic scale*, GESJ Phys. **2009N1** (2009) 41–53, http://gesj.internet-academy.org.ge/download.php?id=1459.pdf.

[65] Particle Data Group, *Atomic and Nuclear Properties of Materials for more than 300 materials*, http://pdg.lbl.gov/2016/AtomicNuclearProperties/.

[66] J. Pequenao, *Computer generated image of the ATLAS Muons subsystem*, Mar, 2008, http://cds.cern.ch/record/1095929.

[67] ATLAS Collaboration, *Performance of the ATLAS muon trigger in pp collisions at* $\sqrt{s} = 8$ *TeV*, Eur. Phys. J. C **75** (2015) 120, arXiv:1408.3179 [hep-ex].

[68] ATLAS Collaboration, *The ATLAS Simulation Infrastructure*, Eur. Phys. J. C **70** (2010) 823, arXiv:1005.4568 [hep-ex].

[69] GEANT4 Collaboration, S. Agostinelli et al., *GEANT4: A simulation toolkit*, Nucl. Instrum. Meth. A **506** (2003) 250.

[70] ATLAS Collaboration, *Summary of ATLAS Pythia 8 tunes*, ATL-PHYS-PUB-2012-003 (2012), http://cds.cern.ch/record/1474107.

[71] P. Z. Skands, *Tuning Monte Carlo generators: The Perugia tunes*, Phys. Rev. D **82** (2010) 074018, arXiv:1005.3457 [hep-ph].

[72] P. Nason, *A New method for combining NLO QCD with shower Monte Carlo algorithms*, JHEP **11** (2004) 040, arXiv:hep-ph/0409146 [hep-ph].

[73] S. Frixione, P. Nason, and C. Oleari, *Matching NLO QCD computations with Parton Shower simulations: the POWHEG method*, JHEP **11** (2007) 070, arXiv:0709.2092 [hep-ph], * Temporary entry *.

[74] S. Alioli, P. Nason, C. Oleari, and E. Re, *A general framework for implementing NLO calculations in shower Monte Carlo programs: the POWHEG BOX*, JHEP **06** (2010) 043, arXiv:1002.2581 [hep-ph].

[75] S. Frixione, P. Nason, and G. Ridolfi, *A Positive-weight next-to-leading-order Monte Carlo for heavy flavour hadroproduction*, JHEP **09** (2007) 126, arXiv:0707.3088 [hep-ph].

[76] M. Czakon and A. Mitov, *Top++: A Program for the Calculation of the Top-Pair Cross-Section at Hadron Colliders*, arXiv:1112.5675 [hep-ph].

[77] M. Botje et al., *The PDF4LHC Working Group Interim Recommendations*, arXiv:1101.0538 [hep-ph].

[78] R. D. Ball et al., *Parton distributions with LHC data*, Nucl. Phys. **B867** (2013) 244–289, arXiv:1207.1303 [hep-ph].

[79] S. Frixione and B. R. Webber, *Matching NLO QCD computations and parton shower simulations*, JHEP **06** (2002) 029, arXiv:hep-ph/0204244.

[80] G. Corcella et al., *HERWIG 6: An Event generator for hadron emission reactions with interfering gluons (including supersymmetric processes)*, JHEP **01** (2001) 010, arXiv:hep-ph/0011363 [hep-ph].

[81] J. Butterworth, J. R. Forshaw, and M. Seymour, *Multiparton interactions in photoproduction at HERA*, Z. Phys. C **72** (1996) 637, arXiv:hep-ph/9601371 [hep-ph].

[82] Particle Data Group Collaboration, *Review of Particle Physics*, Chin. Phys. **C40** (2016) 100001.

[83] J. M. Campbell and R. K. Ellis, *An Update on vector boson pair production at hadron colliders*, Phys. Rev. D **60** (1999) 113006, arXiv:hep-ph/9905386 [hep-ph].

[84] ATLAS Collaboration, *Performance of the ATLAS Inner Detector Track and Vertex Reconstruction in High Pile-Up LHC Environment*, ATLAS-CONF-2012-042, 2012, https://cds.cern.ch/record/1435196.

[85] S. Hassani, L. Chevalier, E. Lancon, J. F. Laporte, R. Nicolaidou, and A. Ouraou, *A muon identification and combined reconstruction procedure for the ATLAS detector at the LHC using the (MUONBOY, STACO, MuTag) reconstruction packages*, Nucl. Instrum. Meth. **A572** (2007) 77–79.

[86] ATLAS Collaboration, *Measurement of the muon reconstruction performance of the ATLAS detector using 2011 and 2012 LHC proton–proton collision data*, Eur. Phys. J. C **74** (2014) 3130, arXiv:1407.3935 [hep-ex].

[87] ATLAS Collaboration, *Topological cell clustering in the ATLAS calorimeters and its performance in LHC Run 1*, arXiv:1603.02934 [hep-ex].

[88] M. Cacciari, G. P. Salam, and G. Soyez, *The anti-k_t jet clustering algorithm*, JHEP **04** (2008) 063, arXiv:0802.1189 [hep-ph].

[89] M. Cacciari and G. P. Salam, *Dispelling the N^3 myth for the k_t jet-finder*, Phys. Lett. B **641** (2006) 57, arXiv:hep-ph/0512210.

[90] M. Cacciari, G. P. Salam, and G. Soyez, *FastJet User Manual*, Eur. Phys. J. C **72** (2012) 1896, arXiv:1111.6097 [hep-ph].

[91] ATLAS Collaboration, *Jet energy measurement and its systematic uncertainty in proton–proton collisions at $\sqrt{s} = 7$ TeV with the ATLAS detector*, Eur. Phys. J. C **75** (2015) 17, arXiv:1406.0076 [hep-ex].

[92] ATLAS Collaboration, *Performance of pile-up mitigation techniques for jets in pp collisions with the ATLAS detector*, arXiv:1510.03823 [hep-ex].

[93] ATLAS Collaboration, *Monte Carlo Calibration and Combination of In-situ Measurements of Jet Energy Scale, Jet Energy Resolution and Jet Mass in ATLAS*, ATLAS-CONF-2015-037, 2015, https://cds.cern.ch/record/2044941.

[94] ATLAS Collaboration, *Electron efficiency measurements with the ATLAS detector using the 2012 LHC proton–proton collision data*, ATLAS-CONF-2014-032, 2014, https://cds.cern.ch/record/1706245.

[95] ATLAS Collaboration, *Electron and photon energy calibration with the ATLAS detector using LHC Run 1 data*, Eur. Phys. J. C **74** (2014) 3071, arXiv:1407.5063 [hep-ex].

[96] ATLAS Collaboration, *Performance of the ATLAS Secondary Vertex b-tagging Algorithm in 7 TeV Collision Data*, ATLAS-CONF-2010-042, 2010, https://cds.cern.ch/record/1277682.

[97] ATLAS Collaboration, *Performance of b-Jet Identification in the ATLAS Experiment*, JINST **11** (2016) P04008, arXiv:1512.01094 [hep-ex].

[98] J. Neyman and E. S. Pearson, *On the Problem of the Most Efficient Tests of Statistical Hypotheses*, Philosophical Transactions of the Royal Society of London. Series A, Containing Papers of a Mathematical or Physical Character **231** (1933) 289–337, http://www.jstor.org/stable/91247.

[99] G. Piacquadio and C. Weiser, *A new inclusive secondary vertex algorithm for b-jet tagging in ATLAS*, J. Phys. Conf. Ser. **119** (2008) 032032.

[100] ATLAS Collaboration, *Calibration of the performance of b-tagging for c and light-flavour jets in the 2012 ATLAS data*, ATLAS-CONF-2014-046, 2014, https://cds.cern.ch/record/1741020.

[101] ATLAS Collaboration, *Calibration of b-tagging using dileptonic top pair events in a combinatorial likelihood approach with the ATLAS experiment*, ATLAS-CONF-2014-004, 2014, https://cds.cern.ch/record/1664335.

[102] ATLAS Collaboration, *Performance of missing transverse momentum reconstruction in proton–proton collisions at $\sqrt{s} = 7$ TeV with ATLAS*, Eur. Phys. J. C **72** (2012) 1844, arXiv:1108.5602 [hep-ex].

[103] ATLAS Collaboration, *Identification of high transverse momentum top quarks in pp collisions at $\sqrt{s} = 8$ TeV with the ATLAS detector*, JHEP **06** (2016) 093, arXiv:1603.03127 [hep-ex].

[104] D. Krohn, J. Thaler, and L.-T. Wang, *Jet Trimming*, JHEP **02** (2010) 084, arXiv:0912.1342 [hep-ph].

[105] ATLAS Collaboration, *Performance of jet substructure techniques for large-R jets in proton–proton collisions at $\sqrt{s} = 7$ TeV using the ATLAS detector*, JHEP **09** (2013) 076, arXiv:1306.4945 [hep-ex].

[106] ATLAS Collaboration, *JetEtmissApproved2014LargeRJES*, https://twiki.cern.ch/twiki/bin/view/AtlasPublic/JetEtmissApproved2014LargeRJES.

[107] ATLAS Collaboration, *JetEtmissApproved2013JESUncertainty*, https://twiki.cern.ch/twiki/bin/view/AtlasPublic/JetEtmissApproved2013JESUncertainty.

[108] ATLAS Collaboration, *Characterisation and mitigation of beam-induced backgrounds observed in the ATLAS detector during the 2011 proton–proton run*, JINST **8** (2013) P07004, arXiv:1303.0223 [hep-ex].

[109] ATLAS Collaboration, J. Kraus, *First observation of electrons in the ATLAS detector*, PoS **HCP2009** (2009) 081, http://cds.cern.ch/record/1233724.

[110] ATLAS Collaboration (internal), *BCHCleaningTool*, https://twiki.cern.ch/twiki/bin/view/AtlasProtected/BCHCleaningTool.

[111] B. Lenzi, C. Guyot, and R. Nicolaidou, *Search for the Higgs boson decaying to four leptons in the ATLAS detector at LHC and studies of muon isolation and energy loss*. PhD thesis, U. Paris-Sud 11, Dept. Phys., Orsay, France, 2010. https://cds.cern.ch/record/1301521.

[112] J. Smith, W. L. van Neerven, and J. A. M. Vermaseren, *Transverse Mass and Width of the W Boson*, Phys. Rev. Lett. **50** (1983) 1738–1740.

[113] *Proposal for truth particle observable definitions in physics measurements*, Tech. Rep. ATL-PHYS-PUB-2015-013, CERN, Geneva, Jun, 2015. https://cds.cern.ch/record/2022743.

[114] G. D'Agostini, *Improved iterative Bayesian unfolding*, arXiv:1010.0632 [physics.data-an].

[115] K. Bierwagen, U. Blumenschein, and A. Quadt, *Bayesian Unfolding*, https://indico.cern.ch/event/107747/contributions/32648/attachments/24323/35007/bierwagen.pdf.

[116] T. Adye, R. Claridge, K. Tackmann and F. Wilson, *RooUnfold: ROOT Unfolding Framework*, http://hepunx.rl.ac.uk/~adye/software/unfold/RooUnfold.html.

[117] ATLAS Collaboration, *JetEtmissApproved2013Jer2011*, https://twiki.cern.ch/twiki/bin/view/AtlasPublic/JetEtmissApproved2013Jer2011.

[118] ATLAS Collaboration, *Performance of Missing Transverse Momentum Reconstruction in ATLAS studied in Proton–Proton Collisions recorded in 2012 at* $\sqrt{s} = 8$ *TeV*, ATLAS-CONF-2013-082, 2013, https://cds.cern.ch/record/1570993.

[119] B. Malaescu, *An Iterative, dynamically stabilized method of data unfolding*, arXiv:0907.3791 [physics.data-an].

[120] ATLAS Collaboration, *Measurement of the W charge asymmetry in the* $W \to \mu\nu$ *decay mode in pp collisions at* $\sqrt{s} = 7$ *TeV with the ATLAS detector*, Phys. Lett. B **701** (2011) 31, arXiv:1103.2929 [hep-ex].

[121] ATLAS Collaboration, *Muon reconstruction efficiency and momentum resolution of the ATLAS experiment in proton–proton collisions at* $\sqrt{s} = 7$ *TeV in 2010*, Eur. Phys. J. C **74** (2014) 3034, arXiv:1404.4562 [hep-ex].

[122] ATLAS Collaboration, *Measurement of the differential cross-section of highly boosted top quarks as a function of their transverse momentum in* $\sqrt{s} = 8$ *TeV proton–proton collisions using the ATLAS detector*, Phys. Rev. D **93** (2016) 032009, arXiv:1510.03818 [hep-ex].

APPENDIX A

FURTHER CHECKS

A.1 Isolation Efficiency Modelling

As part of the signal region event selection of Section 5.4, the muon is required to be isolated. Some of the muons used in this analysis are located inside a jet ($\Delta R < 0.4$), where a large number of tracks and calorimeter deposits are present that can contribute to the isolation energies. While the simulation of muon isolation energies has been studied before [121], muons that were inside jets were not considered, and so it was not known whether isolation was well-described by the simulation.

To validate the simulation, a dedicated study is performed to measure the efficiency of the muon isolation requirement as function of the angular separation ΔR between the muon and the closest jet in simulation and in data. Events containing Lorentz-boosted $t\bar{t}$ are used, because the topology is very similar to collinear W production.

A sample of $t\bar{t}$ events is obtained from data and from a simulated $t\bar{t}$ sample using a selection that does not involve any requirements on muon isolation. The selection requires that each event contains:

- Exactly one muon (object definition of muon is same as in Section 5.2.3 except $p_{\mathrm{T}} > 36$ GeV)
- Passes the non-isolated muon trigger (described in Section 5.2.2)
- Reconstructed muon matches the muon that passed the trigger
- Leptonic top-quark – at least one anti-k_t $R = 0.4$ jet that satisfies the following (if more than one is found, take the highest p_{T} one):
  - $p_{\mathrm{T}} > 25$ GeV

  - $|\eta| < 2.1$
  - $\Delta R(\mu, \text{jet}_{R=0.4}) < 1.5$

- Hadronic top-quark – at least one anti-k_t $R = 1.0$ trimmed jet that satisifes the following (if more than one is found, take the highest p_{T} one):
  - $p_{\text{T}} > 350$ GeV
  - $|\eta| < 2.1$
  - $m > 100$ GeV
  - $\sqrt{d_{12}} > 40$ GeV
  - $\Delta R(\text{jet}_{R=1.0}, \text{jet}_{R=0.4}) > 1.5$
  - $\Delta\phi(\mu, \text{jet}_{R=1.0}) > 2.3$
- $E_{\text{T}}^{\text{miss}} > 20$ GeV
- $E_{\text{T}}^{\text{miss}} + m_{\text{T}}^{W} > 60$ GeV
- Two b-tags (using the working point that corresponds to an efficiency of tagging a b-jet of 70%):
  - The $R = 0.4$ jet found from the 'leptonic top' selection above must be b-tagged
  - At least one anti-k_t $R = 0.4$ jet that satisifes $\Delta R(\text{jet}_{R=1.0}, \text{jet}_{b-\text{tagged},R=0.4}) < 1.0$ must be b-tagged
- $\Delta R(\mu, \text{jet}_{R=0.4}) < 0.04 + \frac{10.0 \text{ GeV}}{p_{\text{T}}^{\mu}}$

It is adapted from Ref. [122], where the main differences are the jet p_{T} requirement being increased by 50 GeV and both the leptonic top and the hadronic top are required to be b-tagged. Figure A.1, which gives the distribution of ΔR in data and in MC simulation after applying the selection, shows that it is successful at providing a relatively pure sample of $t\bar{t}$

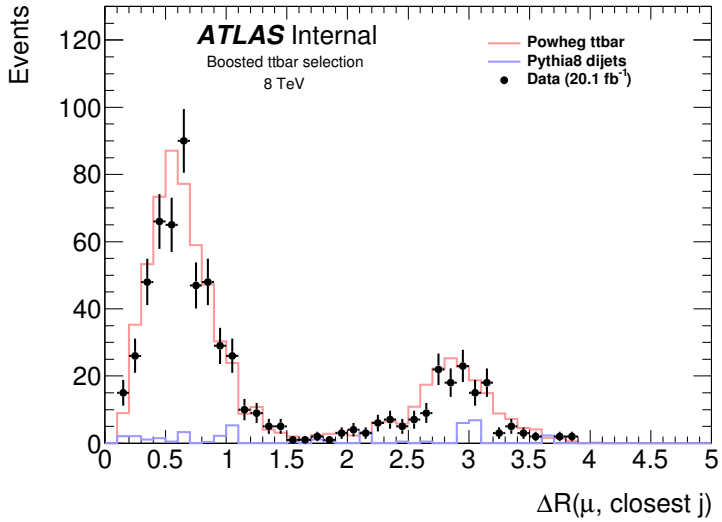

Figure A.1: Distribution of the angular separation between the muon and the closest jet in events from data and from simlated MC samples using the boosted $t\bar{t}$ selection of Appendix A.1.

events from data across the entire ΔR range, as the background from QCD dijets is small. For the sample of events from data, even though the predicted background from QCD dijets is small, the dijet background is still subtracted.

Using these events, the efficiency of the muon isolation requirement is measured by dividing the number of events that would pass the requirement by the total number of events, and this is shown in Figure 5.7 for both data and simulation. As the data and simulation are consistent to within the statistical uncertainties, there is no indication that the modelling and simulation of the muon isolation efficiency are inaccurate. As a result, no scale factors or uncertainties pertaining to the muon isolation efficiency are applied. However, there are an insufficient number of events to draw that conclusion for the region of $\Delta R < 0.2$, and this is why events with $\Delta R < 0.2$ are excluded in the analysis.

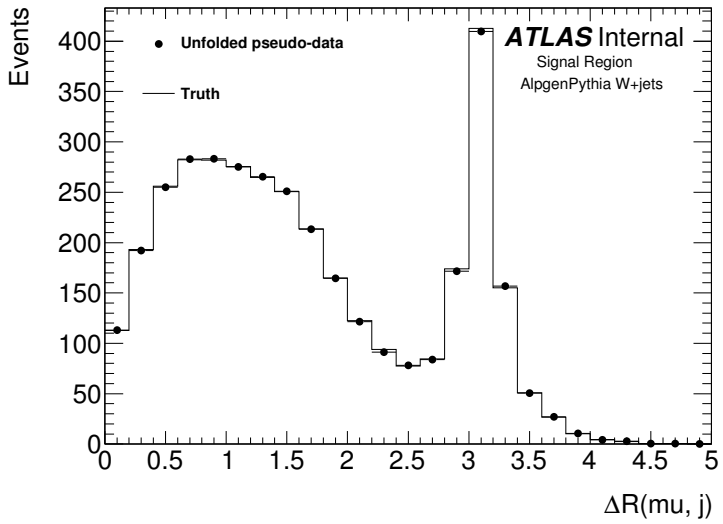

Figure A.2: Distributions of ΔR from unfolded pseudo-data, where the pseudo-data is taken from simulated W + jets events, and from MC truth. The error bars shown here are not the statistical uncertainty in the psuedo-data, but the uncertainty due to the finite number of MC toys used in the unfolding.

A.2 Unfolding Validation

This section describes a few procedures that are performed to validate the unfolding, which is detailed in Section 5.8.

A simple validation of the unfolding is to unfold pseudo-data, taken from simulated W + jets events. Since these simulated W + jets events are from the same MC sample that was used to evaluate the signal selection efficiency and detector response, one would expect that the unfolded distribution should be identical to the particle-level truth distribution. The comparison of the two distributions is shown in Figure A.2, and the expected agreement is observed except for very small statistical fluctuations which arise from the MC toy approach.

A cross-check of the unfolding is performed by unfolding the background-subtracted data using a signal selection efficiency and detector response that have been evaluated using an alternative simulated MC sample. Here, the PYTHIA8 W + jets MC sample of Section 4.2.1 is used instead of the one from ALPGEN+PYTHIA6. The two unfolded distributions of

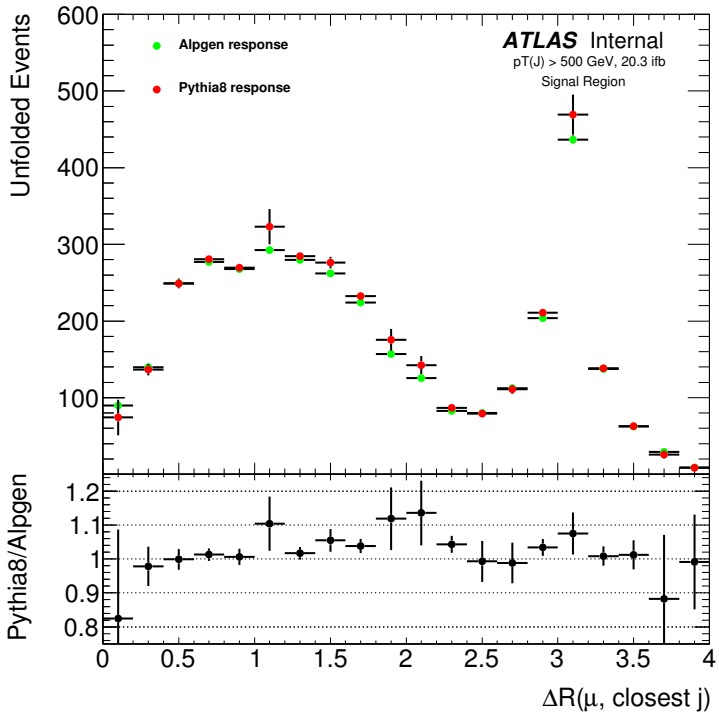

Figure A.3: Distributions of ΔR from unfolded background-subtracted data where the unfolding uses an ALPGEN+PYTHIA6 W + jets MC sample (green) and where it uses a PYTHIA8 W + jets MC sample (red) for evaluating the signal selection efficiency and detector response. The error bars shown are the statistical uncertainties that arise from the limited number of events in the two MC samples.

ΔR from data that result from using these two MC samples in the unfolding are shown in Figure A.3. Both distributions are consistent with each other to within the statistical uncertainties that arise from the limited number of events in the two MC samples.

The MC sample that is used to evaluate the signal selection efficiency and detector response for the unfolding contains both collinear W events and back-to-back W + jets events. As the ratio of the number of collinear events to the number of back-to-back events may not be predicted by the MC generator accurately, this might bias the unfolding if the efficiency and response were not the same for these two categories of events. In order to assess whether there is a bias, background-subtracted data is unfolded twice using the simulated PYTHIA8 W + jets MC sample. In the first instance, events from this sample that contain

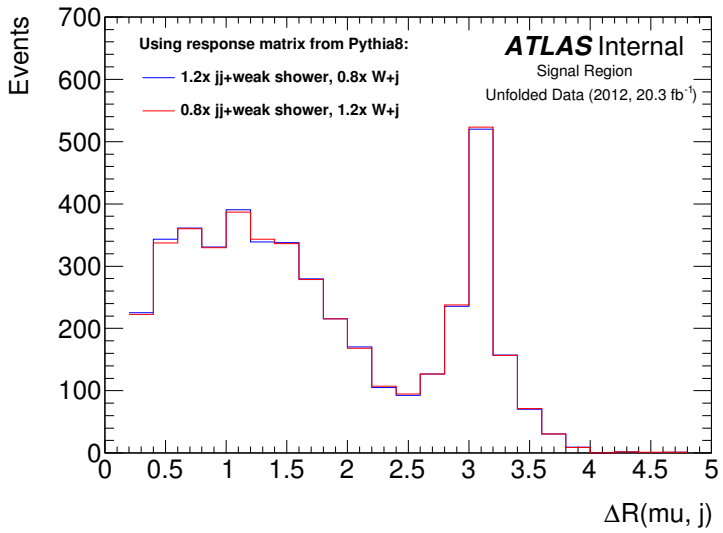

Figure A.4: Distributions of ΔR from unfolded background-subtracted data where a PYTHIA8 W + jets MC sample modified to contain 20% more collinear W events and 20% fewer back-to-back W + jets events (blue) and vice-versa (red) is used for evaluating the signal selection efficiency and detector response.

a collinear W are weighted by a factor of 1.2 and those that contain a back-to-back W are weighted by a factor of 0.8, and vice versa in the second instance. As there is a negligble difference between the two unfolded distributions, shown in Figure A.4, this indicates that the results of the unfolding have no significant dependence on the relative fraction of collinear W events predicted by the MC generator.

A.3 Muon Reconstruction Inside Jets

During muon reconstruction, described in Section 4.3.1, tracks in the Inner Detector are combined with tracks in the Muon Spectrometer. For muons that are inside jets, there could be an increased chance that the wrong Inner Detector track is chosen for this combination, as there are a lot of tracks produced inside an energetic jet, degrading the performance of reconstruction.

To investigate this, the agreement on the muon momentum between the Inner Detector

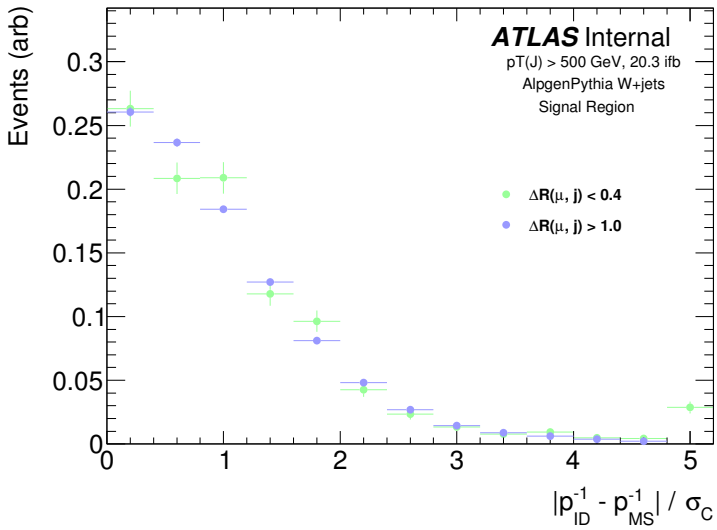

Figure A.5: Distribution of the agreement in muon track curvature p^{-1} between the Inner Detector track (ID) and the Muon Spectrometer track (MS) for muons inside a jet (green) and for muons outside of a jet (blue). σ_C is the combined uncertainty on the two measurements.

track and the Muon Spectrometer track is measured in simulated W + jets events for when the muon is inside a jet ($\Delta R < 0.4$) and for when it is far away from a jet ($\Delta R > 1.0$). If a track mispairing occurs, the momentum measurement from the Inner Detector would be wrong and very different from the measurement from the Muon Spectrometer. Technically, track curvature, the inverse of the muon momentum, is measured and the agreement is defined as the difference between the two curvatures divided by the combined uncertainty σ_C on the two measurements. As the two distributions of the agreement, shown in Figure A.5, are very similar, this indicates that the rate of track mispairing does not increase and muon reconstruction peformance is unaffected when muons are inside a jet.